Structure of Matter:
Nuclear and Hadron Physics

In this section the Scientific Report deals with nuclei, their excitations and their constituents, the hadrons. It thus contains work exploring details of the excitation spectrum of finite, strongly interacting systems as represented by the atomic nucleus and investigations probing strongly interacting matter and its hadronic constituents as produced in collisions between nuclei. Thus various facets of matter in the universe and the processes governing its development in time are investigated.

One milestone in our research was the start of the physics program of the HADES[1] detector system. The HADES experiments at the SIS accelerator focus on studying the in-medium behaviour of hadrons. The most prevalent hadron, the nucleon, is the building block of nuclei, which constitute nearly all the mass of matter surrounding us. The origin of the masses of hadrons has been proposed to be a key to understand the phenomenon "mass": When embedded in strongly interacting matter vector mesons are expected to undergo alterations in their basic properties like lifetimes, decay widths, and especially masses. HADES offers the unique opportunity to explore such in-medium changes. In the fall of 2002 HADES has taken data out of 200 million events of the reaction C(1.95 AGeV)+C. In this measurement all the components of the detector were used: ring imaging Cerenkov counter, multi-wire drift chambers, time-of-flight wall and shower wall. The forthcoming analysis and interpretation of the data allows to acces fundamental properties of particles with far reaching consequences down to the absolute ground state (vacuum), where strongly interacting particles emerge as excitations. This aspect of our research with supplementary experimental and theoretical investigations on strangeness degrees of freedom in dense matter is reported in the first part of the this Report.

A second milestone of the nuclear physics research at Rossendorf in 2002 was the start of operation of the radiation source ELBE. ELBE delivered a primary electron beam which produced Bremsstrahlung photons. These photons are ideally suited to excite selected states of nuclei to study their properties, e.g. in nuclear resonance fluorescence (NRF) experiments. The details of this research and the accompanying theoretical investigations are described in the second part of this report. The very first experiment are devoted to the test of the Bremsstrahlung facility at ELBE. In preparing the NRF experiments on $^{98,100}Mo$ to be performed at ELBE two measurements at the DYNAMITRON in Stuttgart, were carried out in cooperation with other NRF groups. As a rather surprising result the deexcitation from a dipole state to low lying intruder states was observed. Progress was also achieved in developing a novel time-of-flight spectrometer for the detection of fission fragments. This instrument will allow the study and spectroscopy of fission fragments at ELBE delivering information strongly related to the r-process in the "element cooking" in the universe, leading to the production of the heavy elements. As another astrophysically relevant nuclear reaction we plan to observe the energy dependence of the nuclear photo-effect and thus the behaviour of nuclei in a photon bath, as present e.g. in the early universe or high temperature stellar scenarios. Thus mimicing the various cosmic nuclear processes in the laboratory our research contributes to a comprehensive understanding of where, when and how individual isotopes of the chemical elements are formed. In this field we also want to exploit a pulsed source of fast neutrons, driven by primary electrons from ELBE; this set-up which is developed jointly with IfS of FZR and IKTP of TU Dresden.

[1] The **H**igh-**A**cceptance **Di** **E**lectron **S**pectrometer HADES is installed at the heavy-ion synchrotron SIS in GSI/Darmstadt. In 2002 the manufacturing of the six sectors of the multi-wire drift chambers of plane III has been completed in the FZ Rossendorf.

The results decsribed in this Report are obtained in the following collaborations:

ANKE: Univ. Münster, FZ Jülich, Univ. Giessen, Univ. Bonn, Univ. Köln, Univ. Erlangen-Nürnberg, Fachhochschule München, FZ Rossendorf, JINR Dubna (Russia), Univ. Tbilisi (Georgia), Petersburg Nuclear Physics Institute (Russia), ITEP Moscow (Russia), Russian Academy of Science Moscow (Russia), ECN-Nuclear Energy (Netherlands), Jagellonian Univ. Cracow (Poland), Moscow State University (Russia), Univ. College London (England), Soltan Institute for Nuclear Studies (Poland).

FOPI: Univ. Heidelberg, GSI Darmstadt, FZ Rossendorf, IPNE Bucharest (Romania), KFKI Budapest (Hungary), LPC and Univ. Blaise Pascal Clermont (France), ITEP Moscow (Russia), Kurchatov Institute Moscow (Russia), Korea Univ. Seoul (South Korea), IreS Strasbourg (France), Univ. Warsaw (Poland), RBI Zagreb (Croatia).

HADES: Univ. Frankfurt, TU München, Univ. Giessen, GSI Darmstadt, FZ Rossendorf, Institute of Physics Bratislava (Slovakia), LNS Catania (Italy), LPC and Univ. Blaise Pascal Clermont (France), Jagellonian Univ. Cracow (Poland), JINR Dubna (Russia), Univ. degli Studi di Milano (Italy), ITEP Moscow (Russia), INR Moscow (Russia), MEPhI Moscow (Russia), Univ. of Cyprus (Cyprus), Institute de Physique Nucleaire d'Orsay (France), Nuclear Physics Institute Rez (Czechia), Univ. of Santiago de Compostela (Spain), Univ. of Valencia (Spain).

JLab E 91916: JLAB E91-016: Argonne National Laboratory, Argonne (USA), California Institute of Technology, Pasadena (USA), College of William and Mary, Williamsburg (USA), Duke University, Durham (USA), Florida International University, Miami (USA), FZ Rossendorf, Juniata College, Huntingdon (U0SA), Kent State University, Kent (USA), North Carolina A&T State University, Greensboro (USA), Northwestern University, Evanston (USA), Ohio University, Athens (USA), Southern University at New Orleans, New Orleans (USA), The George Washington University, Washington DC (USA), Thomas Jefferson National Accelerator Facility, Newport News (USA), Tohoku University, Sendai (Japan), University of Houston, Houston, (USA), University of Maryland, College Park (USA), University of Minnesota, Minneapolis (USA), University of Virginia, Charlottesville (USA), Yerevan Physics Institute, Yerevan, (Armenia).

KaoS: TU Darmstadt, Univ. Frankfurt, Univ. Marburg, GSI Darmstadt, Jagellonian Univ. Cracow (Poland), FZ Rossendorf.

TOF: Univ. Bochum, FZ Jülich, Univ. Bonn, TU Dresden, Fachhochschule Jülich, Univ. Tübingen, Univ. Erlangen-Nürnberg, FZ Rossendorf, IUCF Bloomington (USA), INFN Torino (Italy), SINS Warsaw (Poland).

NRF: As in previous years the NRF project was substantially benefitting from the successfull cooperation with the spectroscopy groups from the German universities at Stuttgart, Cologne and Darmstadt as well as with the GSI Darmstadt. We acknowledge also the fruitful collaboration with the colleagues from INRE and the University of Sofia. Furthermore, we are grateful to the cooperation with our colleagues at the Universities of Tennessee and of Notre Dame, USA and with the Joint Institute of Nuclear Research at Dubna.

The Dilepton Spectrometer HADES at SIS/GSI Darmstadt in Operation [B,G]

F. Dohrmann, W. Enghardt, E. Grosse, K. Heidel, J. Hutsch, B. Kämpfer, K. Kanaki, R. Kotte, L. Naumann, A. Sadovski, J. Seibert, M. Sobiella and the HADES collaboration

The High Acceptance Di-Electron Spectrometer (HADES) aimes at measuring in-medium modifications of light vector mesons (ρ,ω,ϕ) in nuclear matter. Such modifications of hadron properties are predicted by various models based on fundamental principles like chiral symmetry and QCD.
The HADES setup is nearly complete; it includes the most detector units, read-out, data-acquisition and trigger electronics. The ring imaging Cherenkov counters (RICH), the inner multiwire drift chambers (MDC-I, MDC-II), the time of flight scintillation hodoscopes (TOF, TOFINO) and the pre-shower modules were completely installed. The performance of the drift chambers as well as all other detectors were monitored online.
Up to now four large-area drift chamber modules of MDC-III, produced at FZ Rossendorf, and two MDC-IV modules,prepared at IPN Orsay, for the outer tracking planes were installed. All six modules of MDC-IIIwere produced at the Rossendorf detector workshop. Thus, two sectors of the spectrometer are fully equipped. The angular acceptance of each segment amounts to $\phi = 0° - 60°$ and $\theta = 18° - 85°$.
The HADES collaboration [1] performed three measuring periods in the year 2002 (see Tab. 1).

Reaction	E/A [GeV]	Events	Remarks
C+C	0.6; 0.8	10^9	DAQ commisioning
Mg+C	1.0	10^8	benchmark beamtime
C+C	2.0	10^9	production beamtime

Tab. 1 *HADES beamtime at 2002.*

First physics studies, aimed at measuring electron-positron pairs produced in relativistic collisions of C+C started in 2001 and have been continued extensively in 2002.
In the November/December 2002 beam time a 2 GeV/nucleon carbon beam with an averaged intensity of $1. \times 10^7$ particles per spill hit a carbon target. The spill length amounted to 9.5 s. The target was 3 mm in diameter and had a length of 2×3 mm. A fast twofold hardware selection was implemented with the first level and the second level triggers. These triggers reduced the data by more than one order of magnitude. Using these triggers, most of the detected reaction products were protons and pions. Tab. 2. shows the accumulated statistics for different trigger levels.

HADES proposal

avg beam curr. pps	beam days	duty cycle %	total beam part.	target int. length %	useful target collisions	Trig2 fraction	physics events
5.00E+06	5	50	1.08E+12	1	1.08E+10	0.1	1.08E+09
2.00E+06	5	50	4.32E+11	1	4.32E+09	0.1	4.32E+08
1.00E+06	5	50	2.16E+11	1	2.16E+09	0.1	2.16E+08

Effective beam data

total stored events	Trig2 fraction	Downscaling fraction	Trig2'ed evts	primary collisions	≈ target collision efficiency	useful target collisions
2.13.E+08	0.073	0.094	9.31.E+07	1.28.E+09	0.8	1.02.E+09

useful target collisions	Stored physics events
1.08E+10	1.08E+09
4.32E+09	4.32E+08
2.16E+09	2.16E+08

useful target collisions	Stored physics events
1.02.E+09	7.45.E+07

N. of events accumulated through the beam time	The fraction of accepted lvl1 triggers accepted by lvl2	The fraction of accepted lvl1 triggers stored but with no leptons	lvl2 accepted events	N. of events examined by lvl2	Fraction of events coming from the real target	N. of beam – target interactions
	The fraction of accepted lvl1 triggers stored to disk					

N. of beam – target interactions	Real "clean" events from target filtered by lvl2

Tab. 2 *Amount of data accumulated during the production beamtime under various trigger conditions in Nov./Dec. 2002.*

Future runs, especially for heavier collision systems require therefore a threefold trigger which is able to reduce the event rate up to a factor of 10^{-4} by preselecting lepton pair candidates to about 100 events/sec. The first level trigger selects central events via the multiplicity information from the TOF scintillators. The second level trigger selects events with dilepton pairs within a given invariant mass range. Pattern recognition units detect electron or positron signatures from Cherenkov rings and electromagnetic showers as well as appropriate time of flight candidates in the TOF wall. In the third level trigger, tracking information from the MDC will be used to reduce the number of fake leptons.
During the beam time we stored 2.13×10^8 events at high magnetic field generated by a current of I = 2500 A. A few files were taken without magnetic field for calibration purposes.
A restricted data analysis is available already during the data collection stage and can be used for the monitoring of different parameters to check the detector performance.
As an example of the monitoring process the vertex distribution along the beam axis around the target region is shown in Fig. 1. The reconstruction has been performed only with a drift cell combination. The insert of Fig. 1 shows, that the vertex reconstruction with this cluster finding algorithm is able to identify the two carbon target discs separated by a distance of $\Delta Z = 20$ mm along the beam axis.

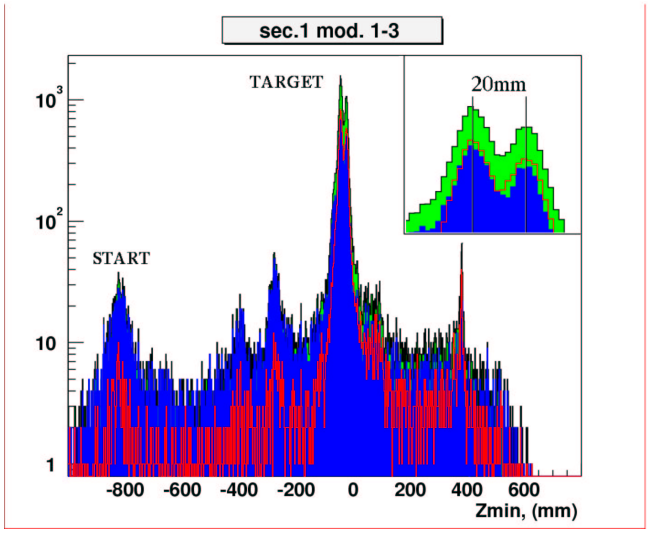

Fig. 1 *Vertex reconstruction with the smallest MDC–I and a large MDC–III in one HADES sector. The cluster finding method requires that the magnet is off to get straight flight pathes. The insert is explained in the text.*

The HADES spectrometer is designed to allow a measurement of the dilepton mass spectrum with an invariant mass resolution of about one percent. Fig. 2 shows the result of the simulated dilepton mass spectrum for the HADES spectrometer. Only conventional sources have been included in the simulation.
The present measurement can determine the e^+e^- yield in the invariant mass region around 500 MeV/c^2. In this region the the DLS collaboration reported [2] a puzzling large yield. The excess of the dileptons in the same invariant mass region, observed by the CERES collaboration [3], can be explained by a strong reshaping of the ρ meson strength. It is therefore important to have sufficiently rich statistics to resolve the ρ and ω peaks to address this issue in more detail.

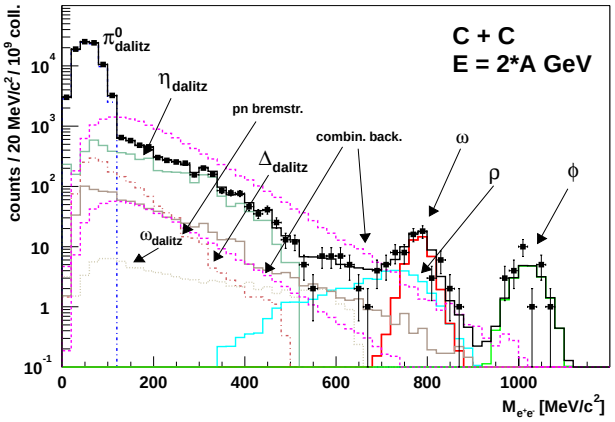

Fig. 2 *Expected frequency of e^+e^- pairs generated in C+C collisions at 2 AGeV versus invariant dilepton mass. The spectra are obtained under realistic assumptions for detector properties. The low (high) combinatorial background is obtained with the best (worst) spatial drift chamber resolution. An amount of 9×10^4 e^+e^- pairs is generated in 2×10^9 target collisions.*

In 2003 one of the main foci of the collaboration is the analysis of the data taken in 2002; this includes the optimization of the analysis software.
Moreover we plan to improve the reliability of the the detector components. For this case one important point is the understanding of the drift chamber aging.
New measurements with proton and pion beams are foreseen for the second half of 2003.

[1] http://www-hades.gsi.de
[2] H. S. Matis et al. (DLS collaboration), Nucl. Phys. A583 (1995) 617c
[3] G. Agakichiev et al. (CERES collaboration), Phys. Rev. Lett. 75 (1995) 1272

Sub-Threshold Phi Meson Production in the Reaction Ni (1.93 A·GeV) + Ni [B,D]

R. Kotte for the FOPI collaboration

Previous exploratory studies of sub-threshold $\phi(1020)$ meson production in central Ni+Ni reactions at 1.93A·GeV have been improved by systematic reanalyses and cross checks. Scanning through $4.7 \cdot 10^6$ central events which comprise about 10% of the total cross section, within the CDC/Barrel acceptance acceptance ($K^{\pm}$ momentum and angular ranges: $p_{t,K} > 100$ MeV/c, $p_{lab,K} < 600$ MeV/c, $40^o < \theta_K < 140^o$) of the FOPI detector setup [1] a number of $23 \pm 7 \pm 2$ correlated K^+K^- meson pairs have been identified (cf. fig. 1). Within this acceptance, the analysis delivers a multiplicity of

$$P_{\phi}^{CDC/Bar} = (1.9 \pm 0.6 \pm 0.95) \cdot 10^{-5}$$

of ϕ mesons per central collision [2]. As a prerequisite, $K^{\pm}$ pair detection efficiencies have been determined performing a complete GEANT simulation.
Assuming an isotropic thermal ϕ source of temperature $T \simeq 90$ MeV, this yield can be extrapolated to a 4π production probability per central collision of

$$P_{\phi} = (2.3 \pm 0.7 \pm 1.1) \cdot 10^{-3}$$

which increases (decreases) by a factor of 2 if the inverse slope parameter T is decreased (increased) to 70 (130) MeV. Comparing the total ϕ yield with the total K^- production probabilities as deduced from FOPI [3] and KaoS [4, 5] experiments (rescaled according to beam energy and centrality differences), we find a surprisingly large ϕ/K^- ratio of at least 0.4. This observation gives rise to the conjecture that presently the K^- production is underestimated due to extrapolations based on rather restricted experimental acceptances. Especially at low c.m. kinetic energies the spectra [4] exhibit hints to an antikaon enhancement on top of the usually observed exponentially declining distribution. Note that such a surplus of low-energy yield may be caused by the decay of intermediate ϕ mesons. (The decay of thermal ϕ mesons with typical inverse slopes of 70-130 MeV would result in daughter $K^{\pm}$ mesons with inverse slopes of only 50% - 60% of that value.) Therefore, future experiments devoted to strangeness production in heavy-ion collisions at sub-threshold energies should aim at sufficient acceptance at low transverse momenta around midrapidity.
The measured yields of correlated K^+K^- pairs as well as the total ϕ production probability have been compared with the output of different transport approaches. The IQMD transport code underestimates the yields in the CDC/Barrel acceptance region by more than an order of magnitude [6]. However, a remarkable step is reached with the most recent BUU approach which includes channels involving intermediate ρ mesons [7]. Within the experimental uncertainties, this code is the first one being able to reproduce the ϕ yield within the FOPI acceptance.
If - in further experiments with statistical more significant results - the unexpectedly high ϕ production [2] will be reconfirmed, then the channel $\phi \rightarrow K^+K^-$ would play a comparably important role for K^- meson production in heavy-ion reactions at subthreshold energies as in near-threshold proton-proton collisions where about 50 % of the antikaons stem from intermediate ϕ mesons [8].

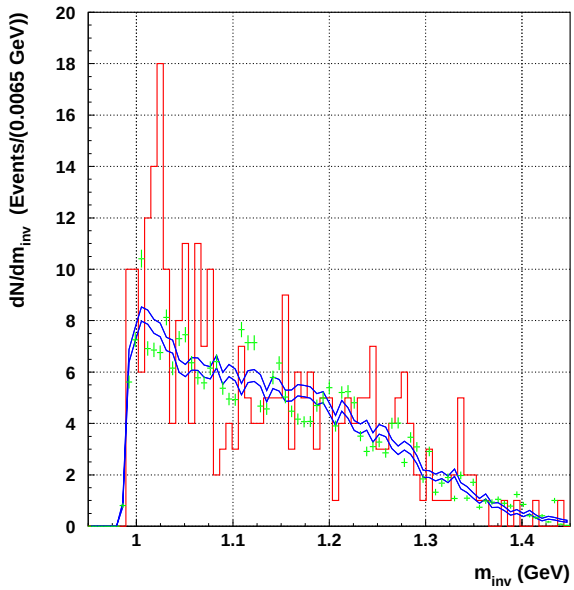

Fig. 1 *The invariant mass distribution of K^+K^- pairs ideintified within the CDC/Barrel acceptance (histogram). The two smooth lines and the error bars show the uncorrelated background obtained via event mixing techniques under different conditions [2].*

[1] A. Gobbi et al. (FOPI collaboration), Nucl. Instr. Meth. A 325 (1993) 156;
J. Ritman for the FOPI collaboration, Nucl. Phys. (Proc. Suppl.) B 44 (1995) 708
[2] A. Mangiarotti and the FOPI collaboration, Nucl. Phys. A 714 (2003) 89
[3] K. Wiśniewski et al. (FOPI collaboration), Eur. Phys. J. A 9 (2000) 515
[4] R. Barth et al. (KaoS collaboration), Phys. Rev. Lett. 78 (1997) 4007
[5] M. Menzel et al. (KaoS collaboration), Phys. Lett. B 495 (2000) 26
[6] C. Hartnack and J. Aichelin, private communication
[7] H. W. Barz, M. Zétényi, G. Wolf, B. Kämpfer, Nucl. Phys. A 705 (2002) 223
[8] F. Balestra et al. (DISTO collaboration), Phys. Lett. B 468 (1999) 7

Inclusive K-meson and Pion Production in Proton-Nucleus Collisions at SIS Energies[B, G]

W. Scheinast and L. Naumann for the KaoS Collaboration:
I. Böttcher[3], M. Dębowski, F. Dohrmann, A. Förster[2], E. Grosse, B. Kamys[5], P. Koczoń[1], B. Kohlmeyer[3], F. Laue[1], M. Menzel[3], L. Naumann, H. Oeschler[2], F. Pühlhofer[3], W. Scheinast, Ch. Schneider, E. Schwab[1], P. Senger[1], Y. Shin[4], H. Ströbele[4], Ch. Sturm[2], G. Surówka[5], F. Uhlig[2], A. Wagner, W. Waluś[5] and H.W. Barz

In 1998 the KaoS collaboration carried out an experiment to investigate the production of kaons and antikaons in proton-nucleus collisions. The Kaon Spectrometer KaoS [1] at the heavy-ion synchrotron SIS at GSI Darmstadt was used to observe charged mesons emitted from a C or Au target struck by the first proton beam at GSI. The kinetic beam energies $T_{\rm kin}$ (1.6, 2.5, and 3.5 GeV) were close to the production threshold of K^+ (1.58 GeV) and K^- (2.5 GeV) in nucleon-nucleon collisions. The whole set of K^+ and K^- spectra, covering four observation angles (32°, 40°, 48°, 56°), was presented in [2].

In addition to these measurements there were also collected data on π^+ and π^- production for a subset of the aforementioned parameters. Their recent analysis opened a new aspect of the interpretation of the $p + A$ reaction dynamics.

To estimate the total cross sections we adjusted to both K- and π-mesons a Maxwell-Boltzmann distribution. For each inclusive reaction (*one* particle species, target nucleus, bombarding energy) all available spectra, i. e. the entire angular distribution, were described by a single function

$$\frac{d^3\sigma}{dp^3} = A \cdot \exp\left(-\frac{E'}{E_0}\right) ,$$

where E' is the total energy of the particle in the frame of maximun isotropic emission moving with velocity $\beta_{\rm em}$. Because there is no a priori reason to choose a particular emission frame, $\beta_{\rm em}$ varied freely together with A and E_0. So, we obtained for each reaction three parameters $(A, E_0, \beta_{\rm em})$, two of which are presented in Fig. 1 (c, d). Fig. 1a shows the total cross section $\sigma_{\rm tot}$ obtained from integrating the Maxwell-Boltzmann distribution.

The energy dependence of $\sigma_{\rm tot}$ and E_0 is much smaller for $\pi^\pm$ than for $K^\pm$ because the pions are produced far above their threshold energy of about $T_{\rm kin} = 0.29$ GeV. In Fig. 1b the cross section is normalized to the geometrical one, yielding the multiplicity

$$M = \frac{\sigma_{\rm tot}}{\sigma_{geo}} \quad \text{with} \quad \sigma_{geo} = \pi \left(1.9\,\text{fm} + \text{A}^{1/3} \cdot 1.2\,\text{fm}\right)^2 .$$

If the target nucleus was an opaque object for the impinging proton, the multiplicity would be equal for

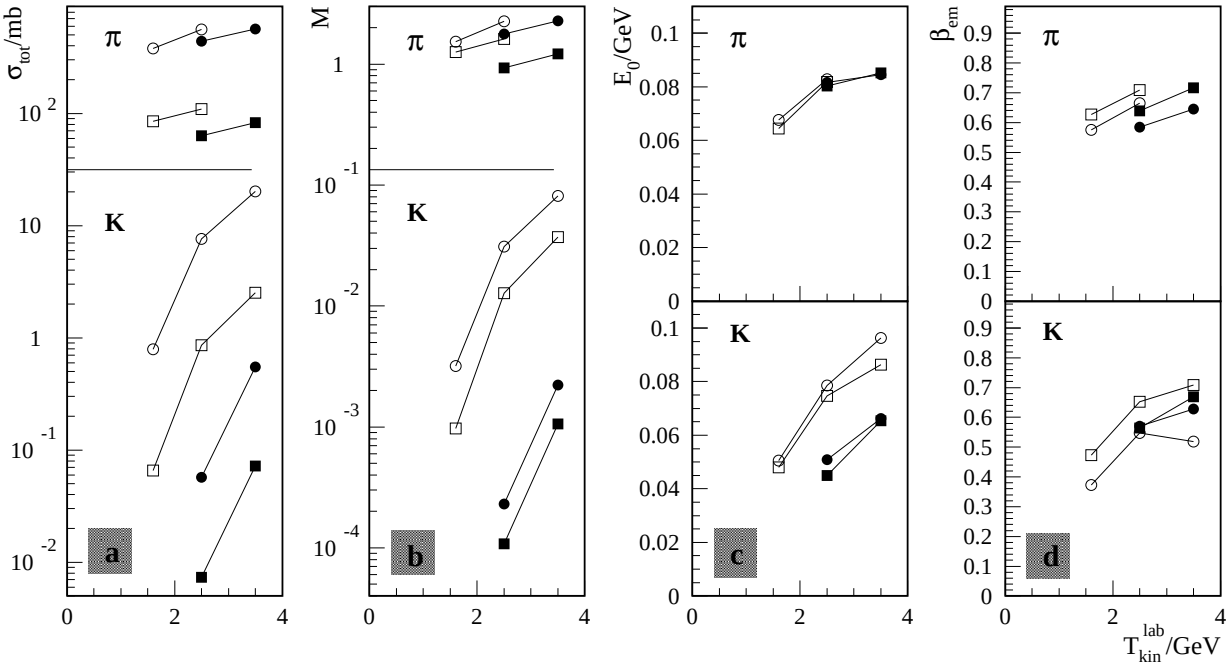

Fig. 1 *Total cross sections (a), multiplicities (b) and fit parameters (c,d) resulting from the adjustment of a Maxwell-Boltzmann distribution to the measured spectra. Open symbols denote* K^+, π^+, *closed symbols* K^-, π^-. *The circles refer to the reaction* $p + Au$, *squares to* $p + C$. T_{kin} *is the kinetic projectile energy.*

[1]GSI Darmstadt, [2]TU Darmstadt, [3]Univ. Marburg, [4]Univ. Frankfurt, [5]Univ. Cracow

both targets. Since this is not the case, the depth, i. e. the volume, plays a role in all these reactions. The production channels are very different for K^+ and K^- because of strangeness conservation; e. g. the threshold reaction in proton-proton collisions is given by $pp \to pK^+\Lambda$ and $pp \to ppK^+K^-$. This leads to very different threshold energies and explains the bigger difference for the quantities σ_{tot} and E_0 between K^+ and K^- than between π^+ and π^-.

As can be observed in Fig. 1c, the slope parameter E_0 is mostly larger for $\pi^\pm$ than for $K^\pm$. This is also caused by different production channels and, furthermore, by different particle masses. So, there remains more energy for the motion of pions.

Finally, the source velocities β_{em} are related to the number of reacting nucleons in the production process. Since particles near threshold can scarcely be produced in primary proton-nucleon collisions, one expects a higher number of participating nucleons for K^- and K^+ rather than for pions. This results in a lower source velocity, as can be seen in Fig. 1d. For a similar reason we see a lower β_{em} in the heavier nucleus Au compared to C.

In the following the pion data obtained at KaoS have been compared with all available data below 10 GeV, for which the value of the total cross section had been mentioned explicitly for inclusive pion production in proton-nucleus collisions. The cross sections in p + C are displayed as a function of the proton bombarding energy for π^+ in Fig. 2 and for π^- in Fig. 3. The only data point for π^+ at 1.6 GeV from [5] fits well to the KaoS data as shown in Fig. 2. We present the first data for 2.5 and 3.5 GeV. All data are in agreement with the BUU calculation in the range from 0.5 GeV up to 3.5 GeV. No total cross section data are available for the pion production in p + Au collisions.

Tab. 1 shows a comparision of the KaoS data and transport calculations with the BUU code [7]. For the carbon target our experimental yields are in good agreement with the theoretical ones. For Au, a heavy target, the theoretical yields overestimate the experimental yields at 2.5 GeV and 3.5 GeV for both the positive and the negative pions. The overestimate amounts to more than 50 percent for the π^- cross sections at 2.5 GeV and 3.5 GeV.

	1.6 GeV	2.5 GeV		3.5 GeV	
	π^+	π^+	π^-	π^-	Target
KaoS	85	109	63	82	C
BUU	89	117	66	78	
KaoS	381	558	439	566	Au
BUU	356	650	659	946	

Tab. 1 *Comparison between experiment and theory for π^+ and π^- cross sections. 'KaoS' denotes the preliminary data presented here, whose systematic errors were valued at 20 %, 'BUU' the transport calculation according to [7].*

So, varying many parameters our data allow for a comprehensive analysis of the kinematics and dynamics in proton-nucleus collisions. All the relations seen can be studied in more detail using complementary data from COSY/ANKE or ITEP/FHS. A combined investigation will be the next step of the ongoing work, supported by various transport calculations.

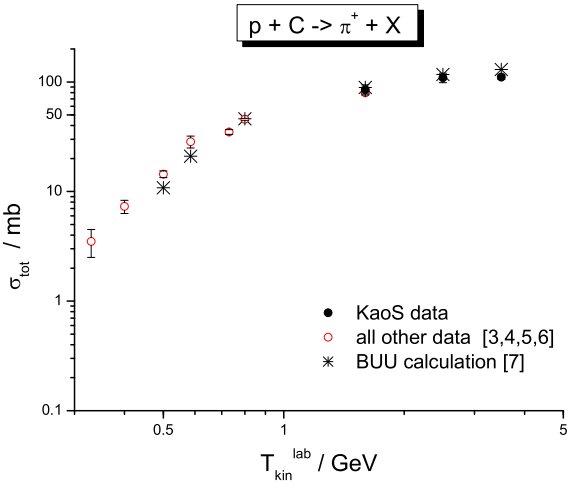

Fig. 2 *Total π^+ cross sections versus proton bombarding energy. The open circles refer to the worldwide available data [3, 4, 5, 6], the full circles to the new yields from the KaoS experiment. The asterisks refer to BUU calculations [7].*

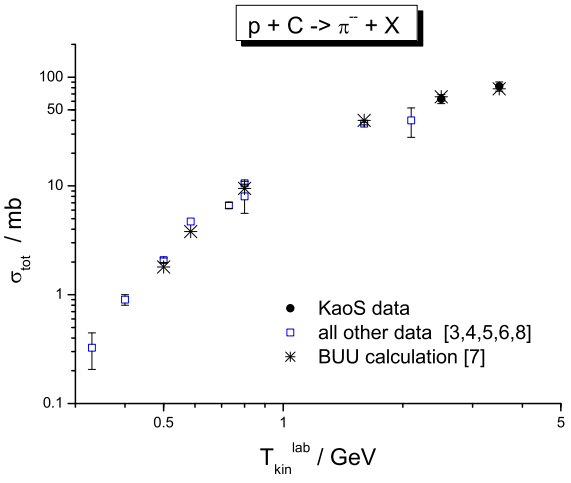

Fig. 3 *Total π^- cross sections versus proton bombarding energy. The open circles refer to the worldwide available data [3, 4, 5, 6, 8], the full squares to the new yields from the KaoS experiment. The asterisks refer to BUU calculations [7].*

[1] P. Senger et al., Nucl. Instr. Meth. A 327 (1993) 39
[2] W. Scheinast et al., Acta Physica Polonica B, Meson 2002 Workshop Proc. (2003) 493
[3] J. F. Crawford et al., Phys. Rev. C 22 (1980) 1184
[4] D. R. F. Cochran et al., Phys. Rev. D 6 (1972) 3085
[5] M. Trzaska et al., Z. Phys. A 340 (1991) 325
[6] N. J. DiGiacomo et al., Phys. Rev. C 31 (1985) 292
[7] Gy. Wolf et al., Nucl. Phys. A 552 (1993) 549
[8] S. Nagamiya et al., Phys. Rev. C 24 (1981) 971

Hyperon-Nucleon Bound States and the Electroproduction of Strangeness on $^{3,4}He$

F. Dohrmann for the Jefferson Lab E91016 Collaboration

The high intensity CW electron beams at the Jefferson Lab provide the possibility to study with high precision the electroproduction of strangeness. Experiment E91016 measured $A(e,e'K^+)YX$ for ^1H, ^2H, ^3He, ^4He, C and Al targets. Here we focus on the results for $^{3,4}He$. Angular distributions of K^+ were measured at forward angles with respect to the virtual photon, γ^*. The experiment was performed in Hall C of Jefferson Lab. For a discussion of the experimental method see [1]. The spectrometer angle for detecting the e' was kept fixed; the K^+ arm was varied. Three different angles between γ^* and K^+ were studied, $\theta^{lab}_{\gamma^*K} = 0^o$, $\simeq 6^o$, and $\simeq 12^o$.
In a previous experiment the reaction $^1H(e,e'K^+)Y$ was studied [1] using the same setup. The missing mass distribution for $^1H(e,e'K^+)Y$ exhibits two peaks corresponding to the Λ and Σ^0 hyperons. The acceptance as well as radiative processes are computed by Monte Carlo simulations. A parametrization of the γ^*N cross section was derived by fitting the kinematic dependences of the $^1H(e,e'K^+)Y$ cross section over the acceptance [1]. This parametrization has been used for $A = 3,4$ [2], where the momentum and in-medium energy of the struck nucleon in the target are taken from spectral functions[3]. Excess yields close to the Λn and ΣN thresholds described in an effective range model[4]. For $A = 3,4$ the agreement between simulation and data is shown in Fig. 1. Near the quasifree Λ-thresholds for $A = 3,4$, Fig. 1 exhibits narrow structures, independent of the angle. These are attributed to the ${}^3_\Lambda H$ and ${}^4_\Lambda H$ bound states and are centered at the right binding energy. While barely discernible for ^3He at $\theta^{lab}_{\gamma^*,K} = 0^o$, it becomes evident for $\theta^{lab}_{\gamma^*,K} = 6^o, 12^o$. It is clearly visible for all measured angles for ^4He. Further quantitative statements are expected after completing the analysis of the data. A kinematic model derived from $^1H(e,e'K^+)Y$ is used in impulse approximation to describe the quasifree production of hyperons on $^{3,4}He$. A spectral function is used to describe the struck nucleon in the target. We observe clear evidence for the ${}^3_\Lambda H$, ${}^4_\Lambda H$ bound states produced in electroproduction.

Acknowledgement: This work has been supported in part by a Feodor Lynen-Fellowship of the Alexander v. Humboldt-Foundation.

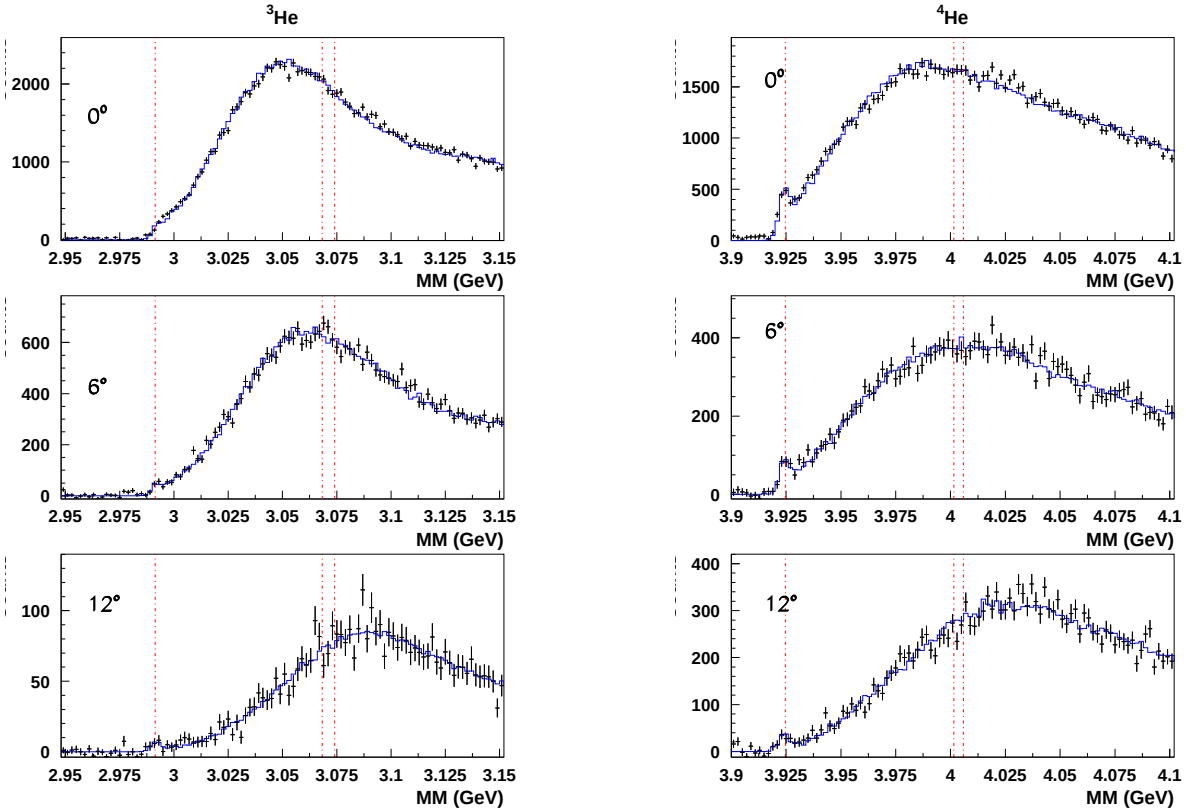

Fig. 1 *Missing mass distributions for $^{3,4}He(e,e'K^+)$ at $\theta^{lab}_{\gamma^*,K} = 0^o, 6^o, 12^o$. Simulations (solid line) of the quasifree production of Λ, Σ^0, Σ^- on $^{3,4}He$, incl. FSI corrections and $^{3,4}He(e,e'K^+)^{3,4}_\Lambda H$ are added. The thresholds for quasifree Λ, Σ^0, Σ^- production for $A = 3,4$ are shown (dot-dashed line).*

[1] B. Zeidman et al., Nucl. Phys. A 691 (2001) 37c
[2] A. Uzzle , PhD thesis, Hampton University (2002)
[3] O. Benhar et al., Nucl. Phys. A 579 (1994) 493
[4] D. Gaskell et al., Phys. Rev. Lett. 87 (2001) 202301

In-Medium Spectral Change of ω Mesons as a Probe of Four-Quark Condensate [B]

S. Zschocke, O.P. Pavlenko[1], B. Kämpfer

Our QCD sum rule evaluations [1] showed that the in-medium change of the four-quark condensate plays a crucial rule for modifications of the ω spectral function. In particular, the sign of the ω meson mass shift is changed by variation of a parameter which describes the strength of the density dependence of the four-quark condensate. In addition, the difference of the vector and axial vector correlators is proportional to the four-quark condensate. Therefore, the sign of the ω meson mass shift, to be measured via the e^+e^- channel at HADES, can serve as a tool for determining of how fast chiral symmetry restoration is approached with increasing density.

We use a correlator satisfying a twice subtracted dispersion relation to get the truncated Borel QCD sum rule

$$\frac{\int_0^{s_0} ds\; S(s,n)\; \mathrm{e}^{-s/M^2}}{\int_0^{s_0} ds\; S(s,n) s^{-1}\; \mathrm{e}^{-s/M^2}} = \tag{1}$$

$$\frac{c_0 M^2[1-\left(1+s_0/M^2\right)\mathrm{e}^{-s_0/M^2}] - c_2/M^2 - c_3/M^4}{c_0\left(1-\mathrm{e}^{-s_0/M^2}\right) + c_1/M^2 + c_2/M^4 + \frac{1}{2}c_3/M^6 - \frac{9n}{4M_N}/M^2}$$

where the imaging any part of in-medium vector meson propagator in the vicinity of the pole mass is

$$S(s,n) = -\frac{\mathrm{Im}\Sigma(s,n)}{(s-m_\omega^2(n))^2 + (\mathrm{Im}\Sigma(s,n))^2} \tag{2}$$

with $\mathrm{Im}\Sigma(s,n)$ as imaginary part of the in-medium ω meson self-energy and $m_\omega(n)$ as its physical mass. Within the linear density approximation, the ω meson self-energy is given by $\Sigma(E,n) = \Sigma^{\mathrm{vac}}(E) - n\; T^{\omega N}(E)$ with $E = \sqrt{s}$ as the ω meson energy, $\Sigma^{\mathrm{vac}}(E) = \Sigma(E, n=0)$ and $T^{\omega N}(E)$ as the off-shell forward ω-nucleon scattering amplitude in free space. c_i are the Wilson coefficients including the condensates. The coefficient c_3 contains also the four-quark condensates $\langle(\overline{q}\gamma_\mu\lambda^a q)^2\rangle_n$ and $\langle(\overline{q}\gamma_\mu\gamma^5\lambda^a q)^2\rangle_n$. The standard approach to estimate their density dependence consists in the mean-field approximation. Within such an approximation the four-quark condensates are proportional to $\langle\overline{q}q\rangle_n^2$, i.e. their density dependence is governed by the square of the chiral quark condensate. We go beyond the mean-field approximation and employ

$$\langle(\overline{q}\gamma_\mu\gamma^5\lambda^a q)^2\rangle_n = -\langle(\overline{q}\gamma_\mu\lambda^a q)^2\rangle_n = \frac{16}{9}\langle\overline{q}q\rangle_0^2\;\kappa_0\;\left[1+\frac{\kappa_N}{\kappa_0}\frac{\sigma_N}{m_q\langle\overline{q}q\rangle_0}\;n\right]. \tag{3}$$

In vacuum, $n=0$, the parameter κ_0 reflects a deviation from the vacuum saturation. To control the deviation of the in-medium four-quark condensate from the mean-field approximation we introduce the parameter κ_N. The limit $\kappa_N = \kappa_0$ recovers the mean-field approximation, while the case $\kappa_N > \kappa_0$ ($\kappa_N < \kappa_0$) is related to a stronger (weaker) density dependence.

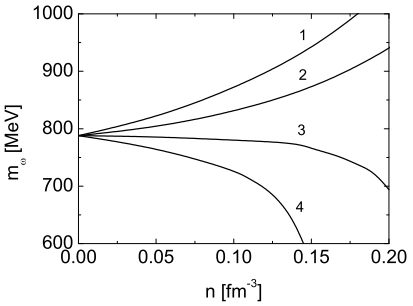

Fig. 1 *Density dependence of the ω meson mass for various values of the parameter κ_N.*

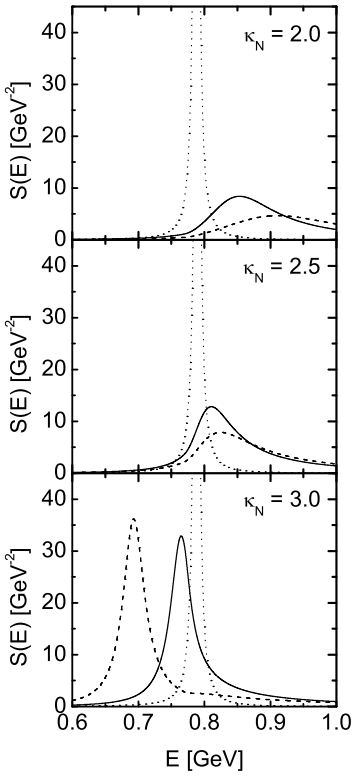

Fig. 2 *The spectral function of the ω meson for $\kappa_N = 2$, 2.5, 3. Solid curves correspond to normal nuclear density ($n = n_0 = 0.15\mathrm{fm}^{-3}$), while dotted and dashed curves are for vacuum and $n = 0.2\mathrm{fm}^{-3}$, respectively.*

We vary the parameter κ_N to estimate the contribution of the four-quark condensates with respect to the main trends of the in-medium modification of the ω meson spectral function. Numerical results of the QCD sum rule evaluation are displayed in figs. 1 and 2. For further details see [2].

[1] S. Zschocke, O.P. Pavlenko, B. Kämpfer, nucl-th/0202134, Eur. Phys. J. A15 (2002) 529
[2] S. Zschocke, O.P. Pavlenko, B. Kämpfer, hep-ph/0212201

[1] *Institute of Theoretical Physics, Kiev, Ukraine*

Modifications of the Di-Electron Spectra from ϕ Meson Decays [B]

B. Kämpfer, O.P. Pavlenko[1], S. Zschocke

The experiments with HADES provide the opportunity to measure via the di-electron channel in-medium modifications of the light vector mesons. There are at least two reasons for studying the in-medium modifications of the ϕ meson. First, within QCD sum rule approaches, the ϕ mass shift in nuclear matter is directly related to the in-medium change of the strange quark condensate $\langle\bar{s}s\rangle$ and, therefore, provides a direct access to the chiral symmetry restoration. This is in contrast to the ρ and ω mesons whose in-medium mass shifts are sensitive to the poorly known four-quark condensate. The second reason to focus on the ϕ meson in-medium effects is related to the interest in understanding the hidden strangeness content of the nucleon and nuclear matter.

Within the linear density approximation the strange quark condensate in hadronic matter can be written as

$$\langle\bar{s}s\rangle_{\rm matter} = \langle\bar{s}s\rangle_0 + \sum_h \frac{\langle h|\bar{s}s|h\rangle}{2M_h}\, n_h, \qquad (1)$$

where $\langle\bar{s}s\rangle_0$ is the vacuum condensate, $\langle h|\bar{s}s|h\rangle$ denotes the matrix element corresponding a one-hadron state, n_h stands for the hadron density, and the sum runs over all hadrons in the medium. For the nucleon matrix element the dimensionless parameter y is widely used to specify the strangeness content in the nucleon via $\frac{\langle N|\bar{s}s|N\rangle}{2M_N} = y\frac{\sigma_N}{2m_q}$, where σ_N is the nucleon sigma term and m_q the light quark mass. The strangeness content of the nucleon is a yet poorly known quantity and matter of debate so far; therefore we shall vary y. We also simplify eq. (1) by the replacement $\sum_h \to y\frac{\sigma_N}{2m_q} n_N$ since the presence of other hadron states can only increase y. Basing on the above parameterization of the strange quark condensate in hadron matter one can perform the QCD sum rule evaluations which give the density dependence in leading order $m_\phi = m_\phi^{\rm vac}(1-0.14y)\frac{n_N}{n_0}$.

The di-electron rate from the in-medium ϕ meson decays in ideal gas approximation at temperature T is

$$\frac{dN}{d^4x\, d^4Q} = \frac{2\,{\rm e}^{-u\cdot Q/T}}{(2\pi)^3} M\Gamma_{\phi\to e^+e^-} A(M^2, m_\phi, \Gamma^{\rm tot}), \quad (2)$$

where $\Gamma_{\phi\to e^+e^-}$ and $\Gamma^{\rm tot}$ are the di-electron and total decay widths, Q_μ denotes the four-momentum of the pair with invariant mass $M^2 = Q^2$, and u_μ is the four-velocity of the medium. We use the Breit-Wigner parameterization of the spectral function A.

To obtain the di-electron spectrum one needs to specify the space-time evolution of the matter. We employ here a variant of the blast wave model [1] with two scenarios for the ϕ multiplicity: (i) the number of ϕ mesons is assumed to be governed by chemical equilibrium, and (ii) the ϕ mesons are still in thermal equilibrium with the bulk of matter but do not maintain chemical equilibrium; to be specific, we take the number as constant. After freeze-out, the ϕ meson decays in vacuum contribute to the spectrum according to [1,2].

The numerical simulations show that, due to the expansion of nuclear matter after the maximum compression stage in the course of heavy-ion collisions, the di-electron spectrum in the ϕ meson region is governed by the superposition of peak positions within a certain interval determined by the nucleon density (see figs. 1 and 2). This causes an effective broadening of the ϕ peak when measured by e^+e^- pairs. The width of the broadening (see fig. 3) appears almost insensitive to the collision broadening in a nuclear medium but is directly related to the density dependence of the strange quark condensate $\langle\bar{s}s\rangle$. This gives a good opportunity to probe the in-medium modification of $\langle\bar{s}s\rangle$ with HADES in heavy-ion collisions.

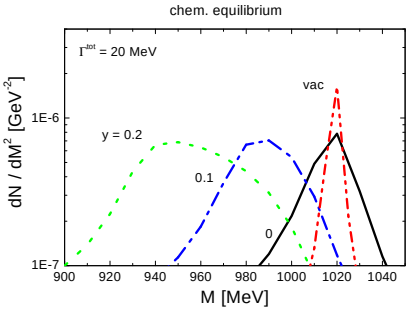

Fig. 1 *Di-electron spectra from ϕ meson decays as a function of invariant mass for case (i), i.e., assumed chemical equilibrium.*

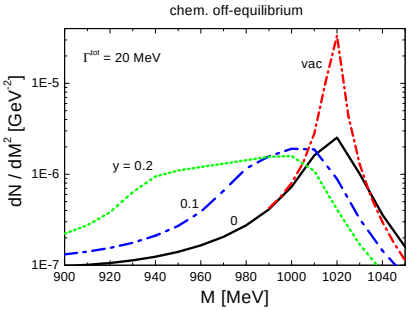

Fig. 2 *As in fig. 1 but for case (ii), i.e., chemical off-equilibrium of ϕ mesons.*

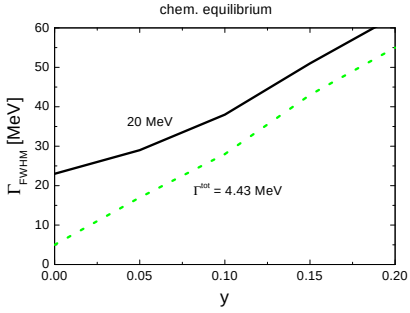

Fig. 3 *The full width half maximum of the ϕ peak as a function of the strangeness content y of nuclear matter.*

[1] B. Kämpfer, O.P. Pavlenko, Eur. Phys. J. A 10 (2001) 101
[2] B. Kämpfer, O.P. Pavlenko, S. Zschocke, nucl-th/0211067, Eur. Phys. J. A (2003) in print

[1] *Institute of Theoretical Physics, Kiev, Ukraine*

Tagging the $pn \to d\phi$ Reaction by Backward Protons in $pd \to d\phi p_{sp}$ Processes [B]

L.P. Kaptari[1], B. Kämpfer, S.S. Semikh[2]

The spectator technique [1] offers one possibility to isolate to a large extent the quasi-free meson (M) production reaction at a neutron when a proton beam impinges on a deuteron target. Since the final state interactions in the pn system differ for singlet and triplet states and can be large at threshold, it is of great advantage to consider the particular reaction $pn \to dM$, as the deuteron (d) is in one well defined state.

In this note we continue our previous study [2] and analyze the complete reaction $pd \to dMp_{sp}$ to test to which extent the spectator technique really selects a quasi-free reaction at the neutron in the deuteron target. In other words, we are going to derive a factorization theorem showing kinematical conditions for which the total cross section $\sigma(pd \to dMp_{sp})$ factorizes in a part depending on the target deuteron characteristics and a part $\sigma(pn \to dM)$. In doing so we select as a sufficiently transparent example the ϕ production. The reasons are obvious: (i) the elementary ϕ production amplitude is simple, (ii) the ϕ meson is interesting with respect to OZI rule [3] and hidden strangeness in the nucleon, and (iii) the ϕ meson is important with respect to both the inclusive K^- [4] production and the e^+e^- decay channel to be studied at HADES in near future.

With the technique described in [2,5] we calculate the process $p_p + p_d = p'_d + p_\phi + p'_p$ at kinetic energies of the incoming proton corresponding to those achievable at the Cooler Synchrotron COSY $T_p \leq 2.7$ GeV. The deuteron is here supposed to be detected in the forward direction, i.e., in direction of the incoming proton with relativistic energy, $T'_d \sim 1$ GeV, and, contrarily, the final (spectator) proton is slowly moving in the backward direction ($\theta_{sp} > 90^0$, $p'_p < 100$ MeV). The main contribution to the process comes then from the spectator mechanism, where the incoming proton interacts with the internal neutron of the deuteron and produces a meson and a deuteron in the final state. The second proton in the deuteron acts merely as a spectator. The spectator mechanism is depicted in fig. 1.

In fig. 2, the differential cross section is presented as a function of the deuteron momentum for the specific choice of variables $\theta'_d = 0^0$, and $\theta'_p = 130^o$. The kinetic energy of the initial proton is $T_p = 2.69$ GeV. Fig. 2 highlights that different models for the deuteron wave function result in vastly different cross sections. This is because the integration over the internal momentum in the final deuteron covers the region of the minimum of the S wave where different models provide essentially different wave functions.

Guided by the very proximity of the numerical results for cross section and polarization observables based on the exact formulae and on the factorized ones [5], we find that, for special kinematical conditions, selection rules are operative immediately causing the above anticipated factorization. This is equivalent to an omission of the contribution of the deuteron D wave at small values of the spectator momentum. This provides a theoretical basis for studying threshold-near processes at quasi-free neutrons.

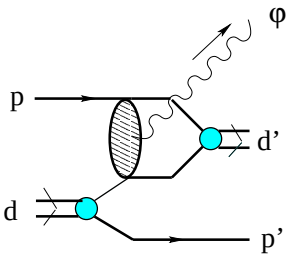

Fig. 1 *Diagram of the considered process.*

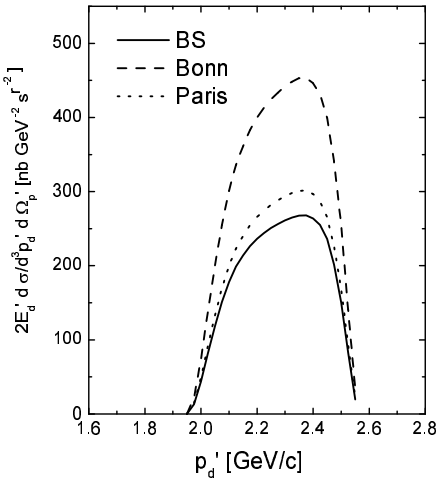

Fig. 2 *Differential cross section of the reaction $pd \to d\phi p_{sp}$ as a function of the deuteron momentum p'_d at $p_p = 3.505$ GeV/c, $\theta_{d'} = 0^o$, $\theta_{p'_{sp}} = 130^o$. The full curve is based on our solution of the Bethe-Salpeter equation, while dashed and dotted curves use Bonn and Paris deuteron wave functions.*

[1] H. Calén et al., Phys. Rev. Lett. 79 (1997) 2642, 80 (1998) 2069, Phys. Rev. C 58 (1998) 2667;
R. Bilger et al., Nucl. Phys. A 663 (2000) 1053c; Nucl. Instr. Meth. A 457 (2001) 64;
M. Büscher et al., "Study of ω and ϕ meson production in the reaction $pd \to dVp_{sp}$ at ANKE", proposal #75
[2] L.P. Kaptari, B. Kämpfer, Eur. Phys. J. A 14 (2002) 211
[3] A.I. Titov, B. Kämpfer, B.L. Reznik, Phys. Rev. C 65 (2002) 065202
[4] B. Kämpfer, R. Kotte, C. Hartnack, J. Aichelin, J. Phys. G 28 (2002) 2035c
[5] L.P. Kaptari, B. Kämpfer, S.S. Semikh, nucl-th/0212066

[1] *Department of Physics, University of Perugia, and INFN Sezione di Perugia, via A. Pascoli, I-06100, Italy*
[2] *Bogoliubov Laboratory of Theoretical Physics, JINR, Dubna 141980, Russia*

Measuring the Effect of ϕ Meson Life Time in Proton-Nucleus Collsions [B]

H.W. Barz, B. Kämpfer, M. Zétényi[1]

The study of in-medium properties of hadrons in nuclear matter is an important subject of contemporary strong interaction physics. Over the last decade a dropping in-medium mass has been considered a precursor phenomenon of chiral symmetry restoration. Using QCD sum rules and chiral dynamics the mass change of various hadrons has been predicted. Recent measurements of kaon yields generated in heavy-ion collisions seem to require a drastic reduction of the K^- mass by about 200 MeV in matter while the measured transverse flow hints to a slight increase of the K^+ mass.

The consequence of these changes of the kaon masses is that the decay width of a ϕ meson in matter should dramatically increase. The small vacuum width of 4.4 MeV is due to the small kinetic energy in the dominant K^+K^- and $K^0\bar{K}^0$ channels. If the rest mass of the kaon pair decreases as predicted then the width should increase by an order of magnitude which leads to a ϕ life time of less than 5 fm/c. This would mean that most of the ϕ mesons decay inside the nucleus mainly into kaon pairs. These kaon pairs are usually used to deduce the number of the produced ϕ mesons. However for kaon pairs created inside the reaction zone there is a great chance that at least one particle of the pair is scattered or absorbed, such that they cannot anymore signal their original invariant mass. This effect will strongly depend on the size of the nuclear system and will lead to a characteristic dependence of the ϕ meson yield on the target-mass number A.

To investigate this effect we use the BUU code with the elementary cross sections for ϕ meson production [1] and kaon rescattering and absorption. We calculate the ϕ production for collisions of protons for three target nuclei, ^{12}C, ^{64}Cu and ^{197}Au at a bombarding energy of 2.5 GeV. For the K^+, K^- and ϕ mesons we use the following scalar potentials as a function of the nuclear matter density n:

$$U_\phi = -0.025\, m_\phi \frac{n}{n_0}, \quad (1)$$

$$U_{K+} = 0.04\, m_K \frac{n}{n_0}, \quad (2)$$

$$U_{K-} = -0.39\, m_K \frac{n}{n_0}, \quad (3)$$

$$U_{K-} = -[0.11 + 0.266 \exp(-2.5p/GeV)] \times m_K \frac{n}{n_0}. \quad (4)$$

The strengths of these potentials reflect the general ideas derived from analyses of data and theoretical investigations [2-4]. The momentum dependence in Eq. (4) has been derived in [5]. The decay width of the ϕ meson is assumed to be proportional to the third power of the kaon momenta p in matter.

In the calculation we follow the evolution of the ϕ mesons and in the case of their decay also the evolution of the kaon pairs. We determine the numbers of ϕ mesons that survive together with the number of kaon pairs which do not suffer encounters with other particles. In Fig. 1 we present the cross sections (rescaled by the factor $A^{-2/3}$) calculated without and with the potentials (1-4).

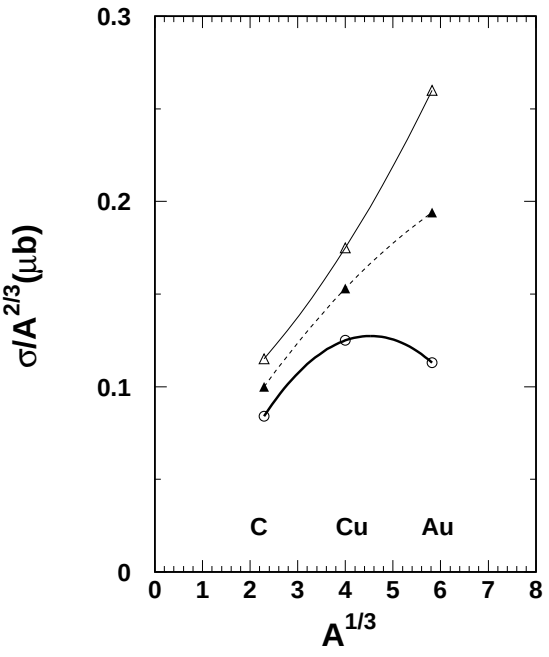

Fig. 1 *The ϕ production cross section in pA collisions as a function of the target mass calculated with momentum independent (thick curve), momentum dependent (dashed curve) and without (thin curve) in-medium modifications.*

The ϕ mesons are dominantly produced in NN and πN collisions. Without inmedium effects the cross section approximately scales with the mass number (thin curve). In very light nuclei like ^{12}C ϕ decay and rescattering does not play an essential role. However in large nuclei like gold the expected number of ϕ mesons is strongly suppressed which leads to the decrease of the yield. We conclude that such measurements are an independent tool to reveal meson properties in nuclear matter.

[1] H.W. Barz, M. Zétényi, Gy. Wolf, B. Kämpfer, Nucl. Phys. A 705 (2002) 223
[2] E.L. Bratkovskaya and W. Cassing, Phys. Rep. 308 (1999) 65
[3] F. Klingl, T. Waas, W. Weise, Phy. Lett. B 431 (1998) 254
[4] T. Hatsuda, H. Shiomi, H. Kuwabara, Prog. Theor. Phys. 95 (1996) 1009
[5] A. Sibirtsev, W. Cassing, Nucl. Phys. A 641 (1998) 476

[1] *KFKI Budapest, Hungary*

Nucleon-K^+ Correlations in Deuteron Induced Collisions with Nuclei at Intermediate Energies [B]

H.W. Barz, F. Dohrmann, E. Grosse, B. Kämpfer

Recently it was proposed to study neutron induced kaon production on nuclear targets. Since neutron beams are not available one may use deuteron induced reactions by measuring the correlation of the produced kaon with the high momentum proton. It is assumed that the high energetic nucleon will be a spectator nucleon from the deuteron while its partner enters the target and produces the kaon. Such an investigation is expected to reveal information about the elementary neutron cross-sections for kaon production which are poorly known from available data. Moreover, current theoretical predictions are very uncertain as the kaon production proceeds via pion or strangeness transfer. Due to this complicated mechanism relations between proton and neutron cross-section on a baryon , e.g. via isospin reflection, cannot be derived in a parameter free manner.
Several elementary reactions contribute to the kaon production within the nucleus, mainly NN and πN collisions. E.g. N-N collisions contribute to 60(70)% of the kaon yield in p+C collisions at 1.6(2.0) GeV. The variety of contributing channels will make it very challenging to relate the difference between neutron and proton induced collisions to specific channels. The comparison of results using neutron as well as proton rich targets could increase the sensitivity to the different cross sections.

Here we study deuteron induced collisions at 2 A·GeV within a Boltzmann-Ühling-Uhlenbeck (BUU) transport model which has been furnished with the elementary cross sections given in refs. [1,2] and kaon rescattering processes. The BUU model requires the knowledge of the spatial and the momentum distribution of the incoming deuteron. We have used a Hulthen wave-function $\Psi = \frac{1}{r}(\exp(-\kappa r) - \exp(-a\kappa r))$ and its Fourier transformation to derive these distributions. The parameter used are κ=0.231 fm^{-1} and $a = 6.16$.

To illustrate the effect that may be expected when using these cross sections, we calculated the multiplicity N_K of kaons when bombarding the target with neutrons or protons, respectively. For the average impact parameter we get for the ratio N_K(p+A)/N_K(n+A) the values 1.25 and 1.27 for a ^{12}C and a ^{40}Ca target, respectively.

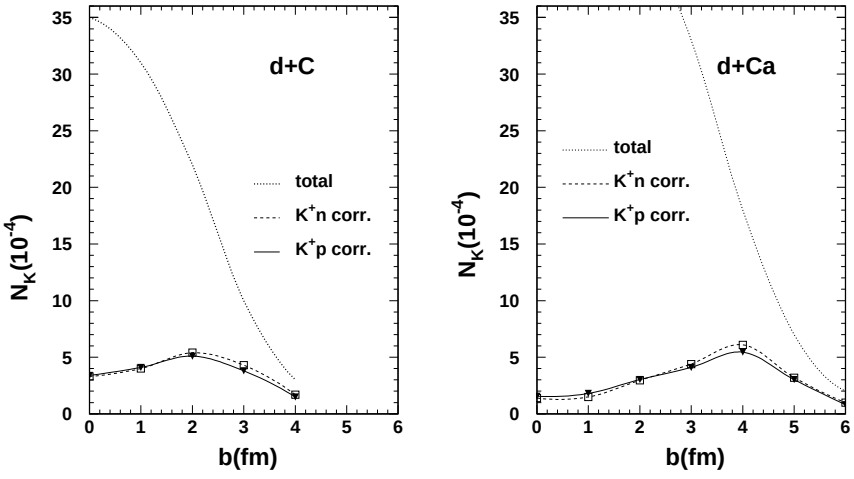

Fig. 1 *Uncorrelated kaon multiplicity (dotted line) and in correlation with a forward neutron or proton as a function of impact parameter b for the reactions d+C and d+Ca at 2 A·GeV bombarding energy.*

The multiplicity of kaons in coincidence with a nucleon (proton or neutron) going in forward direction with a maximum transverse momentum of 0.2 GeV/c and a longitudinal momentum larger than half of the incoming deuteron momentum is calculated. These multiplicities are presented in Fig. 1 together with the total kaon multiplicities (dotted lines) for collisions with carbon and calcium targets. The multiplicities clearly show a maximum for peripheral collisions with impact parameters equal to the target radius. The total kaon cross-section amounts to 0.8 mb (2.2 mb) for C(Ca). The correlated cross sections are smaller by about a factor of five. The ratio of the neutron to proton correlated kaon production is 1.1 and 1.12 for C and Ca, respectively. This means that when measuring the kaons in deuteron induced collisions in coincidence with a leading neutron (proton) the difference of the kaon rates between a proton and a neutron beam is strongly diminished. We expect a similar reduction if the actual cross section could be used. Hence the expected effect is very small. Calculations using stricter selection criteria for the forward particles (Δ p$_\perp$ = 0.05 GeV/c) did not essentially enhance this effect.

[1] Gy. Wolf, W. Cassing, U. Mosel, Nucl. Phys. A 552 (1993) 549
[2] K. Tsushima, J.W. Huang and A. Faessler, Austr. J. Phys. 50 (1997) 35
[3] K. Tsushima, A. Sibirtsev, A.W. Thomas G.Q. Li, Phys. Rev. C 55 (1999) 369

Strangeness Saturation: Dependence on System-Size, Centrality and Energy within the Thermal Model [B]

J. Cleymans[1], B. Kämpfer, P. Steinberg[2], S. Wheaton[1]

The abundances of different hadronic species in the final state of relativistic heavy-ion collisions can be well described by statistical-thermal models. Thus the observed multiplicities of a large number of hadrons can be reproduced by a small number of parameters. It is the subject of the present note to pursue this idea and to analyze the dependence of the thermal parameters, describing hadron multiplicities, on system size, centrality and energy. This will provide further information about the effects of the size of the excited strongly interacting system created at various beam energies.
The primary hadron number of species i is

$$N_i^{\rm prim} = V g_i \gamma_s^{|S_i|} \int \frac{d^3p}{(2\pi)^3}\, dm_i\, {\rm e}^{\frac{E(m_i,p)-\vec{\mu}_i\vec{Q}_i}{T}} \times BW(m_i,\Gamma_i), \quad (1)$$

where V is a fiducial volume of the system, T denotes the temperature, $\vec{\mu}_i$ and $\vec{Q}_i$ stand for the chemical potentials and corresponding conserved charges; BW is the Breit-Wigner distribution for hadron i with total width Γ_i. Eq. (1) is to be improved by the quantum statistical factors. For small values of $N_i^{\rm prim}$, the canonical expression is to be employed by the projection method. We include phenomenologically a strangeness suppression factor γ_s for hadrons with the total number S_i of strange valence quarks. The final particle numbers are $N_i = \sum_j [N_i^{\rm prim} Br(i \to j) + N_j^{\rm prim} Br(j \to i)]$ due to decays of unstable particles with branching ratios $Br(j \to i)$.
We have analyzed data of NA49 [1] (4π and mid-rapidity multiplicities of $\pi^{\pm}$, $K^{\pm}$, $N_{\rm part}$ [taken as sum over all baryons; partially also $\bar{p}$, ϕ, Λ, $\bar{\Lambda}$, $\Xi^{\pm}$ and K^0_s are included] in collisions C+C, Si+Si, Pb+Pb at beam energies 40, 80 and 160 AGeV; it should be emphasized that protons are not included in our analysis as they due not belong to participants in non-central collisions) and PHENIX [2] ($\pi^{\pm}$, $K^{\pm}$, $p^{\pm}$ in collisions Au+Au at $\sqrt{s_{NN}} = 130$ GeV). Results of our fits are displayed in figs. 1 - 3. Fig. 1 (for fully phase space integrated yields) exhibits that strangeness saturation for peripheral lead-on-lead collisions differs from that in collisions C+C and Si+Si. The strangeness saturation increases with centrality. Fig. 2 reveals again the increase of strangeness saturation with centrality; the strangeness saturation at mid-rapidity is larger than in full phase space. Fig. 3 summarizes the energy dependence. f_2 is the fraction of multiply interacting nucleons calculated in a Glauber model. For further details see [3].

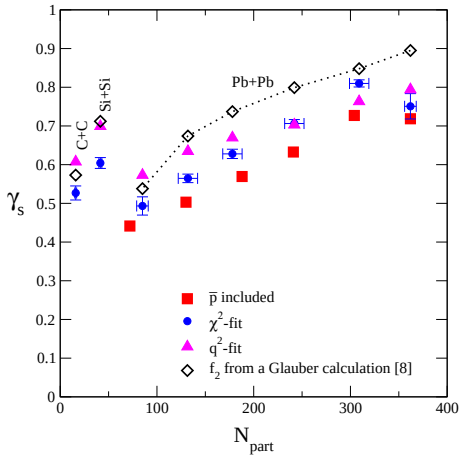

Fig. 1 *System-size and centrality dependence of γ_s as a function of the participant number $N_{\rm part}$, for the beam energy of 160 AGeV.*

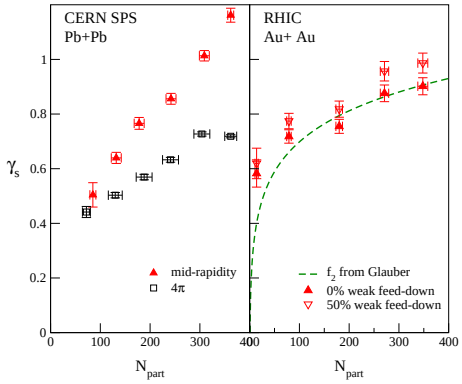

Fig. 2 *Centrality dependence of γ_s for the beam energy of 160 AGeV (left panel) and $\sqrt{s_{NN}} = 130$ GeV (right panel).*

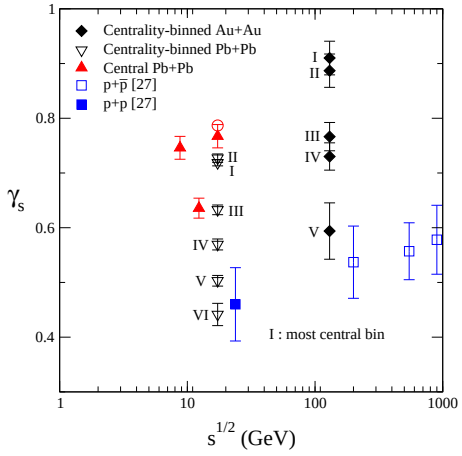

Fig. 3 *Energy dependence of γ_s. For details consult [3].*

[1] F. Sikler et al. (NA49), Nucl. Phys. A 661 (1999) 45c, C. Höhne et al. (NA49), nucl-ex/0209018
[2] K. Adcox et al. (PHENIX), Phys. Rev. Lett. C 66 (2002) 054902
[3] J. Cleymans et al., Phys. Rev. C 65 (2002) 027901, hep-ph/0203134, hep-ph/0204227, hep-ph/0208247, hep-ph/0212335

[1] *University of Cape Town, Rondebosch 7701, Cape Town, South Africa*
[2] *Brookhaven National Laboratory, Upton, NY, USA*

Energy Loss of Charm Quarks by Gluon Radiation [B]

K. Gallmeister[1], B. Kämpfer, O.P. Pavlenko[2]

Induced gluon radiation of a fast quark propagating through a deconfined medium of quarks and gluons causes an energy loss which should considerably modify various observables in relativistic heavy-ion collisions. In such a way the properties of the deconfined medium can be probed. The modified transverse momentum spectrum of final hadrons appears as a convolution of the energy loss distribution and the primary spectrum. To enable a comparison with earlier work [1], we employ here a simplified version by using a Monte Carlo averaging over tranversed path lengths and by shifting the transverse momentum of a quark before hadronizing by the mean energy loss. Remarkable in the energy loss formula is the apparent independence of the initial state, i.e. the energy loss depends on the temperature T_f at which the quark leaves the medium. As shown in [2], however, due to life time and geometrical size effects, a sensitivity on the initial conditions occurs.

Using the PYTHIA version 6.206 with parameters given in [3] one gets the charm cross section $\sigma_{c\bar{c}}^{NN} = 404$ μb at $\sqrt{s_{NN}} = 130$ GeV. With the electron/positron decay channels of charmed hadrons within PYTHIA the resulting inclusive transverse momentum spectrum agrees fairly well with the PHENIX data [4] when using the appropriate thickness functions $T_{AA} = 6.2$ (22.6) mb^{-1} for minimum bias (central) collisions, see fig. 1.

To see which space is left for an energy loss we use the above described scheme with Bjorken symmetries and parameters decsribed in [3]. We parameterize different energy loss strengths by ζ multiplying the energy formula used in [1,2,3]. The results of our Monte Carlo sampling are exhibited in fig. 2. An optimum description of the data is accomplished by $\zeta = 0.2 \cdots 0.5$. It turns out, however, that larger energy losses are also compatible with data, as no energy loss does. Insofar, the present data do not constrain significantly the energy loss of charm quarks.

Energy loss effects can suppress the dileptons from charm decays [1]. This is a potentially important effect since these charm contributions compete with the Drell-Yan yield and hide the interesting thermal contribution. Given the above parameterization of the modifications of inclusive single electrons by energy losses of charm quarks, we proceed to estimate the possible suppression of dileptons from correlated semi-leptonic decays of open charm mesons. Our predictions are displayed in fig. 3 for various values of the strength parameter ζ. Indeed, the dilepton spectra are quite sensitive to energy losses, however, assuming a small loss, as suggested by the above analysis, the corresponding suppression is small.

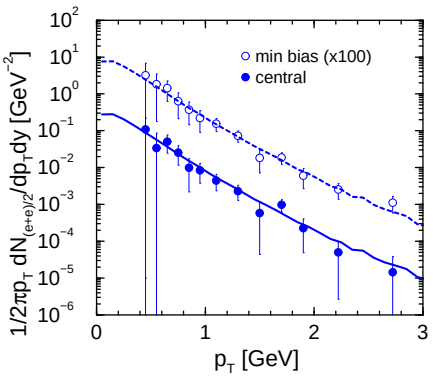

Fig. 1 *Comparison of our PYTHIA results with the PHENIX data [4] (statistical and systematical errors are quadratically added).*

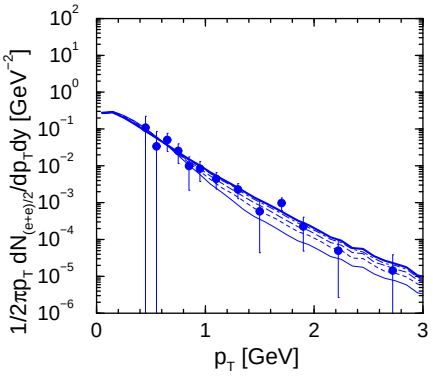

Fig. 2 *Comparison of various energy loss strengths $\zeta = 0$, 0.2, 0.5, 1.0, 2.0 (from top to bottom) with PHENIX data [4] of central collisions. For details see [3].*

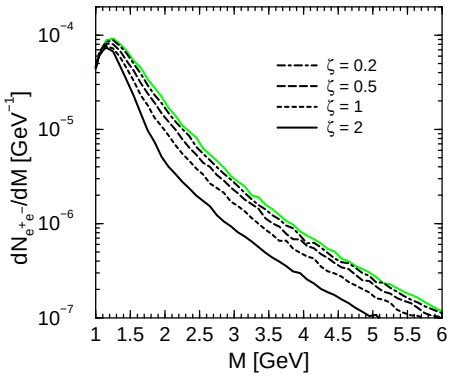

Fig. 3 *Predicted dilepton spectra from open charm mesons for various strength parameters of the energy loss within the PHENIX acceptance. $T_{AA} = 31$/mb, $\sqrt{s_{NN}} = 200$ GeV. Single-lepton $p_\perp^{\min} = 0.5$ GeV/c.*

[1] K. Gallmeister, B. Kämpfer, O.P. Pavalenko, Phys. Rev. C 57 (1998) 3276
[2] K. Gallmeister, B. Kämpfer, O.P. Pavalenko, Phys. Rev. C 66 (2002) 014908
[3] K. Gallmeister, B. Kämpfer, O.P. Pavalenko, nucl-th/0208006, Nucl. Phys. A (2003) in print
[4] K. Adcox et al. (PHENIX), Phys. Rev. Lett. 88 (2002) 192303

[1] *Institute für Theoretische Physik, Universität Giessen*
[2] *Institute for Theoretical Physics, Kiev, Ukraine*

Relativistic Effects in Deuteron Break-Up Reactions [B]

L.P. Kaptari[1], B. Kämpfer, S.S. Semikh[2], S.M. Dorkin[3]

Recently, data on proton-induced deuteron break-up at intermediate energies with forward emission of a fast proton pair has been reported [1]. One motivation for the experiment was the possibility to investigate the off-mass shell effects in NN interactions [2]. As predicted in [1],[3], at a certain initial energy of the beam protons, the cross section should exhibit a deep minimum, corresponding to the node of the non-relativistic $^1S_0$ wave function of the two outgoing protons, provided a non-relativistic picture holds and off-mass shell effects can be neglected. The data [1] exhibits, however, a completely different behavior: the cross section is smoothly decreasing; there is no sign of a pronounced minimum.

In the present note we use the Bethe-Salpeter (BS) approach to analyze the data [1] on deuteron break-up with the emission of a fast forward pp pair. The calculation is based on our solution of the BS equation for the deuteron with a realistic one-boson exchange kernel. The final state interaction of the two protons is treated also within the BS formalism, by solving the BS equation for the t matrix within the one-iteration approximation.

Let us consider the process

$$p + d = (p_1 p_2)(0^0) + n(180^0) \qquad (1)$$

at low excitation energy of the pair ($E_x \sim 0 - 3$ MeV) and intermediate initial kinetic energies $T_p \sim 0.6 - 2.0$ GeV corresponding to the conditions at the Cooler Synchrotron COSY in the ANKE experiment [1]. In the one-nucleon exchange approximation the reaction can be represented by the diagram depicted in fig. 1. With the theory described in detail in [4] we obtain for the differential cross section results as depicted in fig. 2. A non-relativistic calculation and a constraint relativistic calculation exhibit, indeed, the expected minimum. The full calculation [4] reveals, however, that the complete set of necessary relativistic effects fully masks the expected minimum. The experimental results are then correctly described, see fig. 3.

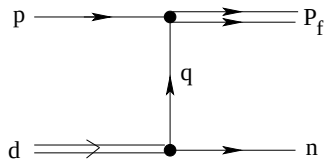

Fig. 1 *Kinematics of the process $pd \to (pp) + n$ corresponding to the experiment [1,2].*

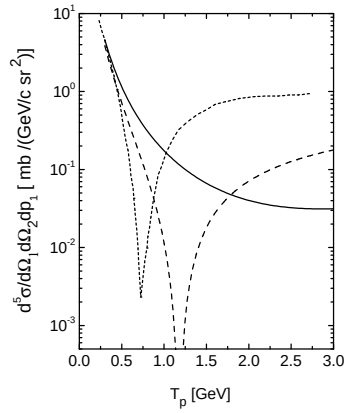

Fig. 2 *Five-fold cross section as a function of the kinetic energy T_p of the incident proton. The dotted curve corresponds to a non-relativistic calculation, i.e., to the case where only the "++" components in the $^1S_0$ state are taken into account and any Lorentz boost effects are ignored. The dashed curve depicts results of a calculation with all relativistic effects in "++" components. The solid curve is for the results of a complete calculation with taking into account all the relativistic effects including the contribution of P waves in the wave function of the pp pair. The two protons are supposed to be detected in forward direction.*

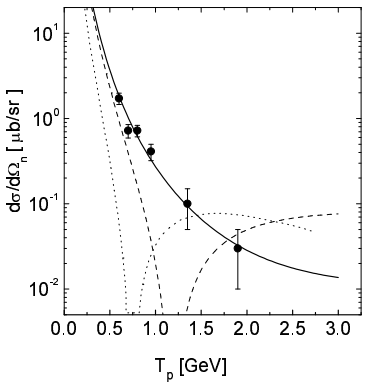

Fig. 3 *Differential cross section in the center of mass integrated over the excitation energy E_x as a function of the kinetic energy T_p of the incident proton. Notation is as in fig. 2. Experimental data are from [1].*

[1] V.I. Komarov et al., nucl-ex/0210017

[2] V.I. Komarov (spokesman) et al., COSY proposal #20 (updated 1999), "Exclusive deuteron break-up study with polarized protons and deuterons at COSY"

[3] Yu.N. Uzikov, V.I. Komarov, F. Rathmann, H. Seyfarth, nucl-th/0211001; Yu.N. Uzikov, J. Phys. G28, B13 (2002)

[4] L.P. Kaptari, B. Kämpfer, S.S. Semikh, S.M. Dorkin, nucl-th/0212062

[1] *Department of Physics, University of Perugia, and INFN Sezione di Perugia, via A. Pascoli, I-06100, Italy*
[2] *Bogoliubov Laboratory of Theoretical Physics, JINR, Dubna 141980, Russia*
[3] *Nuclear Physics Institute, Moscow State University, Moscow, Russia*

Exclusive Charge-Exchange Reaction $pD \to n(pp)$ within the Bethe-Salpeter Formalism [B]

L.P. Kaptari[1], B. Kämpfer, S.S. Semikh[2], S.M. Dorkin[3]

At the cooler synchrotron COSY in FZ Jülich, a program to study charge-exchange processes at relativistic energies has been started, and a detailed investigation of polarization observables is envisaged. Details of the deuteron wave function at short distances and the relevant reaction mechanisms can be investigated in inclusive deuteron break-up reactions.

Inspired by this, in previous work [1] we investigated the process $p\vec{D} \to n(pp)$ within the impulse approximation. The goal of the present note is to report results of our improved study [2] of the charge-exchange reaction at relativistic energies, as accessible at COSY and the upgraded Dubna accelerator by (i) taking into account the effects of final state interaction, (ii) to check whether in this case the non-relativistic predictions hold, and (iii) whether the reaction can be used as a "deuteron polarimeter". We employ a covariant generalization of the spectator mechanism (see fig. 1) based on the Bethe-Salpeter (BS) formalism and on a numerical solution of the BS equation with a realistic one-boson exchange kernel. Our amplitude of the process in an explicitly covariant form allows a determination of any polarization observable.

To test our approach, in figs. 2 and 3 we compare with experimental data from SATURN-II. The agreement is satisfactory, in particular for small excitation energies of the slow backward (pp) pair (the fast forward neutron is not detected). This gives confidence that also at COSY energies the reaction is correctly described within our formalism. The predicted cross sections [2] are large enough to use the considered reaction as "deuteron polarimeter", as proposed in [4].

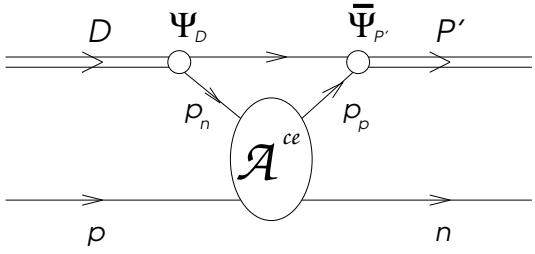

Fig. 1 *Spectator mechanism for the charge-exchange process $pD \to n(pp)$. The BS amplitude for the deuteron bound state and the pp pair in the continuum are denoted as Ψ and $\bar{\Psi}$, respectively. The elementary pn charge-exchange amplitude is symbolically represented by $\mathcal{A}^{ce}$.*

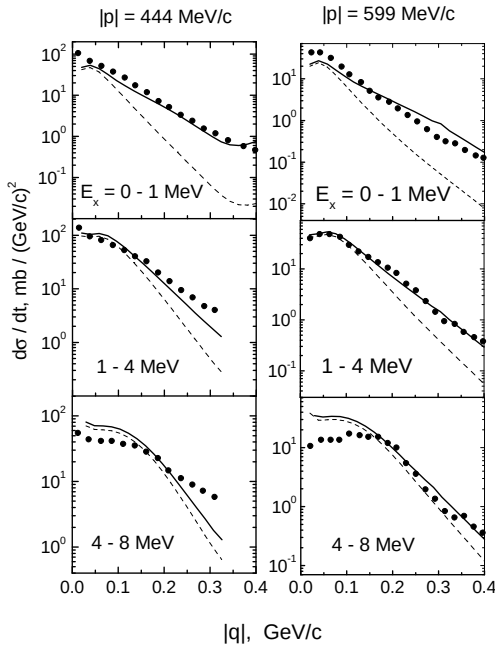

Fig. 2 *Results of calculations of the differential cross section as a function of the transferred momentum with taking into account the effects of final state interaction in the (pp) $^1S_0$ state (solid curves). Experimental data from SATURN-II [3]. The dashed curves depict the results of calculations within the impulse approximation.*

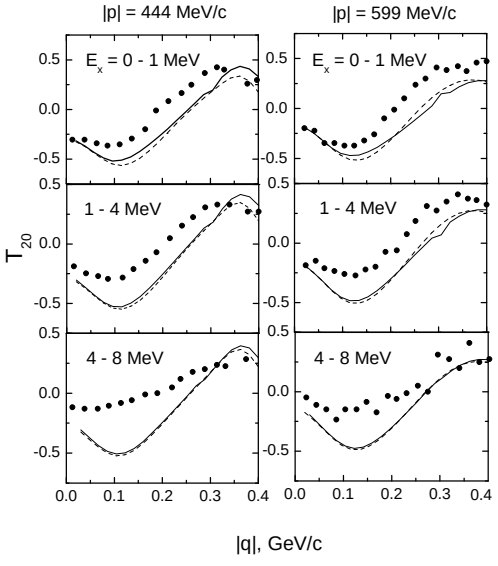

Fig. 3 *The same as in fig. 2 but for the tensor analyzing power.*

[1] S.S. Semikh, S.M. Dorkin, L.P. Kaptari, B. Kämpfer, Yad. Fiz. 65 (2002) 469
[2] L.P. Kaptari, B. Kämpfer, S.S. Semikh, S.M. Dorkin, nucl-th/0211076, Eur. Phys. J. A (2003) in print
[3] S. Kox et al., Nucl. Phys. A 556 (1993) 621
[4] D.V. Bugg, C. Wilkin, Phys. Lett. B 152 (1985) 37; Nucl. Phys. A 467 (1987) 575

[1] *Department of Physics, University of Perugia, and INFN Sezione di Perugia, via A. Pascoli, I-06100, Italy*
[2] *Bogoliubov Laboratory of Theoretical Physics, JINR, Dubna 141980, Russia*
[3] *Nuclear Physics Institute, Moscow State University, Moscow, Russia*

From QCD Lattice Calculations to the Equation of State of Quark Matter [B]

A. Peshier[1], B. Kämpfer, G. Soff[2]

One of the fundamental issues which triggered, and has influenced since, heavy ion physics is the phase structure and the thermodynamic properties of strongly interacting matter at energy densities above $1\,\mathrm{GeV/fm^3}$. Under such conditions, exceeding the energy density in nuclei but still far away from the asymptotic regime, the coupling strength is large, which makes the theoretical description of the many-body problem challenging.

In the recent past the understanding of this field has become much more particularized. The phase diagram for QCD with two massless flavors, which is the case we will consider in the following, can be briefly described as follows. At zero quark chemical potential, $\mu = 0$, the broken chiral symmetry of hadron matter is restored within the quark-gluon plasma, at a critical temperature $T_c \approx 170\,\mathrm{MeV}$. It is thought that this second order transition persists also for nonzero μ, thus defining a critical line, which changes to a first order transition line at the tricritical point. For small temperatures and $\mu \sim \mu_c$ one anticipates a color-superconducting phase of quark matter. The value of μ_c is expected to be 100...200 MeV larger than the quark chemical potential $\mu_n = 307\,\mathrm{MeV}$ in nuclear matter. Quantitative results for large couplings can be obtained from first principles by lattice calculations which were, however, restricted to finite temperature and $\mu = 0$ until very recently. Therefore, the described picture for $\mu \neq 0$ is mainly based on general arguments combined with results from various models, including first lattice QCD results [1,2].

With respect to the starting Compressed Baryon Matter project at GSI a semi-quantitative determination of the phase border line is important. We report here results of our quasi-particle model [3] to accomplish this goal.

Our model is based on dynamically excited quark and gluon modes near the light cone. The quasi-particle excitations determine the entropy density, which delivers the pressure and energy density in a thermodynamically self-consistent manner. A crucial ingredient is the effective coupling to be adjusted at lattice data. Fig. 1 exhibits an example of the pressure at $\mu = 0$.

The extrapolation to finite baryon density is based on a thermodynamic self-consistency condition and a extremum property of the potential. The emerging characteristics are shown in fig. 2. The innermost characteristic joining the chiral transition temperature T_c is considered as representative of the phase border line. It also quantifies the numerical value of the critical baryo-chemical potential.

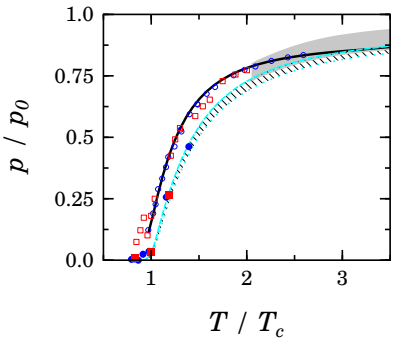

Fig. 1 *Compilation of $n_f = 2$ lattice data for the pressure in units of the free pressure p_0. Shown are the scaled data [4] for light quarks corresponding to meson mass ratios of $0.65 \leq m_{ps}/m_v \leq 0.75$ (small open circles: $N_\tau = 4$, small open squares: $N_\tau = 6$), and a continuum estimate (grey band). The full line is our quasi-particle result. The full symbols depict the data [4] for larger quark masses, with $m_{ps}/m_v = 0.95$. The hatched band represents the pure SU(3) lattice data normalized to the corresponding free pressure. For details see [5].*

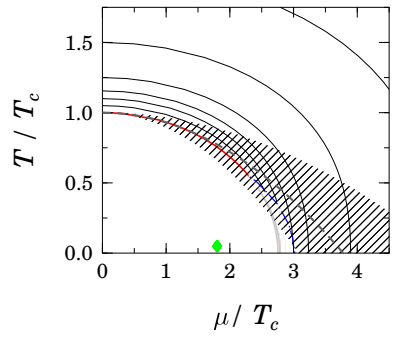

Fig. 2 *Represented by the full lines are the characteristics. The characteristic through T_c coincides for small μ with the critical line (with a hatched error band) obtained in the lattice calculation [2]. In the region under the dash-dotted line the resulting quasi-particle pressure is negative – a transition to another phase has to happen somewhere outside. Therefore, the narrow grey region under the $p = 0$ line, where the pressure is not unique, is physically irrelevant. Indicated by the symbol (assuming, for the scaling, $T_c = 170\,\mathrm{MeV}$) is the chemical potential μ_n in nuclear matter. The equation of state follows from our model in the region covered by the characteristics.*

[1] Z. Fodor, S.D. Katz, JHEP 0203 (2002) 014
[2] C. R. Allton et al., hep-lat/0204010
[3] A. Peshier, B. Kämpfer, O. P. Pavlenko, G. Soff, Phys. Rev. D 54 (1996) 2399;
A. Peshier, B. Kämpfer, G. Soff, Phys. Rev. C 61 (2000) 045203
[4] A. Ali Khan et al., Phys. Rev. D 64 (2001) 074510
[5] A. Peshier, B. Kämpfer, G. Soff, Phys. Rev. D 66 (2002) 094003

[1] *Institute für Theoretische Physik, Universität Giessen*
[2] *Institute für Theoretische Physik, TU Dresden*

Quality Assessment for Monitoring of HADES DST Production

A. Sadovski, F. Dohrmann, K. Kanaki, R. Kotte, D. Magestro[1], C.Müntz[1], L. Naumann

The purpose of HADES Quality Assessment (QA) is to provide diagnostic tools (histograms and scalers) during Data Summary Tape (DST) production in order to help assess the quality of the data for higher levels of physics analysis. Initially the program was modelled after the STAR QA/QC (quality assurance/quality control) package [1]. At the moment the program includes 92 diagnostic plots, several of these are overlays (see Fig. 1). Each physical detector of the HADES setup as well as two logical units, Kickplane and Trigger, are covered. The program is open for additional diagnostic plots.
QA works in parallel with DST production and creates its output per DST file. The output is stored in several formats, as PDF or PS format, as well as ROOT-file format [2] in order to allow for analysing of multiple outputs with dedicated scripts.

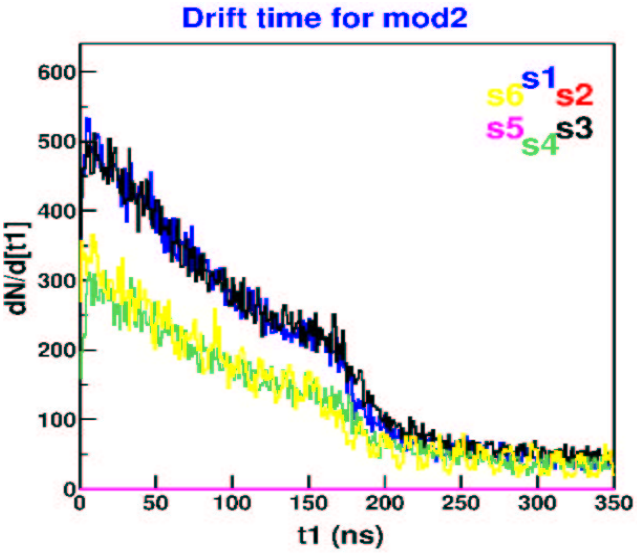

Fig. 1 *An example of overlayed picture from DST-QA PDF output from November 2002 beam time. The plot shows time distribution of the first electron of the signal for four modules MDC-III (sectors 1, 3, 4, 6). The vertical axis units are* (ns^{-1}). *Sectors 4 and 6 have less count rate due to only 4 out of 6 layers being operational.*

Recently two dedicated scripts were written, which allow to perform a semi-automatic analysis of diagnostic plots (see Figs. 2, 3). This is important when dealing with several hundreds of QA files. The main idea is to give the detector expert a possibility to preselect several good histograms manually and then to compare all the remaining files with this reference pattern and accept/reject any of others. This procedure is iterative. One automatic iteration takes about 40 seconds for a one-dimensional histogram over 231 files on a modern Linux cluster. At the moment it uses the mean value distribution of each one-dimensional histogram to select histograms. Experts from different detector groups are supposed either to provide the reference histograms or may evaluate files with histograms corresponding to the respective detector. Finally, the results from different detector groups are to be grouped together in a DST-QA report.
The next step of HADES DST-QA is to make preselection of histograms/files more automatic by providing a set of reference plots and to develop adequate selection criteria for respective groups of histograms.

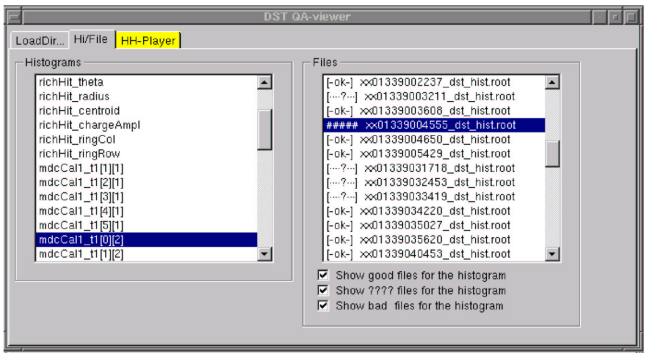

Fig. 2 *Example of the user interface for selection of good and bad histograms among QA output of DST files. A histogram is chosen from the left menu, and the results for this histogram of automatically preselected files with a quality flag (in front of the name of file) are shown in the right menu.*

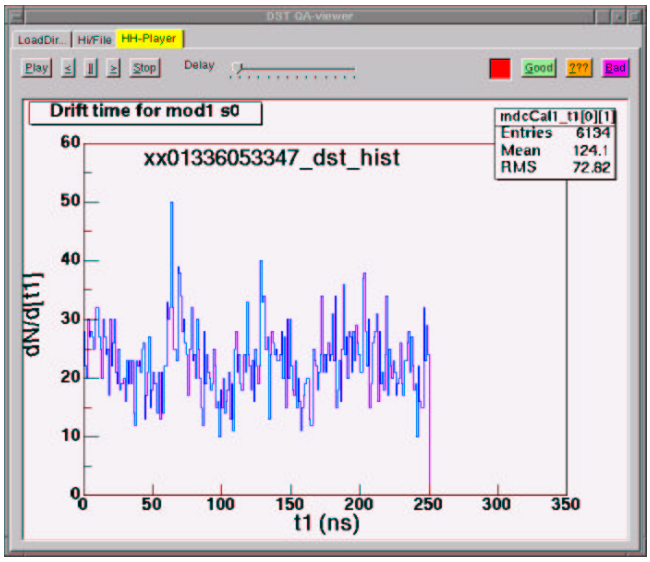

Fig. 3 *Screen shot of the quick histogram player for DST-QA. The histogram shown is MDCII sector 1 has been marked by semi-automatic quality control procedure as a "bad" one (to be compared with the corresponding reference plot). The user can always change the assigned quality flag for the histogram of the current file manually in case it was not correctly set by semi-automatic procedure. The control buttons are located at the top of the widget.*

[1] http://www.star.bnl.gov/STARAFS/comp/qa/shifts/QA_general.html
[2] http://root.cern.ch/

[1] *Gesellschaft für Schwerionenforschung mbH, Darmstadt, Germany*

A Method for Separation of Faulty Wire Connections in the HADES Drift Chambers

K. Heidel, J. Hutsch, U. Wolf, K. Kanaki, R. Kotte, L. Naumann

The tracking system of the HADES spectrometer at GSI, Darmstadt consists of four planes of Multiwire Drift Chambers (MDC). Each module contains approximately the same numbers of anode wires (∼1000) which gives us a total of about 27,000 channels.

The stable operation of an MDC module requires constant high voltage on the field and cathode layers. Yet, during the operation, it might be the case that there is a persistent local discharge around a cathode (field) wire C_i (F_i) which can lead to an instant drop of its potential. This abrupt change will lead to an attractive force between wires of sequential layers and quite often to a spark which can provide sufficient energy for the wires to weld.

The origin of this phenomenon was studied using two (dummy) layers of wires at a distance of 4 mm, on which both kinds of electrodes (field wires, Ø = 100 μm; cathode wires, Ø = 80 μm) were strung with the operational tension, i. e. 1.5 N and 1.0 N respectively. The sense wires were not included in the study. With this setup it was proven that a rise of the potential above a certain value may cause wire oscillations and sparks and moreover, even recreate a faulty connection between the layers. Here we have to point out that in the case of the dummy frames, what we have is rather a superficial attachment than welded wires, meaning that a mechanical vibration is often sufficient to cure the faulty connection. No external damage on the surface of the wire was observed.

From high-frequency engineering it is known that sparkover paths can be repaired with the help of high voltage pulsers. This method would be suitable for the repair of the faulty connection in our case. Furthermore, a short current pulse can induce a force on the wire.

When we deal with such a case in a chamber installed in the HADES setup, it is always practical and less time consuming to repair the chamber without removing and opening it. Using the above dummy frames, such a method for repairing the faulty connection of the wires was tested. The fundamental idea was to use a time controlled switcher for a pulse source (Fig. 1).

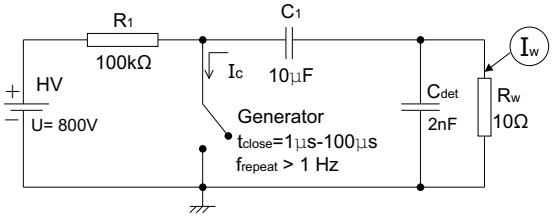

Fig. 1 *Time controlled high voltage switcher.*

Keeping the switch closed, the charged capacitor discharges on the connection of the two Al wires through the resistivity $R_w \sim 10\ \Omega$. The simulated discharge current for the time constant of $\tau = R_w C_1 \simeq 100\ \mu$s is depicted in Fig. 2. For flexibility purposes a generator is used in order to vary the duration time t_{close} and the pulse repetition rate f_{repeat}.

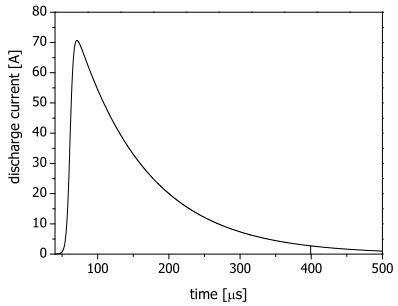

Fig. 2 *Plot of the simulated discharge current as a function of time.*

Experience showed that a duration of $t_{close} = 10\ \mu$s and frequencies f_{repeat} higher than 1 Hz are appropriate. A glow lamp (not shown in the circuit) signalizes the successful separation of the wires. The electric energy (Fig. 3) for the above circuit was simulated with PSpice [1] and was calculated from the time integral of the electric power as

$$W = \int_0^{t_{close}} U_w I_w dt. \qquad (1)$$

For $t_{close} = 10\ \mu$s and $U = 800$ V the dissipated energy is $W \simeq 0.5$ J while the theoretical curve

$$E(t) = \int_0^t P(t')dt' = \frac{\tau U_{max}^2}{2R_w}\left(1 - e^{-2t/\tau}\right), \qquad (2)$$

also calculated by integration, gives $E = 0.6$ J.

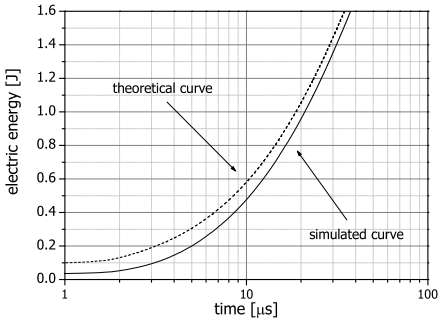

Fig. 3 *Overlay of theoretical and simulated curve of the dissipated electric energy as a function of time.*

In contrast to the direct heating method [2] which induces energies of about 25 J on the wire connection, the short energy pulses provide safety against smelting wires.

[1] http:/www.pspice.com
[2] http://www-hades.gsi.de/proceedings/collmeetXI/jboy1/jboy1.html

Examination of the Wire Deflections for the HADES Drift Chambers MDC III

K. Kanaki, J. Hutsch, F. Dohrmann, R. Kotte, L. Naumann, A. Sadovski, M. Sobiella

From the mechanical point of view, an operational drift chamber requires wires strung with tension high enough to avoid sagittas and oscillation amplitudes which are comparable to the distance between the layers of the wires. Simulations and tests were performed before the construction of the HADES modules, in order to define the right value for this force that will compensate for gravity. Apart from the gravitational forces, the wires are also subject to electrostatic forces that tend to displace them, when voltage is applied. The combined effect of these forces and of the restoring mechanical tension results in an elastic deformation of the wire. The wire deflection from the nominal position can be estimated with the program GARFIELD [1] by solving the differential equation which describes its equilibrium state.

The differential equation describing the shape $y(x)$ of a wire (x runs along its length) subjected to an external force $f(x)$ can be derived by making the following assumptions:

- the wire deflection is small compared to the length of the wire
- the wire elongation is in the elastic range of the Hooke's law.

If the wire is stretched under tension T and has a shape $y(x)$, the force per unit length F_t acting on an elementary part of the wire between x and dx is given by:

$$F_t(x)dx = T\Big(\frac{dy}{dx}\Big)_{x+dx} - T\Big(\frac{dy}{dx}\Big)_x = T\frac{d^2y}{dx^2}dx. \quad (1)$$

This is the force that tends to restore the wire back to its nominal position and balances any external applied force. The gravitational force per unit length acting on the wire is $F = g\rho\sigma$, where ρ is the density of the wire and σ its cross section, while the electrostatic force is $F = \lambda E$, where λ is the charge per unit length and E the electric field generated by the surrounding electrodes. If the field is constant, it creates a constant force per unit length, similar to the gravitational one. For a wire placed in a position of electrostatic equilibrium, a small deviation from this position generates a force acting on the wire tending to displace it. This force has the form $F = \frac{V^2}{2}\frac{dC}{dx}$, where V is the potential of the wire and dC/dx the variation of its capacitance per unit length due to displacement [2]. It can be shown that

$$F \simeq \frac{V^2}{2}\frac{4\pi\epsilon_0}{[\alpha ln(\alpha/r)]^2}x = ky \ (k = const), \quad (2)$$

where r is the radius of the wire and α the typical distance of the wire from the other electrodes. Thus, the equation describing the equilibrium position of the wire is

$$T\frac{d^2y}{dx^2} = -ky - g\rho\sigma = f(x). \quad (3)$$

For $k = 0$ we can study separately the effect of gravity. Integrating for the total wire length L, the sagitta is

$$s_g = \frac{L^2 g\rho\sigma}{8T}, \quad (4)$$

and is proportional to the inverse of the mechanical tension T. If T is increased, the effect is reduced but it cannot be arbitrarily increased, since non-elastic deformations take place. The total sagitta of the wire under the combined effect of electrostatic and gravitational forces is

$$s = \frac{8s_gT}{L^2k}\Big(\frac{1}{cos\sqrt{k/T}(L/2)} - 1\Big) = s_g\frac{2}{q^2}\Big(\frac{1}{cosq} - 1\Big). \quad (5)$$

It is clear that the electrostatic forces amplify the sagitta produced by the gravitational forces. From the above equation we can deduce the stability condition

$$q^2 = \frac{4\pi\epsilon_0}{[\alpha ln(\alpha/r)]^2}\frac{U^2}{2T}\frac{L^2}{4} \leq 1. \quad (6)$$

The above relation allows us to calculate the critical tension T_c ($q^2 = 1$) for fixed parameters U, L, α and r, below which the wires oscillate under working conditions (see Tab. 1).

wire	Ø [μm]	T_c [N]	T [N]	material
sense	20	0.31	0.5	W
cathode	80	0.65	1.0	Al
field	100	0.72	1.5	Al

Tab. 1 *Summary table of all wire tensions, actual and critical, calculated for α = 4 mm, L = 2 m and U = -2000 V.*

Following the above we attempted to calculate the sagittas for the sense wires of MDC III as a function of their tension, without varying the potential applied on the field and the cathode wires.

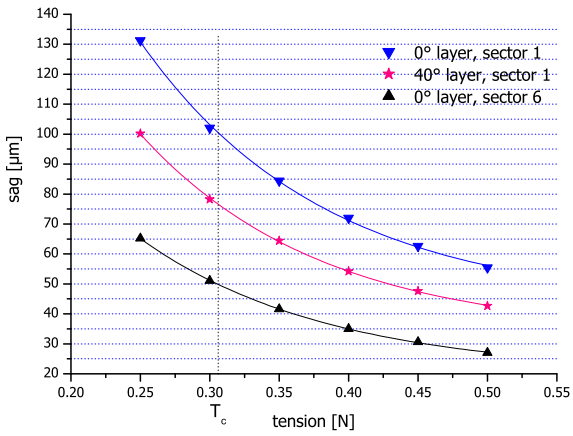

Fig. 1 *Anode wire sagittas for different layers and chamber orientations.*

The calculation was performed for a series of tension values between the strung and the critical one and for different layers and chamber orientations, i. e. for different gravitational sagittas. The results for the anode wires ($U_c = U_f$ = -2 kV) are depicted in Fig. 1.
The plot shows that the sense wires of the 0° layer of sector 1 are subject to the highest deflection from the nominal position. Due to symmetry, the wires of chambers that are installed in opposite sectors have the same deflection. The sagitta is lower for inclined layers and chambers. Nevertheless, for a loss of 20 % in tension, the sagitta does not deviate more than the designed resolution of the modules (100 μm), e. g. for 0.4 N the sagitta of 0° layer in sector 1 is below 80 μm.

The tension which the sense wires (W) are strung with remains constant in the first couple of years of operation, in contrast to the tension of the field and the cathode wires (Al) which decreases approximately 13% within three years due to the creeping process (see Fig. 2). The shape of the curves is stamped by the production process and is not influenced by aging procedures.

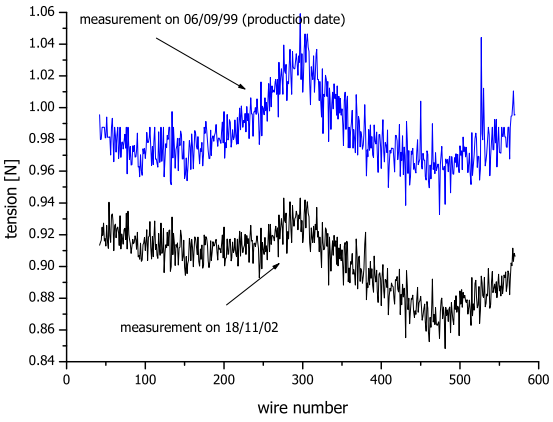

Fig. 2 *Comparison of the cathode wire tension for MDC III measured at different times.*

Apart from the creeping, the deformation of the stesalit frames can cause loss of tension as well. Such a case appears, for example, when the drift chamber is operated under gas overpressure. The mylar foils "swell" causing the stesalit frames to bend inwards. Consequently, the length of the wires changes and so does their tension. Fig. 3 depicts the frame deformation for the 0° layer as a function of gas overpressure, while Tab. 2 gives the tension values calculated for the sense wires of the same layer. The deformation was measured at the points indicated by the arrows in the figure.

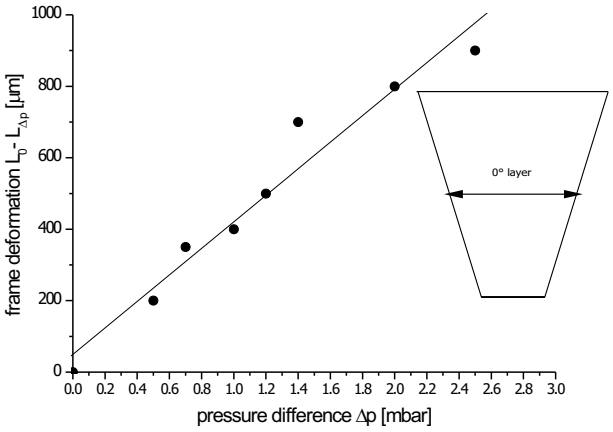

Fig. 3 *Frame deformation for 0° anode layer vs. pressure difference.*

frame deformation [μm]	corresponding tension [10^{-2}N]	change in %
0	50.00	0.00
200	46.44	6.90
350	44.00	12.00
400	43.10	13.80
500	41.40	17.20
700	37.95	24.10
800	36.20	27.60
900	34.50	31.00

Tab. 2 *The change of the anode wire tension depending on the frame deformation.*

A gas overpressure control system assures that the pressure difference will not exceed the value for which the frame deformation will lead to tensions below the critical one.

[1] Simulation of gaseous detectors, http://garfield.web.cern.ch/garfield
[2] W. Blum, L. Rolandi, Particle detection with drift chambers, Springer-Verlag, Berlin (1993)

Momentum-Reconstruction System for ANKE Side Detectors

V. I. Dimitrov, J. Seibert

Recently the ANKE spectrometer [1] at COSY-Jülich has been upgraded with a negative particle detection system [2], consisting of 2 mm thick start scintillators, two MWPCs for momentum reconstruction, two groups of stop scintillators and several bent Čerenkov counters for kaon–pion discrimination for momentum values where TOF differences are too small [3]. With the help of the new detector it is possible to register negatively charged particles with momenta 120...1000 MeV/c. This allows studying π^-−, K^-− and, indirectly, ϕ – meson production. In addition, more complete and precise reconstruction of the reaction kinematics of particles registered in the positive particle detectors of the spectrometer becomes possible. As a part of the development of the appropriate data analysis software for the new detector system, a momentum-reconstruction software package has been designed and tested. The package fulfils the following general requirements:

- Fast operation which makes it possible to use it in online analysis;
- Low system load for seamless coexistence with other analysis tools;
- Implementation as a C++ class for an easy integration into the existing analysis framework;
- Precision consistent with that of ANKE hardware and/or software.

With regard to the above, the chosen implementation uses a GEANT [4] generated, size optimized database of pre-calculated particle tracks, and a fast interpolation engine for evaluating the vertex particle momentum from the MWPC hit coordinates. While GEANT is a well-known standard tool, the scattered data interpolator has to be developed from scratch, as the existing methods for scattered data interpolation (Nearest Neighbor Interpolation, Shepard method etc.) do not meet one or more of the above requirements.

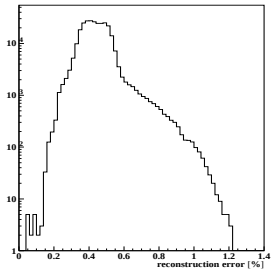

Fig. 1 *Error distribution of the reconstructed momenta. Notice the log scale.*

[1] S. Barsov et al., Nucl. Instr. Meth. A 462 (2001) 364
[2] H.R. Koch et al., FZJ Annual Report (1999) p. 28
[3] M. Büscher et al., Phys. Rev. C 65 (2002) 014603
[4] GEANT: CERN Program Library, Long Writeup W5013

The implementation chosen involves an optimized cell algorithm for locating the N-th nearest neighbour of a node, and a quasi-linear interpolation based on the functional values at the nearest neighbours. A detailed account on the method will be published elswhere.
Figures 1–3 demonstrate the performance of the momentum reconstruction system with simulated data. Checks with real ANKE data are under way.

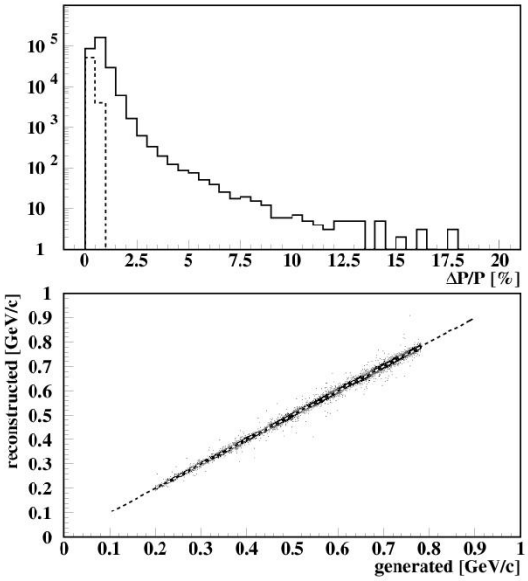

Fig. 2 *Effects of multiple scattering on the precision of the momentum reconstruction. The dashed line shows the resuls without small angle multiple scattering.*

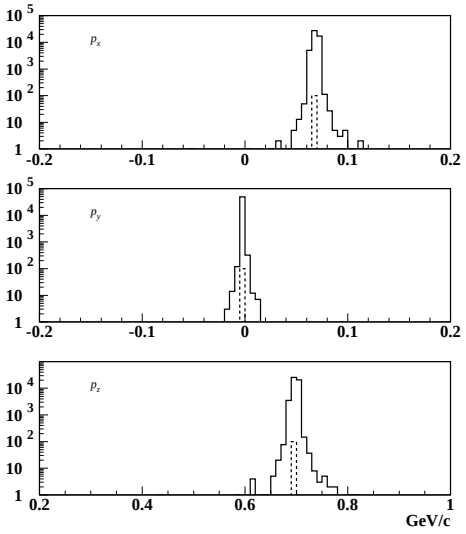

Fig. 3 *Reconstruction of the momentum components of a particle with fixed momentum with (solid lines) and without (dashed lines) small angle multiple scattering.*

ELBE-n-TOF: Comparison to other Neutron Sources and Experiments

E. Grosse, K. Möller, B. Mukherjee, L. Naumann, A. Wagner for the n-TOF collaboration

Neutron interaction cross sections are strongly varying in dependence on neutron energy and mass and charge number of the hit nucleus. Together with the low natural neutron background this makes them an ideal probe for the study of the interior of matter, which they penetrate nearly freely until they hit a high cross section nucleus. Four methods are employed for the production of neutrons in the laboratory i.e. to liberate them from their nuclear binding:

1. nuclear fission, usually accompanied with 2 - 3 neutrons.
2. specific binary nuclear reactions with a neutron in one exit channel.
3. spallation induced by fast (v$\gg$0.25 c$\approx$ v_n, the mean velocity of the nucleon's Fermi motion in nuclei) projectiles in a heavy target nucleus.
4. photoproduction making use of the nuclear photoeffect - the method of choice at ELBE.

In all cases the average neutron energy is much smaller than the other forms of energy coming from the neutron radiator. One may thus judge the "efficiency" of a neutron source by the amount of energy needed (or waisted) for a free neutron.

For the 4 processes listed above one estimates:

1. In a fission reactor up to 2 neutrons per fission may be taken out; the fission fragments with their 200 MeV of kinetic energy thus deposit 1 Ws per $6 \cdot 10^{10}$ neutrons. The maximum power density of a fission reactor (500 W/cm^3) results in a flux limit of $5 \cdot 10^{12} n/cm^2 \cdot s$ for the emission from a reactor volume of $1 cm^3$.
2. In nuclear reactions usually considerably less than 10^9 neutrons are emitted per Ws of beam and they have narrow distributions in energy and direction, such that they are of use in special cases only.
3. One proton of 1.2 GeV hitting 35cm of Pb leads to 22 neutrons; this corresponds to 10^{11} neutrons per Ws of beam [1]. In 1 cm of Pb only $5 \cdot 10^9$ neutrons were observed per Ws of beam.
4. 30 MeV electrons deposit about half of their energy in 1 cm of Pb and the resulting bremsstrahlung leads to 10^{-2} free neutrons per electron [2]; thus $2 \cdot 10^9$ neutrons are produced per Ws of beam, and emitted from the radiators surface of 6 cm^2.

From these numbers it seems as if neutron production at an electron accelerator like ELBE is much less efficient than e.g. a spallation neutron source. But in many investigations not the neutron rate but rather the neutron flux (rate per area) is the important quantity ; as already obvious from what was noted under (3) the size of the spallation target determines the flux. If also the proton beam dimension is taken into account, the flux per power falls to $10^9 n/cm^2 \cdot Ws$ for a beam size 6x20 cm^2 as envisaged for the proposed European Spallation Source ESS. As compared to $3 \cdot 10^{12} n/cm^2 \cdot s$ to be reached at ELBE with 3.3 MHz repetition rate and thus 10 kW beam power, the ESS with its envisaged MW's of beam power may finally produce $10^{15} n/cm^2 \cdot s$; the ESS proposal [3] announces an average thermal flux of $3 \cdot 10^{14} n/cm^2 \cdot s$.

A high flux from a small radiator volume is especially important for time-of-flight studies yielding information about the energy dependence of neutron induced processes. For neutron energies above 100 keV and $\triangle E/E < 2$ % the ESS with its ejection bunch length of $\sim 1\mu$s has to use 200 m of flight path; this results in a flux of $10^7 n/cm^2 \cdot s$ at the end of the flight path.

ELBE with <200 ps pulse width and 3.6 m path length allows TOF-experiments up to 3MeV with $\triangle E/E \approx 1\%$ at several $10^6 n/cm^2 \cdot s$, and is thus fully competitive to ESS for such fast neutrons. To exploit this advantage in TOF-studies detectors with < 200 ps time resolution are required. With such detectors ELBE-n-TOF will allow energy dispersive neutron tomography and measurements of neutron scattering in materials of importance for the transmutation of nuclear waste as well as laboratory simulations for the astrophysical s-process. For neutrons of $\sim 0.1 MeV$ the parameters of ELBE allow for an improvement of up to one order of magnitude as compared to the electron linac ORELA at Oak Ridge (Tenn., USA), which is dedicated to such studies. As was shown there recently [4] energy dispersive neutron capture and transmission measurements have impact on our understanding of the "element-cooking" in stars.

One choice for neutron detectors of such good time resolution are small volume scintillators read out by photomultipliers. To compensate the small probability of signal generation (relying on proton recoil) a large total detection volume is required. Only by careful optimization of the detector geometry and the signal processing paths a cost-efficient set-up can be designed [5]; such work is in progress at the IKH.

[1] D. Hilscher for the Nessy Collaboration at FZJ-COSY, Heraeus Ferienkurs Dresden, 2002
[2] B. Naumann et al., Annual Report ELBE 2002 and ELBE/IKH 2001
[3] ESS proposal 2002
[4] P.E. Koehler et al., PRC 64(2001)065B02 and PRC62(2000)055803
[5] A. Butra et al., NIMA 455(2000) 412

Detector Setup for Nuclear-Resonance-Fluorescence Experiments at ELBE [D]

R. Schwengner, L. Käubler, M. Langer, G. Rusev, W. Schulze, A. Wagner

The bremsstrahlung facility at ELBE will be used for nuclear-structure experiments employing photon-induced reactions such as (γ,γ') (nuclear resonance fluorescence), (γ,n), (γ,p) (nuclear photoeffect) and photon-induced fission. All these experiments require an efficient setup of high-purity germanium (HPGe) detectors for the measurement of the characteristic γ radiation of the nuclides to be studied.

The setup of HPGe detectors for nuclear-resonance-fluorescence experiments is shown in Fig. 1. Four HPGe detectors are placed at 90° relative to the photon-beam direction and at 90° to each other. This orientation of the detectors was designed in particular for measuring asymmetries of γ-ray intensities in experiments with polarised photons. The detectors are mounted on frames made of sectional aluminium and can be moved on slide rails in order to vary the distance from the target. Each of these four detectors has an efficiency of 100 % relative to a 3" × 3" NaI detector. Two detectors (top and bottom) are four-fold segmented and may also be used as Compton polarimeters.

All four detectors are surrounded by escape-suppression shields consisting of eight optically separated bismuth germanate (BGO) scintillation detectors. These BGO detectors were specially designed for the present setup which is illustrated in Fig. 2. An example for the performance of the escape-suppression shield is shown in Fig. 3. This example for the energy region around 8 MeV shows that the Compton background in the HPGe detector is reduced by a factor of about two while the single-escape peak is reduced by a factor of about three in the spectrum measured in anticoincidence with the BGO detector as compared with a singles spectrum.

A fifth HPGe detector is positioned at 130° with respect to the beam direction in order to enable the measurement of angular distributions of the γ rays.

Fig. 1 *Setup of high-purity Ge detectors surrounded by escape-suppression shields. The photon beam enters the experimental area from the right.*

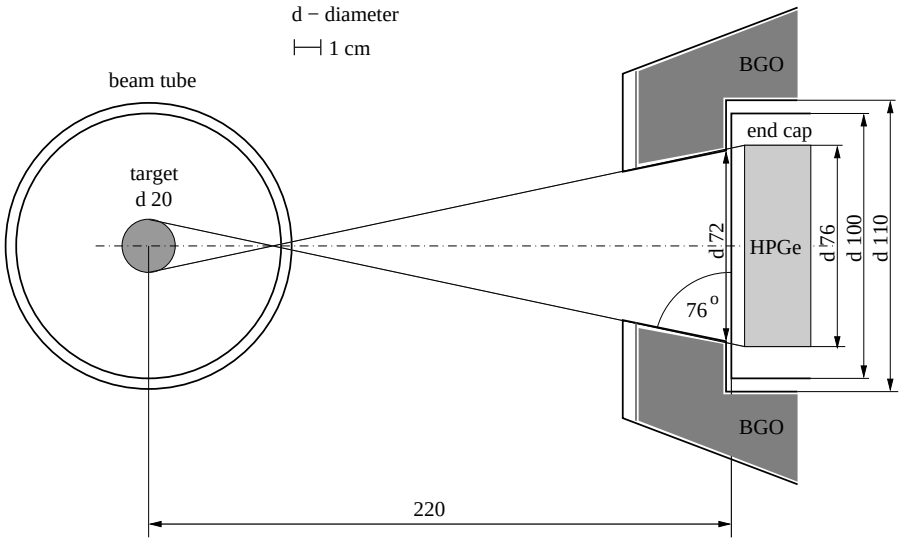

Fig. 2 *Shape of the BGO detector surrounding the end cap of the HPGe detector. The front end of the BGO detector was designed such that radiation from a target of 20 mm diameter is covered by the HPGe detector at a distance of 220 mm from the target.*

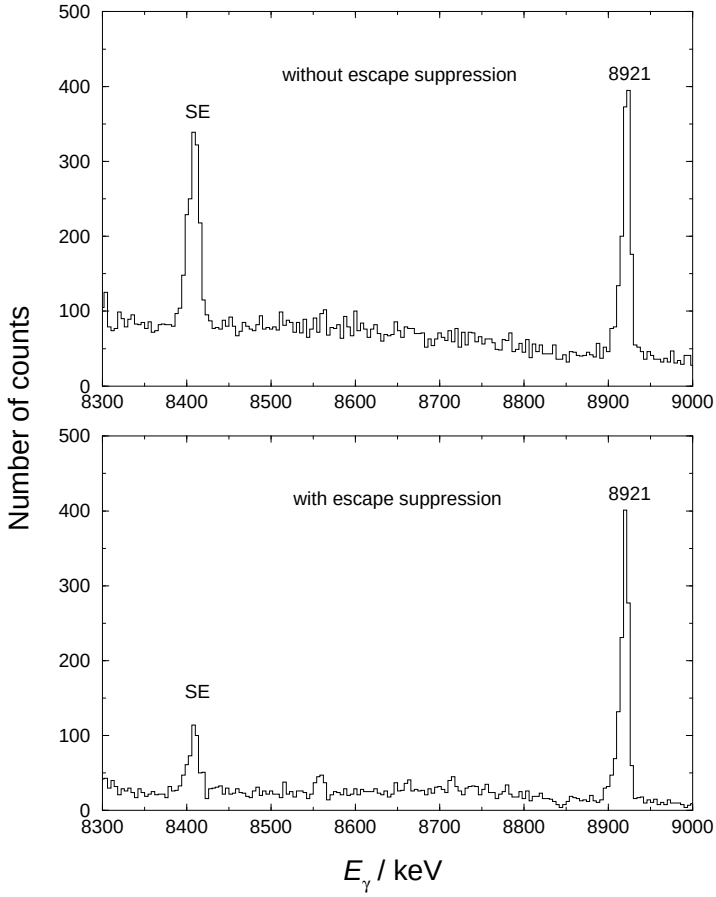

Fig. 3 *Portions of spectra of one HPGe detector containing singles events (upper panel) and events measured in anticoincidence with the surrounding BGO detector (lower panel). Peaks labelled SE are the single-escape peaks belonging to the full-energy peak at 8921 keV.*

Collimators for the BGO Escape-Suppression Shields [D]

G. Rusev[1], R. Schwengner, A. Wagner, L. Käubler, F. Dönau, E. Grosse

In nuclear spectroscopy high-purity germanium (HPGe) detectors are used for γ-ray detection with high energy resolution. However, these detectors have a rather small detection efficiency at high γ-ray energies. In order to suppress the signals of not fully absorbed photons in the HPGe crystal we use an escape-suppression shield of bismuth germanate (BGO) scintillation detectors [1]. The BGO surrounds the HPGe detector and works as a veto to photons scattered out of the HPGe crystal.

The escape-suppression shield has to be protected from direct radiation from the nuclear-resonance-fluorescence (NRF) target. We designed a lead collimator by performing Monte-Carlo simulations with the GEANT3 [2] program package, where the real detector-setup geometry was implemented. Monoenergetic photons with energies of 7, 10, 13 and 16 MeV were generated from the place of the NRF target. These energies represent the range where we expect to observe resonance lines. The entrance and exit diameters of the collimator were varied from 24 to 32 mm and from 26 to 72 mm, respectively, in steps of 1 mm. For each collimator geometry a spectrum of the deposited energy in the HPGe crystal in anticoincidence with the BGO escape-suppression shield was collected. From the spectrum the area of the photo-peaks and the common background due to Compton scattering and pair creation was extracted.

We used two competing criteria to obtain the optimal geometry of the collimator. The first criterion is to maximise the ratio of photo-peak to background. Fig. 1 shows this ratio versus the entrance and exit diameters of the collimator cone. It shows a flat distribution with a maximum at smaller diameters. The second criterion is to get a big photo-peak area. Fig. 2 shows the photo-peak area versus the two collimator diameters. This quantity increases with increasing opening angle of the collimator.

One good compromise is a point in the flat part of ratio peak-to-background for which the photo-peak area is as big as possible. We chose values for the entrance and exit diameters of 30 and 50 mm, respectively. The point is marked with a cross in Figs. 1 and 2.

Lead was chosen as a material for the collimator because it has a big density and well known NRF lines. The collimator thickness is 70 mm. This is equivalent to about five half-thicknesses for the absorption of 3 MeV photons. The collimator length was divided into one part of 3 cm and four parts of 1 cm in order to adjust experimentally the collimator thickness. The technical outline is shown in Fig. 3.

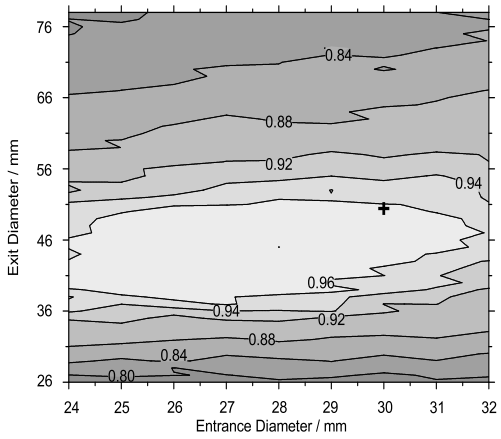

Fig. 1 *Normalised ratio of photo-peak to background versus the entrance (abscissa) and the exit diameter (ordinate). The cross marks the chosen diameters.*

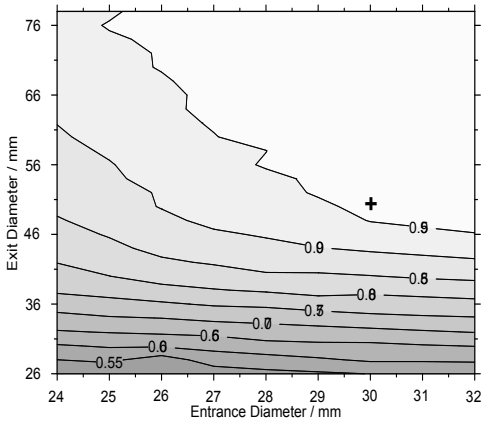

Fig. 2 *Normalised area of photo-peak versus the two diameters. The cross shows the chosen diameters.*

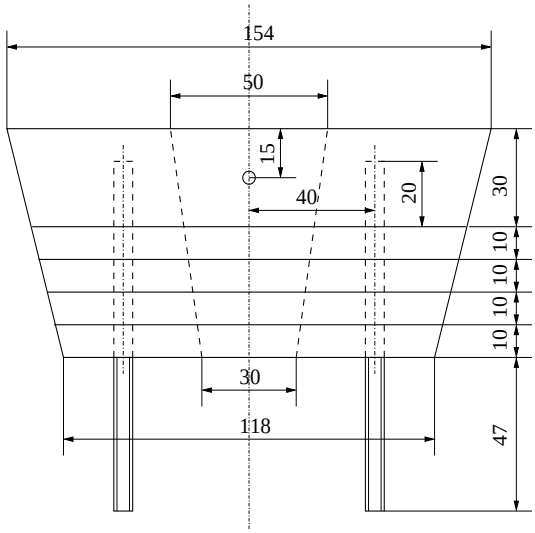

Fig. 3 *Technical outline of the collimator.*

[1] R. Schwengner et al., This Report, p. 27

[2] CERN Program Library Long Writeup Q121, CERN, Geneva (CH), 1994

[1] *FZR and INRNE, Sofia, Bulgaria*

Radiator for the Production of Bremsstrahlung at ELBE

K.D. Schilling, F. Dönau, E. Grosse, L. Käubler, R. Schwengner, A. Wagner, B. Wustmann[1], U. Lehnert[2], A. Nowak[1], B. Rimarzig, R. Schlenk[1]

The radiator occupies a key position in the nuclear physics beam line at ELBE, in particular, for the nuclear resonance fluorescence (NRF) experiments [1]. It converts the kinetic energy of the electrons into electromagnetic radiation, more precisely, into bremsstrahlung. The radiator itself consists of a thin metallic foil (e.g. Nb or Al) or of a thin slice of other material (e.g. CVD diamond) and is embedded in a water-cooled holder construction as shown in Fig. 1.

The radiator foil (slice) is hit by the electron beam and absorbs typically only about one part per thousand of the incident electron energy. The radiator thickness has to be optimized for each material by making a compromise: to maximize the production yield of bremsstrahlung, on the one hand, and to minimize the small-angle scattering of the electrons during their passage through the radiator material, on the other hand. The latter effect has two important consequences: (i) a definite polarization degree of the bremsstrahlung beam can be achieved, which is important for parity determinations of high-energy excited states to be measured, and (ii) the radiation background resulting from the interaction of the scattered electrons in the beam envelope with beam-line components downstream of the radiator can be reduced. Thus, the use of thin radiators has been decided in the present case. The typical thickness ranges from $3\text{x}10^{-4}$ to 10^{-3} times the radiation length X_0, that means , for instance, 4 to 12 μm Nb, 25 to 75 μm Al and 70 to 180 μm diamond radiators.

Some preparatory considerations and simulations regarding the choice of optimum radiator materials have been performed earlier [2]. They result in the preference of the above mentioned Nb and Al radiators for reasons given here and in [2]. Diamond is another candidate with superior heat conductivity, heat resistivity as well as neutron separation energy (cf. also [3]). The diameter of the radiator foils (slices) was chosen primarily with regard to the best possible heat dissipation; but possible instabilities of the beam alignment were also taken into account.

The beam position on the radiator is continuously observed by a video camera in the following way: a mirror positioned about 600 mm in front of the radiator inside the beam tube but outside of the electron beam reflects the optical transition radiation (OTR) of the beam spot emitted backwards into the video camera, thus imaging the radiator and the beam spot completely.

Furthermore, the temperature of the radiator at the beam spot (Ø $\approx$ 2 mm) is controlled by radiation thermometry. For this purpose, a pyrometer (RAYTEK Corporation, Santa Cruz, CA) with a laser viewfinder and a high optical resolution (300:1) is monitoring the infrared radiation (of 1.6 μm wavelength) emitted from the hottest spot of the radiator in a distance of 300 mm at the backward angle of 135°. Thus, we are able to determine the maximum temperature in the centre of the radiator with about 1 mm spatial resolution. This is an important information to prevent melting of materials like aluminium. The range of the expected critical temperatures has been calculated in advance with the finite-element code ANSYS [4] for various materials. This was of decisive importance for the design and construction of the radiator holder (Fig. 1).

After having passed the radiator, the geometrically widened (spread) electron beam is deflected by a dipole magnet [5] and led through a vacuum separation window made from beryllium (1 mm thick, Ø = 90 mm) into the electron beam dump, where far the most of the beam power is deposited (cf. Fig. 1 in [6]).

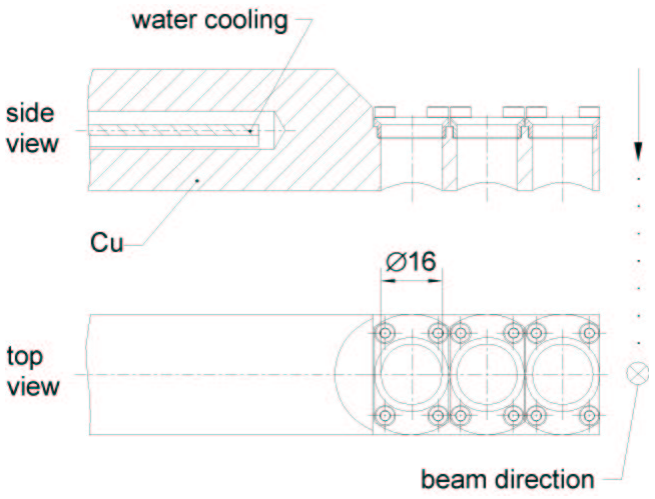

Fig. 1 *Schematic view of the radiator holder consisting of a massive, water-cooled Cu rod with three fixings for the radiator foils at the top (on the right). The net diameter of the radiators is 16 mm. The beam direction is indicated.*

[1] K.D. Schilling et al., Wiss.-Tech. Ber. FZR-271 (1999) 32; K.D. Schilling, http://www.fz-rossendorf.de /ELBE/en/np; R. Schwengner, http://www.fz-rossendorf.de /FWK/MITARB/rs/krf-elbe.html

[2] A. Wagner et al., Wiss.-Tech. Ber. FZR-271 (1999) 33

[3] A. Wagner et al., Wiss.-Tech. Ber. FZR-319 (2001) 40

[4] M. Werner, FZ Rossendorf, FWS, priv. comm.

[5] K.D. Schilling et al., This Report, p. 33

[6] K.D. Schilling et al., This Report, p. 31

[1] *FZ Rossendorf, FWF*
[2] *FZ Rossendorf, FWL*

Steering Magnets for the Production of Polarized Bremsstrahlung at ELBE

K.D. Schilling, U. Lehnert[1], F. Herbrand[2], R. Schwengner, A. Wagner, B. Caspar[2], M. Langer, T. Riedel[2], A. Wagner II

The electron beam is transported by a non-dispersive system of two dipole and three quadrupole magnets into the nuclear physics beamline and focused onto the radiator [1] as schematically displayed in Fig. 1. The collimated beam of bremsstrahlung photons excites the target nuclei to be investigated in the nuclear resonance fluorescence (NRF) experiments. The de-excitation of the excited states occurs via the emission of characteristic γ-rays, which are the subject of investigation [2].

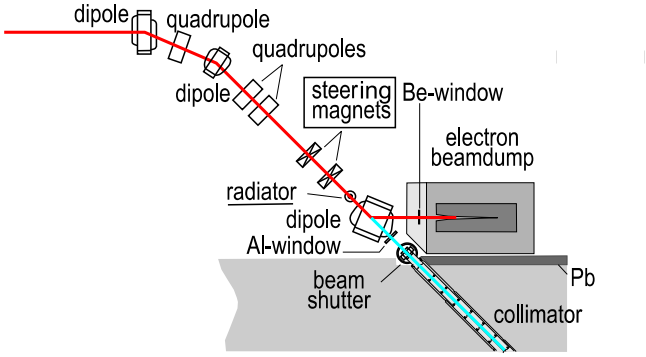

Fig. 1 *Nuclear physics beam line for the production of polarized bremsstrahlung at ELBE (red = electron beam, blue = bremsstrahlung beam).*

In order to deduce the parity of the excited states, it is necessary to measure the linear polarization of the $\gamma-$transitions. The knowledge of the polarization enables a discrimination between electric and magnetic multipole radiation, especially between electric dipole (E1) and magnetic dipole (M1) transitions. For this purpose, the target will be irradiated with polarized bremsstrahlung. The method for polarized bremsstrahlung production is shown in Fig. 2. It makes use of the fact [3] that the electric field vector $\vec{E}$ of the radiation is aligned tangentially around a cross section of the spatial distribution of the photons. With two steering magnets described below, the electron beam will be deflected from the normal direction and back such that it hits the radiator in the centre under a particular angle Θ_o. As a consequence, an off-axis portion of the spatial distribution of the photons is cut out by the collimator. This off-axis portion of the bremsstrahlung cone is dominated by a definite direction of the electric field vector $\vec{E}$, which means that the photon beam passing through the collimator is partially polarized. The degree of polarization depends on the angle Θ_o and has a maximum at $\Theta_o = m_0 \cdot c^2 \ / \ E$, wh ere $m_0 \cdot c^2 = 511$ keV is the rest energy of the electron and E is the total energy of the incident electrons. The polarized incident photons cause an azimuthal asymmetry of the intensity of the γ-transitions emitted from the excited states of the target nuclei. The asymmetry of E1 radiation is opposite to the one of M1 radiation. Therefore, one can discriminate between electric and magnetic radiation by measuring the asymmetry with detectors at different azimuthal angles (see Fig. 2).

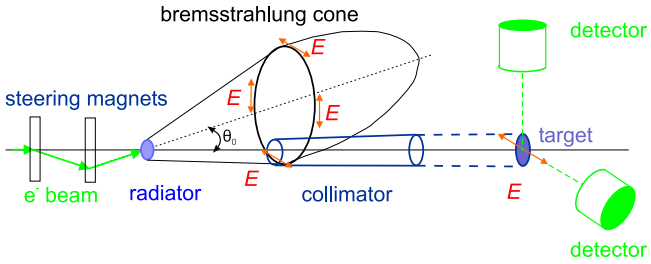

Fig. 2 *Principle of generation of linearly-polarized off-axis bremsstrahlung.*

The two steering magnets of identical construction are positioned 340 mm and 680 mm in front of the radiator, respectively (cf. Fig. 1). They were built up symmetrically (see Fig. 3) to deflect the electron beam periodically into the four directions in space: left(l) and right(r), up(u) and down(d). Thus - in spite of possible fluctuations of the electron current - the effective photon flux for each deflection angle will be the same. In this way, possible systematic asymmetries in the steerer positions and in the beam alignment will be averaged resp. minimized. The monitoring of the photon flux and the determination of its energy distribution is performed with the setup described in [4]. A sketch of one of the two steering magnets is presented in Fig. 3. The four identical coils are symmetrically arranged at the steel (ST37) yoke around the beam tube of 70 mm outer diameter (66 mm inside diameter). The shape of the four pole shoes has been optimized for the best field homogeneity [5]. The magnetic field strength in the middle plane of the steerer on the symmetry axis reaches about 30 mT - whereas 25 mT (83 %) are achieved on a trajectory displaced by 22 mm perpendicularly to the field lines, which corresponds to the maximum required displacement (deflection) of the electron beam.
In order to achieve the highest degree of polarization, the typical deflection angles range from about 3.5° to 1.5° for electron energies from 8 to 20 MeV. The deflection angles of the electron beam are visually optimized before and controlled after each measurement by two view screens at definite positions using the diagnostic mode of the accelerator, i.e. at low beam currents. The first view screen is positioned downstream of the second

[1] *FZ Rossendorf, FWL*
[2] *FZ Rossendorf, FWF*

steering magnet 210 mm in front of the radiator, where the beam is relatively far displaced from the beam axis; the second view screen is at radiator position, where the beam crosses the centre of the radiator.
Continuous monitoring of the polarization degree of the bremsstrahlung beam is required during the experiment. This is realized by the polarization monitor presented in [6]. The switching signal for the steerer coils is also delivered from the polarization monitor such that the electron beam is deflected after a definite number of events into the next of the four directions in space in the order: l - u - r - d. Self-made 15V/5A linear regulation moduls are used to supply the steering coils. The polarization degree and the coil currents are controlled by a progammable logic controller (PLC) SIMATIC S7 for each coil separately. This PLC is embedded in the ELBE machine control system. The sets of current for each deflection angle can be stored and reloaded by the human-machine interface (HMI) WinCC of the ELBE machine control system.

The effective length L_{eff} of the magnetic field in beam direction - as a characteristic property of the steering magnet - has been deduced by a Hall-probe measurement to be 186 mm. The product of the latter quantity with the required magnetic field strength in the middle plane determines the deflection angles.
A third steering magnet is placed between the radiator and the dipole (deflecting) magnet (cf. Fig. 1) in order to correct the vertical component of the tilted beam direction. The horizontal beam component can be corrected by an additional contribution to the magnetic field value of the deflecting dipole magnet. This steering magnet has the shape of a C-magnet with horizontal field direction produced by four coils that are arranged in the following way: each one of them at the two vertical legs and two at the horizontal leg of the yoke. Thus, magnetic fields of more than 20 mT can easily be achieved. The effective field length of the third steering magnet has been measured to be $L_{eff} = 133$ mm.

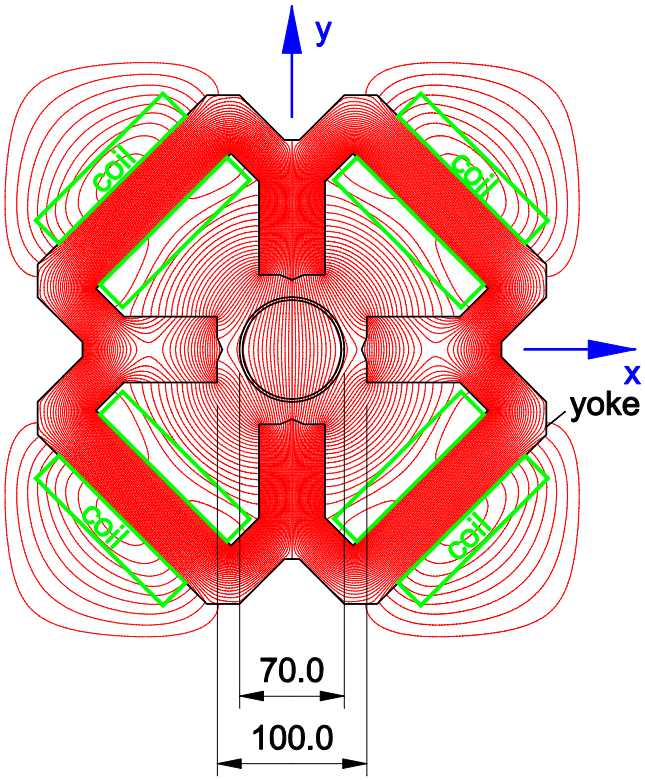

Fig. 3 *Sectional drawing of a steering magnet with the magnetic field pattern calculated with the code POISSON [5]. The cross-section of the beam tube is indicated in the centre. Sizes are in mm.*

[1] K.D. Schilling et al., This Report, p. 30
[2] R. Schwengner, http://www.fz-rossendorf.de/FWK/MITARB/rs/krf-elbe.html
[3] M. May and G.C. Wick, Phys. Rev. 81 (1951) 628
[4] A. Wagner et al., FZ Rossendorf, Wiss.-Tech. Ber. FZR-341 (2002) 38
[5] J.H. Billen and L.M. Young, Poisson Superfish, version 6, LAACG, LANL, NM (2000)
[6] R. Schwengner et al., FZ Rossendorf, Wiss.-Tech. Ber. FZR-341 (2002) 39

Beam Separation Magnet of the Bremsstrahlung Facility at ELBE

K.D. Schilling, M. Langer, U. Lehnert[1], W. Schulze

The electron beam impinging upon the radiator [1] of the nuclear physics beam line generates bremsstrahlung for NRF and photofission experiments [2]. Shortly after having passed the radiator, the electrons are deflected by a large dipole magnet to be described here into the electron beam dump, whereas the bremsstrahlung photon beam goes straight ahead through the collimator [3] to the nuclear physics cave. The dipole magnet, thus, separates the electron beam from the photon beam (cf. also Fig. 1 in [4]). The magnet was delivered originally as a standard dipole magnet (DANFYSIK A/S) with a 40 mm gap.

This gap has been enlarged to 117 mm in order to meet the requirements discussed in [1], i.e. to enable the beam, which is widened by small-angle scattering after having passed through the radiator foil, the passage through the vacuum chamber of the magnet with minimum interaction with the chamber walls. After this change of the construction, a series of detailed magnetic field measurements with a Hall probe have been performed and compared with model calculations with the POISSON code [5].

Two important results have been obtained: (i) the magnetic field distribution has been measured including the maximum field value of $B_{max} = 363$ mT (at $I_{max} = 160$ A) in the centre of the pole shoes and (ii) the effective field length L_{eff} has been derived to be 309 mm. The calculated value [5] of B_{max} is 373 mT in good agreement with the experimental result. The calculated L_{eff} value [5] is with 281 mm somewhat smaller (≈ 10 %) than the result derived from the measured field distribution. This slight difference is within the usual model uncertainties for a dipole magnet with such a large ratio of gap/pole-shoe length.

On the basis of the measured L_{eff} value, the functional dependence of the magnetic field strength - and, in this way, of the electron beam energy - on the coil current has been deduced, which serves now as a basis for the determination of the electron beam energy at the nuclear physics beam line. The analytical expression is:

$$E_{kin}(MeV) = 0.267 \cdot I(A) - 0.402.$$

The graphic representation of this dependence is shown in Fig. 1. It can also be seen here that there are reserves in the applicability of the magnet for even higher beam energies - if desired in future.

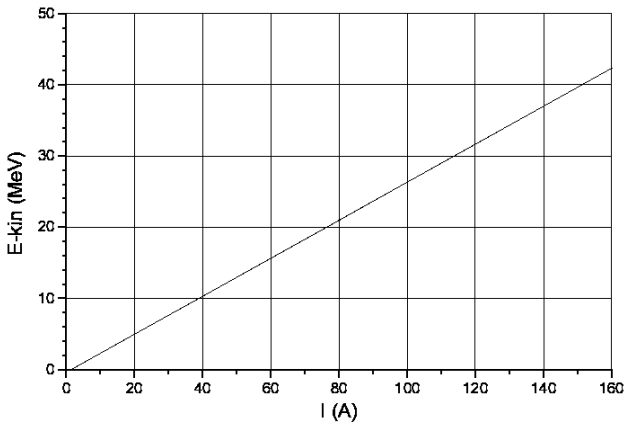

Fig. 1 *Electron beam energy vs. coil current for the 45° deflecting dipole magnet of the bremsstrahlung facility.*

[1] K.D. Schilling et al., This Report, p. 30
[2] R. Schwengner, http://www.fz-rossendorf.de/FWK/MITARB/rs/krf-elbe.html
[3] K.D. Schilling et al., FZ Rossendorf, Wiss.-Tech. Ber. FZR-341 (2002) 37
[4] K.D. Schilling et al., This Report, p. 30
[5] J.H. Billen and L.M. Young, Poisson Superfish, version 6, LAACG, LANL, NM

[1] *FZ Rossendorf, FWL*

Dipole Excitations in ^{98}Mo [B]

G. Rusev[1], R. Schwengner, F. Dönau, L. Käubler, S. Mallion, K. D. Schilling, A. Wagner, L. K. Kostov[1], H. von Garrel[2], U. Kneissl[2], C. Kohstall[2], M. Kreutz[2], H. H. Pitz[2], M. Scheck[2], F. Stedile[2], P. von Brentano[3], J. Jolie[3], A. Linnemann[3], N. Pietralla[3], V. Werner[3]

The chain of stable Mo isotopes is an interesting object for the investigation of the interaction between protons and neutrons. In ^{94}Mo, 1^+, 2^+ and 3^+ mixed-symmetry states were found which deexcite via $M1$ transitions with strengths of up to 0.3 μ_N^2 [1,2]. Possible candidates for such states were also found in ^{96}Mo [3]. In the next heavier isotope ^{98}Mo, the influence of the $N = 56$ subshell closure on the properties of dipole states may be studied. Nuclear resonance fluorescence (NRF) experiments were carried out at the Stuttgart Dynamitron accelerator at electron energies of 3.3 and 3.8 MeV. The target consisted of a sample of ^{98}Mo with a mass of 1998 mg and an enrichment of 98.55%, combined with 756.7 mg ^{27}Al and 102 mg ^{13}C for photon flux calibration.

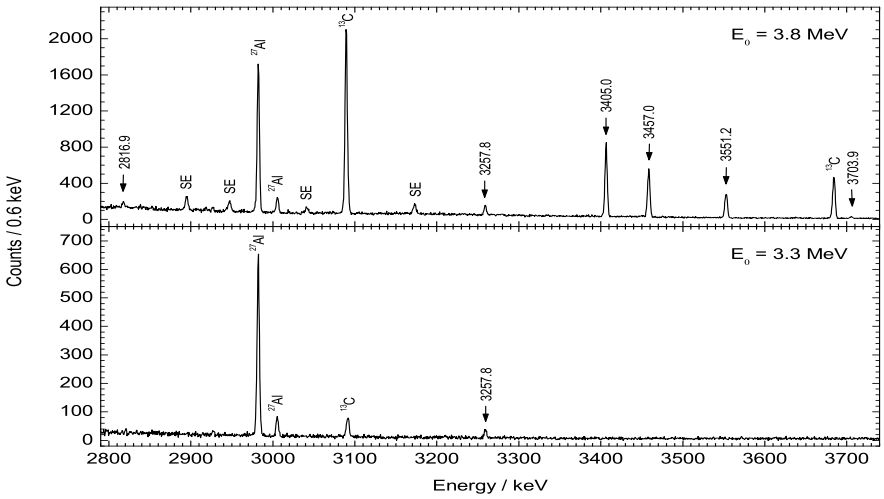

Fig. 1 *Parts of spectra of photons scattered from ^{98}Mo, measured at 127° relative to the beam and at electron energies of 3.8 MeV (top) and 3.3 MeV (bottom). SE marks the single-escape peaks.*

We observed six transitions in ^{98}Mo for the first time [4]. Spectra including these transitions are shown in Fig. 1. The angular distributions indicate dipole character for the newly observed transitions.

The comparison of the spectra measured at different energies reveals that the transition at 2817.1 keV is not a ground-state transition, but deexcites a state at an energy greater than 3.3 MeV. Indeed, it fits well the energy spacing between the dipole state at 3552.2 keV and the second 0^+ state.

A level scheme including the dipole states found in the present experiments and known low-lying states is shown in Fig. 2. The deexcitation of a $J = 1$ state to the excited 0^+ state is a specific feature of this nuclide and one of the first observations of such transitions from dipole states to intruder states.

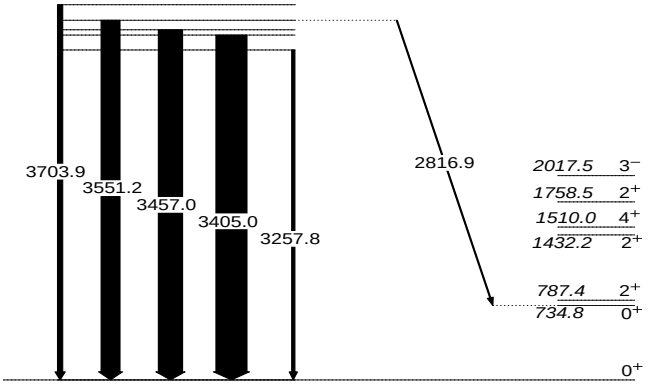

Fig. 2 *Level scheme of ^{98}Mo including the dipole states found in the present work (left) and known low-lying states (right).*

[1] N. Pietralla et al., Phys. Rev. Lett. 83 (1999) 1303
[2] N. Pietralla et al., Phys. Rev. Lett. 84 (2000) 3775
[3] V. Werner et al., IfS Annual Report 1999, p. 18
[4] G. Rusev et al., Fz Rossendorf, Wiss.-Tech. Ber. FZR-341 (2002) 77

[1] *FZR and INRNE, Sofia, Bulgaria*
[2] *IfS, Universität Stuttgart*
[3] *Institut für Kernphysik, Universität zu Köln*

Nuclear Resonance Fluorescence Experiments on ^{100}Mo [D]

G. Rusev[1], R. Schwengner, F. Dönau, L. Käubler, S. Mallion, K. D. Schilling, A. Wagner, L. K. Kostov[1], H. von Garrel[2], U. Kneissl[2], C. Kohstall[2], M. Kreutz[2], H. H. Pitz[2], M. Scheck[2], F. Stedile[2], P. von Brentano[3], J. Jolie[3], A. Linnemann[3], N. Pietralla[3], V. Werner[3]

In order to extend our study of dipole excitations in Mo isotopes to greater neutron numbers we investigated the nuclide ^{100}Mo. This isotope has 58 neutrons and may allow us to study the onset of collectivity and its influence on the properties of dipole excitations.

We performed nuclear resonance fluorescence experiments at the Stuttgart Dynamitron accelerator at electron energies of 3.2, 3.4 and 3.8 MeV. A sample of 1620 mg ^{100}Mo, enriched to 99.0 %, was used as a target in the NRF measurements. The target was combined with 758.4 mg ^{27}Al and 102 mg ^{13}C for photon flux calibration. In the present experiments, we observed 19 γ rays for the first time. These γ rays are marked with their energies in the spectra shown in Fig. 1. Based on the analysis of the angular distributions we consider them as dipole transitions.

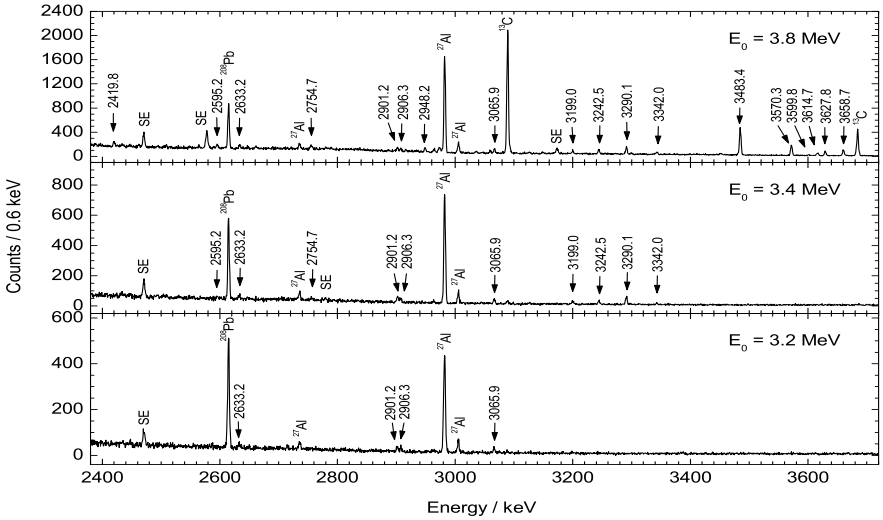

Fig. 1 *Comparison of partial spectra of photons scattered from ^{100}Mo at 127° relative to the beam axis for different electron energies. SE marks the single-escape peaks.*

The comparison of the spectra measured at the different energies allows us to distinguish between ground-state transitions and transitions that populate low-lying levels. Based on this comparison and on the respective level spacings we established the level scheme shown in Fig. 2. In addition to ground-state transitions, we observed transitions populating the lowest 2^+ state as well as excited 0^+ and 2^+ states. The observation of a transition to the excited 0^+ state is analogous to the neighbouring isotope ^{98}Mo [1]. The transititon at 2595.0 keV fits the energy spacing between the 3659.6 keV state and the 2^+_2 state as well as the spacing between the state at 3290.7 keV and the 0^+_2 state. The measurement at 3.4 MeV proves that both 2595.0 keV transitions exist and have nearly the same intensity.

In addition to the deexcitation of dipole states to the 0^+ intruder state, which was also found in ^{98}Mo, we observed transitions to low-lying 2^+ states in ^{100}Mo.

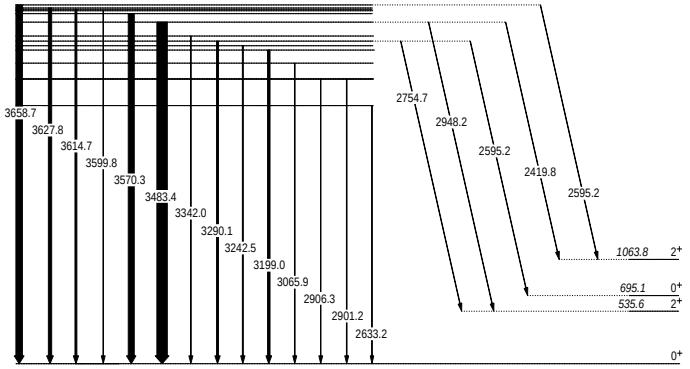

Fig. 2 *Level scheme of ^{100}Mo. The widths of the arrows are proportional to the intensities of the transitions.*

[1] G. Rusev et al., This Report p. 34

[1] *FZR and INRNE, Sofia, Bulgaria*
[2] *IfS, Universität Stuttgart*
[3] *Institut für Kernphysik, Universität zu Köln*

Simulations for a Double Time-of-Flight Spectrometer for Fission Fragments[G]

H. Sharma, A. Wagner, E. Grosse

The study of exotic nuclei is one of the most active and interesting areas of research in nuclear physics. Indeed, some of such studies have already opened a new area of research in nuclear physics. The nuclei with extreme neutron to proton ratio are very important in nuclear astrophysics because of their relevance to the r-process in nucleosynthesis. Informations on their structure and their properties would help us to better understand the r-process and also other violent stellar events. Experiments are planned to study these exotic nuclei at ELBE.

Theoretical calculations by Fan et al. [1] have shown the possibility of producing neutron-rich exotic nuclei at ELBE via bremsstrahlung-induced fission of ^{238}U. The next challenging task is to detect these low-energy fission fragments (FFs) with the highest attainable mass and charge resolution. The time-of-flight (TOF) measurements can be carried out with a high precision of the start signal due to the very good time structure ($<$ 10ps) of the electron beam at ELBE [2]. Using this precise timing of the electron beam for the identification of the fission fragments, the velocity change of the moving fragments can be measured by a double TOF method as shown in Fig. 1. The double TOF, i.e., first TOF (t1) of the fragments before passing the foil and the second TOF (t2) after passing them through the foil may provide a separation of mass and charge of the fission fragments. The technical information about the foils, MCPs, anodes, mirrors as illustrated in Fig. 1, will be given in a separate report.

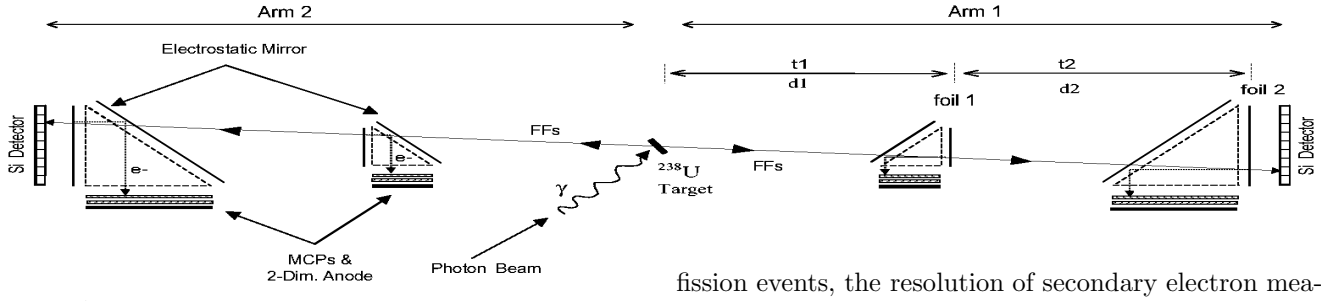

Fig. 1 *A schematic lay-out of the double TOF spectrometer.*

In the first elaborate attempt to understand the response of the double TOF spectrometer a simulation program based on a Monte Carlo method has been developed for an event-by-event analysis of the FFs. The calculated yield distribution is normalised to the experimental fragment yield distribution for a given fissioning nucleus. The fragment's kinetic energy is calculated using standard liquid drop parameters for the fissioning nucleus and the procedure reported in the literature [3]. The prompt neutron emission probability for the excited FFs is also calculated following the description given by Fraser [4]. At maximum two neutrons are evaporated from the excited fragment and the resulting velocity change of the fragment is taken into account. The fragment's kinetic energy-loss in the foil (foil1) is calculated and the energy straggling is estimated empirically as a function of fragment's Z and A and its energy. The input of the simulation program requires: (i) Fragment yield distribution; (ii) Liquid drop parameters; (iii) Neutron emission parameters for the fissioning nucleus; (iv) Composition of the foil and areal density; (v) Length of various flight paths.

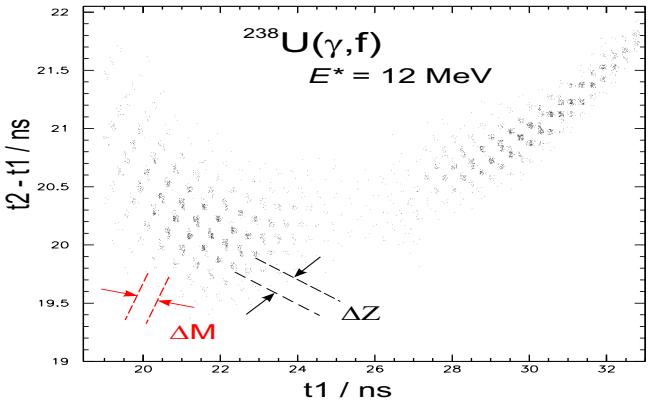

Fig. 2 *Calculated correlation between t1 and t2 for the double TOF spectrometer.*

Fig. 2 shows TOF spectra calculated for the ^{238}U(γ, f) reaction with an electron end-point energy of 12 MeV, distances $d1 = d2 = 300$mm and a carbon foil of $500\mu g/cm^2$. The results indicate that for the fragment's M and Z separation time resolutions better than $\Delta t1 = 100$ psec and $\Delta t2 = 300$ psec, respectively, are required. The multiple neutron evaporation, the ternary fission events, the resolution of secondary electron measurements, energy-loss of the FFs the target material, inhomogeneity in foil thickness and the energy-straggling in the foil will deteriorate the quality of the time spectrum and hence ΔM and ΔZ resolutions. These sources of deterioration in the precise M and Z determination of the FFs are subject of further investigations.

Present calculation has demonstrated that the simultaneous determination of mass and charge of the FFs can be possible by a double time-of-flight measurement at ELBE if the TOF measurement can be realised with a time resolution better than 100 ps.

[1] S. Fan, A. Wagner, E. Grosse, Wiss.-Tech. Ber. FZR-319 (2001) 39
[2] P. Evtushenko et al., Wiss.-Tech. Ber. FZR-341 (2002) 19
[3] The Nuclear Fission Process, Ed. C. Wagemans, CRC Press, 1991
[4] J. S. Fraser, Phys. Rev. 88 (1952) 536

A Time Coincidence Test Setup for an MCP Detector[G]

H. Sharma, K. Kosev, A. Wagner, K. D. Schilling, A. Wagner II, W. Schulze, K. Heidel

A double time-of-flight (TOF) spectrometer for the identification of fission fragments is under construction [1]. The TOF spectrometer will be tested offline with a spontaneous fission source ^{252}Cf. Secondary electrons emitted simultaneously with fragments from the ^{252}Cf source can be detected in order to get a trigger signal which is necessary as start signal for the TOF measurements with the source.

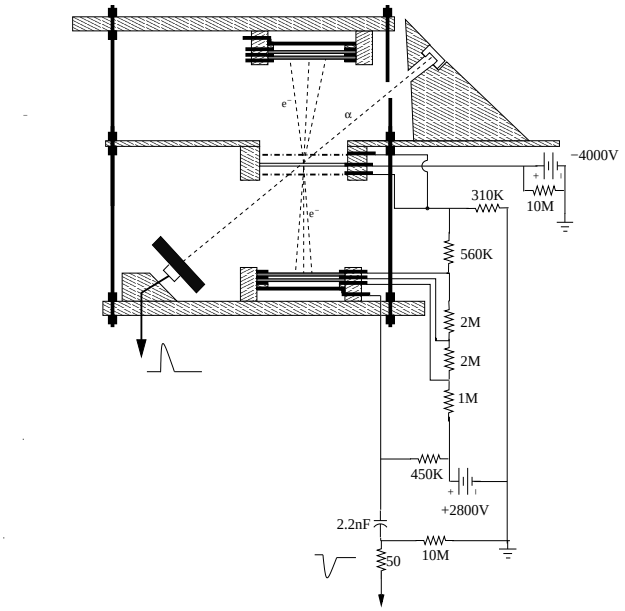

Fig. 1 *The provisional experimental setup.*

For this purpose a zero-time detector has been designed using two microchannel plates (MCPs) for amplification of the secondary electron signal. In order to test the performance of the MCPs, a coincidence measurement between the MCP and a silicon (Si) detector has been carried out by using a provisional experimental setup as shown in Fig. 1. We have also measured the coincidence between two MCP detectors by measuring backward and forward secondary electrons from the foil, as shown in Fig. 1

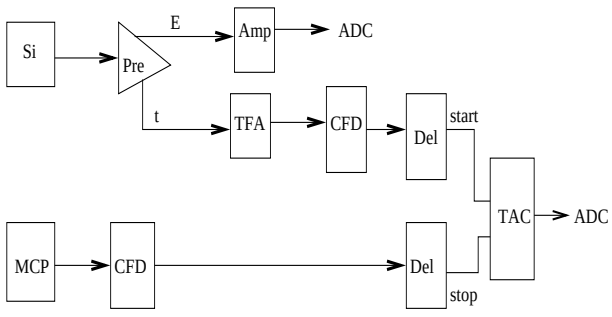

Fig. 2 *Block diagram of the slow-fast electronics setup used in the coincidence measurements.*

The measurements were performed with a collimated mixed radioactive alpha source (^{239}Pu, ^{241}Am and ^{244}Cm) in a vacuum chamber at a pressure of about $4\text{x}10^{-6}$ mbar.The alpha particles impinge on a thin aluminum foil (2.0μm thick) at an incidence angle of 45^o. The secondary electrons emitted from the foil were accelerated by -3.8 kV potential and collected onto the MCP. The foil and the Si and MCP detectors were mounted in very close geometry to the alpha source. The distance between alpha source and the Si-detector was about 80mm and the distance between foil and the MCPs was about 45mm. The accelerating grid was mounted below the foil at a separation of 3mm.

The anode, the MCPs and the accelerating grids were biased with a single positive bias supply by using a resistor chain. The foil was biased with a separate negative bias supply according to Fig. 1. The fast signals from the MCP were directly fed to constant-fraction-discriminator (CFD) whereas the signals from the Si-detector were processed through a charge-sensitive preamplifier. A standard fast-slow coincidence setup was used as shown in Fig. 2. In order to avoid any pickup in the Si detector from the high voltage discharges at the foil or from a discharge of the MCPs, both MCP and foil frames had metallized grounded surfaces.

The data were acquired using a multi-channel analyser. Fig. 3 shows the collected time-to-amplitude-convertor (TAC) spectra. In case of MCP versus Si detector a typical time resolution of 15 nsec was observed (Fig. 3) which mainly contributed by the the Si-detector. In case of coincidence between MCP versus MCP the time resolution of about 550 ps (FWHM) was obtained as shown in Fig. 3. Improvements to improve the time resolution are under way.

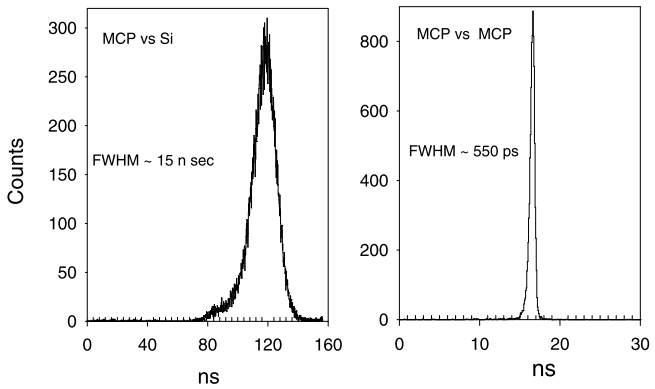

Fig. 3 *The TAC spectrum shows the observed time resolutions of 15 ns for MCP versus Si (left) and of about 550 ps for MCP versus MCP (right).*

[1] H. Sharma et al., This Report p. 36
[2] G. Pausch et al., Nucl. Instr. Meth. A 443 (2000) 304

Secondary Electron Trajectories for an Electrostatic Mirror[G]

H. Sharma, K. Kosev, A. Wagner, K. D. Schilling, M. Sobiella, K. Kanaki

Experimental studies of exotic neutron-rich nuclei are planned at ELBE. These nuclei will be produced via bremsstrahlung induced photo-fission. The fission fragments will be detected by a proposed double time-of-flight (TOF) method [1].
For this purpose a two-dimensional position-sensitive TOF spectrometer is under construction. The mounting system of the spectrometer is designed with coupling flanges of standard dimensions in order to use it at the heavy-ion syncrotron at GSI and at the electron accelerator ELBE. The spectrometer is composed of four TOF detectors [1]. Each of the TOF detectors consists of a thin foil producing secondary electrons, accelerating grids, an electrostatic mirror, a stack of micro-channel plates (MCPs) as a signal amplifier and a two-dimensional position-sensitive delay-line anode as shown in Fig. 1. The MCPs and delay-line anodes of active diameter of $\emptyset = 40$mm (DLD40) and $\emptyset = 80$mm (DLD80) have been procured from RoentDek[2].

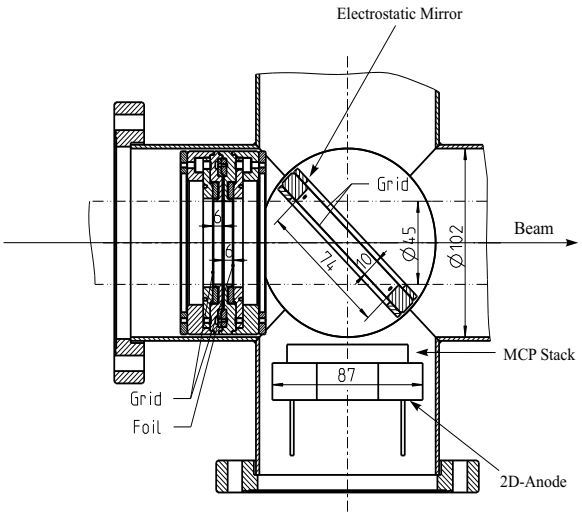

Fig. 1 *Setup for the position sensitive TOF detector with an active area of about 1250 mm^2.*

The electrostatic mirror, a decisive part of the TOF detector, has been designed and tested. The main function of the mirror is to deflect the secondary electrons (SEs) towards the MCP's surface isochronously. The mirror consists of two stainless-steel frames and two grids made of tungsten wires of $\emptyset = 31\mu$m with a separation of 0.5 mm. A ceramic [3] ring has been designed in order to keep the 10 mm separation between the two grids. The grids mounted with sufficient tension provide approximately 78 % transmission for the beam particles and can be biased up to 7500 V in high vacuum conditions.

Due to the large emittance and broad energy distribution of the SEs a proper acceleration and transport of these electrons is mandatory to obtain a good position and time resolution. Therefore, SEs trajectories have been calculated using OPERA-3D [4] in order to simulate the detector response and to optimize the setup accordingly.
A three-dimensional model space equivalent to the geometry of the TOF detector was defined as shown in Fig. 2. The distribution of the SEs emitted from the foils was considered isotropic [5]. The Maxwellian energy distribution of the SEs is also known from the literature [6]. Considering these two distributions the SEs trajectories were calculated.

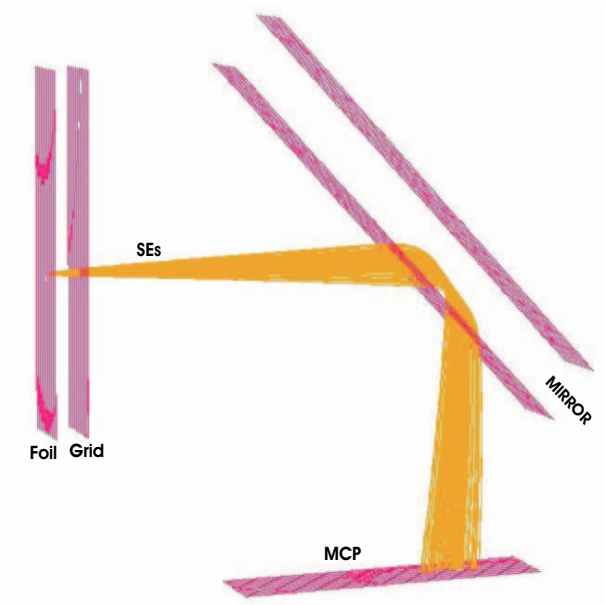

Fig. 2 *Model space equivalent to the TOF detector and corresponding secondary electrons trajectories.*

From these simulations the response of the mirror is found to be satisfactory and the necessary electrical potentials for the mirror and the foil have been optimised as : -4500V at the foil, and -5000V at the mirror and -500V at the grids. According to the present geometry of the TOF detector, the flight path for the SEs is about 120 mm. For this flight path the corresponding transversal spread in the SE-beam is determined as about 8 mm from these calculations. However, this is an upper limit of the lateral diffusion for the SEs.

[1] H. Sharma et al., This Report p. 36
[2] RoentDek GmbH: http://www.roentdek.com
[3] Vitronit©, http://www.vitron.de
[4] Vector Fields Ltd. Oxford OX51JE, England
[5] K. Kruglov, Nucl. Instr. Meth. A 441 (2000) 595
[6] B. L. Henke et al., J. Appl. Phys. 52 (1981) 1509

Measuring Foil Thicknesses for a Time-of-Flight Spectrometer[G]

K. Kosev, H. Sharma, A. Wagner

At ELBE, the high-intensity photon-beam from Bremsstrahlung-production will be used to produce exotic nuclei by photon-induced fission. For the detection of the fission fragments a double time-of-flight spectrometer is under construction. In this spectrometer several thin foils will be used. For secondary electron production a 4 micron thick polypropylene foil with an area of 46x70 mm^2 was metallised with 100 Å aluminium layer in order to reduce the electrical resistivity. The precise thickness profile of the foils is an important requirement for the TOF spectrometer [1].

In order to extract a precise thickness profile of the foil, energy-loss measurements have been carried out using a collimated mixed (^{239}Pu/^{241}Am/^{244}Cm) alpha source. To measure the thickness profile of the foil it was mounted on a frame in between the alpha source and a silicon detector inside a vacuum chamber set at about 6.7x10^{-6} mbar. The foil frame was moved along two dimensions with the help of two stepper motors remotely controlled. The position resolution for this setup was in the order of few a microns. For each run 24 measurements were taken with a step size of 2mm while keeping the other direction fixed.

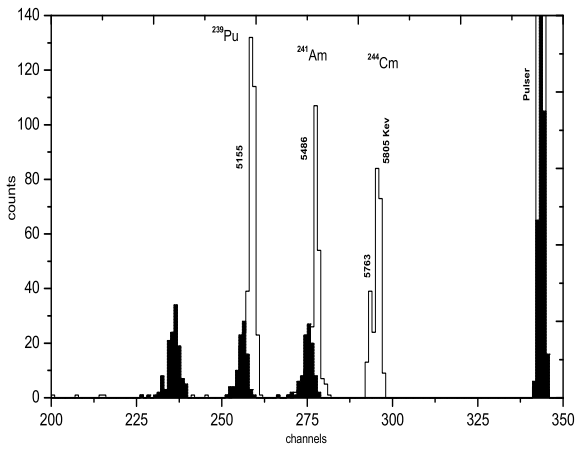

Fig. 1 *Comparison between a calibration spectrum (hollow peaks) and a spectrum with foil (full peaks).*

A spectroscopic electronics setup was used to determine the rest energy of the alpha particles after passing the foil. The silicon detector (type EURISYS LEC 200-4000) having sensitive areas of 200 mm (diameter 16 mm) and useful thickness of 4.25 to 4.88 mm was connected to a ZfK-VV5 preamplifier and an ORTEC 570 main amplifier set at a shaping time 0.5 μsec. The observed FWHM at 5486 keV for this detector was around 30 keV. For monitoring any gain shift in the electronics an ORTEC 440 research pulser was used. The data was acquired using Interwinner MCA. More than 1200 spectra were collected while scanning the whole area of the foil. Fig. 1 shows a comparison of spectra taken with and without the foil.

A dedicated program was developed for an automated analysis which locates the peaks and fits them with Gaussian distributions. From the peak's centroid the energy-loss of the alpha particles in the foils is determined and the thickness derived (see Fig 2).

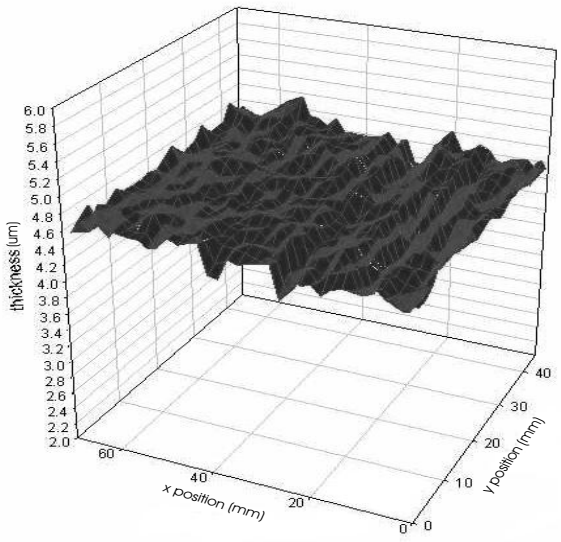

Fig. 2 *Two-dimensional distribution of the foil thickness profile using energy loss of alpha particles.*

The measurements show a satisfactory uniform thickness distribution of the foil as shown in Fig. 3.

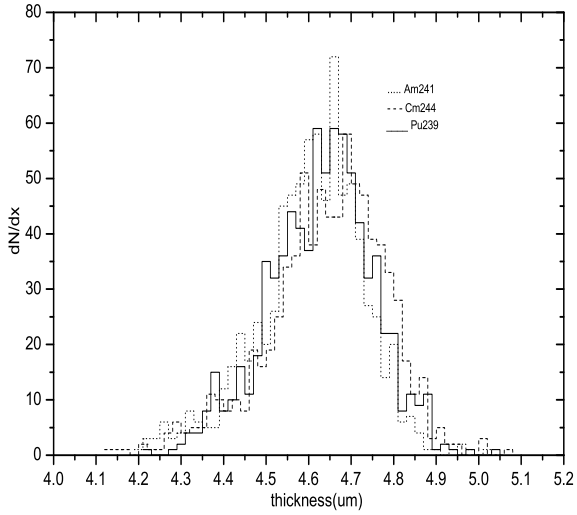

Fig. 3 *Thickness distribution of the foil.*

[1] H.Sharma et al., This Report, p. 36

Probing the Gateway to Superheavy Nuclei in Cranked Relativistic Hartree-Bogoliubov Theory

A. V. Afanasjev, S. Frauendorf, T. L. Khoo[1], I. Ahmad[2], G. A. Lalazissis[2]

The cranked relativistic Hartree-Bogoliubov (CRHB) theory [1], including approximate particle number projection through the Lipkin-Nogami method and the Gogny force in the particle-particle pairing channel, has been applied for a systematic study of the nuclei around ^{254}No [2]. These are the heaviest elements with a large body of spectroscopic data for testing the reliability of mean-field theory predictions for superheavy nuclei. The deformation, rotational response, pair correlations, quasiparticle spectra, nucleon separation energies and shell structure of these nuclei have been extensively studied with different RMF forces.

While the deformation properties are well reproduced, the calculations reveal that an accurate description of other observables requires better effective forces both in the particle-hole and particle-particle channels. The calculated moments of inertia show only small sensitivity to the RMF force and thus to the details of the single-particle structure. In contrast to previous studies, where the moments of inertia in lighter systems are well reproduced (see Ref. [2] for details), good agreement in the heaviest nuclei can be obtained only with a decrease ($\approx 12\%$) of the strength of the D1S Gogny force in the pairing channel.

The CRHB theory has been extended for a detailed description of quasi-particle states in odd and odd-odd nuclei. For the first time, the blocking procedure in such nuclei has been performed fully self-consistently, with effects of the breaking of time-reversal symmetry (nuclear magnetism) taken into account. Analysis of quasiparticle spectra in odd ^{249,251}Cf and ^{249}Bk nuclei with the NL1 and NL3 forces (see Fig. 1) suggests that the energies of most of the spherical orbitals, from which active deformed states of these nuclei emerge, are described with an accuracy better than 0.5 MeV. However, for a few subshells the discrepancies reach 1.0 MeV. Considering that the RMF forces were fitted only to bulk properties of spherical nuclei without considering single-particle energies, this level of agreement is impressive. However, in very heavy systems, where the level density is high, the accuracy is not sufficient for reliable predictions of the location of deformed shell gaps, which are small (≈ 1 MeV).

The results of the present investigation have a number of implications for the study of superheavy nuclei. The NL-SH and NL-RA1 forces do not provide satisfactory descriptions of the single-particle energies: the deviation between experiment and theory in the $A \sim 250$ mass region reach 2 MeV for some spherical subshells. Thus their application to superheavy nuclei is not recommended. The extrapolation of the results for quasiparticle states obtained in the $A \sim 250$ mass region suggest that the NL1, NL3 and NL-Z forces provide reasonable descriptions of most of the states in the vicinity of the $Z = 120$ and $N = 172$ spherical shell gaps. These are magic gaps in most parametrizations of the RMF theory. However, it is not possible to estimate the accuracy of the description of some low-j states, such as $\nu 3d_{3/2}$, $\nu 4s_{1/2}$ and $\pi 3p_{3/2}$, $\pi 3p_{1/2}$, which are located near these gaps by studying lighter deformed nuclei. Thus the particle numbers corresponding to magic gaps in superheavy nuclei still remain an open question. In addition, the study of number of effects in superheavy nuclei, such as pairing and the importance of self-consistency, is in progress.

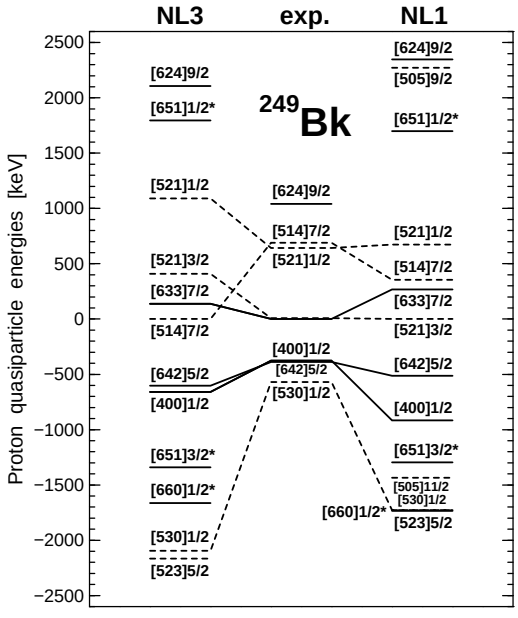

Fig. 1 *Experimental and theoretical quasiparticle energies of neutron states in ^{249}Bk. Positive and negative energies are used for particle and hole states, respectively. Solid and dashed lines are used for positive and negative parity states, respectively. The symbols 'NL3' and 'NL1' indicate the RMF force used in calculations.*

[1] A. V. Afanasjev, P. Ring and J. Konig, Nucl. Phys. A 676 (2000) 196

[2] A. V. Afanasjev, T. L. Khoo, S. Frauendorf et al., Phys. Rev. C 67 (2003) 024309; Proc. Conf. on "Frontiers of Nuclear Structure", Berkeley, USA, AIP Conf. Proc. 656 (2003) 379

[1] *Argonne National Laboratory, USA*
[2] *Aristotle University, Thessaloniki, Greece*

Proton-Neutron Pairing in Rotating $N \approx Z$ Nuclei

A. V. Afanasjev[1], S. Frauendorf

The rotational features of the $N \approx Z$, $A \sim 60 - 80$ nuclei were studied in a systematic way within the cranked relativistic mean field (CRMF) theory, cranked relativistic Hartree-Bogoliubov theory with only like-particle T=1 pairing, and cranked Nilsson-Strutinsky (CNS) approach. These nuclei are expected to provide important information on the nature (i.e. isoscalar T=0 or/and isovector T=1) and strength of proton-neutron (pn) pairing correlations [1]. The structure of ^{70}Br [2], ^{72,73}Kr [3, 4, 5] and ^{74}Rb [6] nuclei has been investigated in detail.

The Coriolis antipairing (CAP) effect breaks the $T = 1$ pairs, but there is no CAP effect for the $T = 0$ pairs [8] in which the n and p occupy identical space-spin orbitals. Thus isoscalar np pairing is expected to survive up to very high rotational frequencies and may influence the moments of inertia at these frequencies. However, the good agreement between calculations with and without pairing and experiment at high rotational frequencies (see Fig. 1 and discussion in a forthcoming article [9]) clearly shows that both types of pairing (like-particle and unlike-particle) are weak at these frequencies and have little impact on rotational properties of the $N \approx Z$ nuclei. This strongly suggests that high spin rotational structures do not provide evidence for possible existence of isoscalar np pairing.

It was also suggested that the presence of the isoscalar pn pairing leads to the delayed band crossing in the $N = Z$ nuclei as compared with its $N \neq Z$ neighbors. The bands in ^{72}Kr and ^{60}Zn were in focus of such discussions. Early data [7] shown by open circles in Fig. 1b indicated considerable delay of band crossing in ^{72}Kr. However, recent experiment [4, 5] revealed a previously unobserved side band shown by solid circles in Fig. 1b. This band, which is yrast above $I = 16\hbar$, represents missing doubly aligned S-band. The properties of this band above band crossing are excellently described both in the CRMF and CRHB+LN calculations. The CRHB+LN theory reproduces the band crossing frequencies in ^{74}Kr (see Fig. 1c) and suggest the lowering of crossing frequency in ^{72}Kr by $\approx$ 100 keV as compared with ^{74}Kr. Unfortunately, due to some uncertainties in the lowest few transitions of new band the frequency of paired band crossing in ^{72}Kr is not firmly established. However, the new data remove the largest part of discrepancies seen before between theory and experiment. These results for ^{72}Kr combined with the ones for ^{60}Zn (see Fig. 1a and Ref. []) considerably weaken the arguments in favor of delayed band crossing as a fingerprint of isoscalar pn pairing. On the contrary, the spectra of ^{74}Rb compared with the CRHB+LN calculations corrected for the $t = 1$ np-pair field by restoring isospin symmetry [1] give strong evidence for the existence of the isovector np pairing [6].

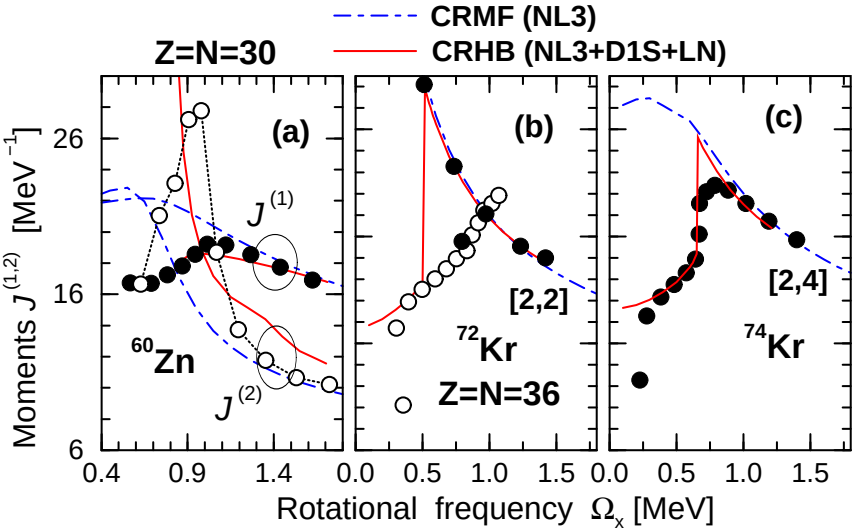

Fig. 1 *Panels (b-c) Experimental (circles) and calculated (lines) kinematic moments of inertia in ^{72,74}Kr nuclei. The results of the paired CRHB+LN and unpaired CRMF calculations are shown. The unpaired configurations are labeled by [p,n] where p(n) is a number of occupied $g_{9/2}$ proton (neutron) orbitals. Panel (a) shows the experimental and calculated kinematic and dynamic moments of inertia of magic SD band in ^{60}Zn.*

[1] S. G. Frauendorf and J. A. Sheikh, Nucl. Phys. A645 (1999) 509
[2] D. G. Jenkins et al., Phys. Rev. C 65 (2002) 064307
[3] N. S. Kelsall et al., Phys. Rev. C 65 (2002) 044331
[4] N. S. Kelsall et al., Proc. Conf. on ´´Frontiers of Nuclear Structure´´, Berkeley, USA, AIP Conf. Proc. 656 (2003) 261
[5] N. S. Kelsall et al., EuroPhysical Journal A, in press
[6] C. D. O'Leary et al., Phys. Rev. C 67 (2003) 021301(R)
[7] S. M. Fischer et al, Phys. Rev. Lett. 87 (2001) 132501
[8] A. L. Goodman, Phys. Rev. C 63 (2001) 044325
[9] A. V. Afanasjev and S. Frauendorf, in preparation

[1] *University of Notre-Dame*

Beta-Decay Studies of Neutron-Deficient Tin Isotopes [G]

M. Karny[1], Z. Janas[1], L. Batist[2], J. Döring[3], I. Mukha[3], C. Plettner[3], A. Banu[3], A. Blazhev[3], F. Becker[3], W. Brüchle[3], T. Faestermann[4], M. Górska[3], H. Grawe[3], A. Jungclaus[5], M. Kavatsyuk[3], O. Kavatsyuk[3], R. Kirchner[3], M. La Commara[6], S. Mandal[3], C. Mazzocchi[3], A. Płochocki[1], E. Roeckl[3], M. Romoli[7], M. Schädel[3], R. Schwengner, J.Żylicz[1]

Studies of nuclei in the ^{100}Sn region offer the possibility to test nuclear models describing structure and decay properties of nuclei in which protons and neutrons occupy identical orbitals near a double shell closure. An insight into the structure of nuclei close to ^{100}Sn can be gained by studying their β decay which is dominated by $\pi g_{9/2} \rightarrow \nu g_{7/2}$ Gamow-Teller (GT) transitions. An attractive feature of such nuclei is that most of the GT strength lies within the $Q_{\rm EC}$-value window. Such a concentration of strength has recently been observed in a series of light indium and silver isotopes (see [1] and references therein). ^{100}Sn has been predicted to decay by one GT transition to a single 1^+ 1p-1h state in ^{100}In at an excitation energy of about 1.8 MeV, while the closest even-even neighbours of ^{100}Sn, ^{98}Cd and ^{102}Sn, show a spreading of the GT strength over a number of 1^+ states in the daughter nucleus.

In the recent experiments at the GSI-ISOL facility we used the FEBIAD-B3C ion sources with the addition of CS_2 [2] for the mass separation of SnS^+ ions. In this way routinely about 60% of the intensity of the Sn^+ beam was shifted to the SnS^+ molecular side-band, where the strong suppression of contaminants [2] cleaned the beams from In, Cd, and Pd isobars. Only the strongly produced activities of Ag were traced in on-line experiments, the suppression of which was 4-5 times lower than the anticipated value of 10^4 found in off-line studies. The latter effect may be due to an operation of the ion source at lower temperature compared to the off-line measurement, which was made to enhance the SnS^+ intensity. We measured β-γ-γ decay properties of $^{101-105}$Sn with two complementary set-ups, namely (i) the Total Absorption Spectrometer (TAS) for the measurement of GT strength distributions and (ii) an array of germanium detectors (including the FZR-Cluster and two GSI-Clover detectors) operated in coincidence with silicon β-detectors. Beta-delayed protons of ^{101}Sn were measured by using $\Delta E - E$ silicon telescopes. The intensities of the mass-separated $^{101-105}$Sn beams were obtained from the experimental decay properties. By using a 40 particle-nA ^{58}Ni beam, a 3 mg/cm^2 ^{50}Cr target, and a catcher of ZrO_2 fibers inside the FEBIAD source, we reached secondary beam intensities given in Table 1. These values are about one to two orders of magnitude higher than those obtained by a previous FRS experiment [3].

The data on the ^{102}Sn decay collected with the high-resolution setup (ii) as well as spectra obtained by the small germanium detector in the TAS confirm the main features of the ^{102}Sn decay scheme proposed by Stolz [3] on the basis of an FRS experiment. The main difference is that we do not confirm the 53 keV transition (see Fig. 1), which was previously [3] placed at the very bottom of the ^{102}In level scheme. Removing this transition from the decay scheme may affect the spin assignment of the ground state of ^{102}In. Figure 2 presents the β-gated TAS spectrum of ^{102}Sn after subtraction of contributions from daughter activities which were determined in separate measurements. The maximum occurring at a recorded TAS energy of about 2.5 MeV is interpreted as being due to the $\pi g_{9/2} \rightarrow \nu g_{7/2}$ GT resonance at a ^{102}In excitation energy of about 1.5 MeV.

In summary, the development of SnS^+ beams at the GSI ISOL allowed us to study in detail the β-decay properties of $^{101-105}$Sn. These data, in particular those on γ-γ coincidences, are under evaluation. An extrapolation of the experimental beam intensities, yields 8 at/h for ^{100}Sn indicating that the measurement of β-delayed γ rays of this nucleus will indeed be a very challenging task.

Table 1 *Measured ISOL rates of the $^{101-105}$Sn isotopes.*

Isotope	^{101}Sn	^{102}Sn	^{103}Sn	^{104}Sn	^{105}Sn
at/min	2.4	31	$1.4 \cdot 10^3$	$3.0 \cdot 10^4$	$2.0 \cdot 10^5$

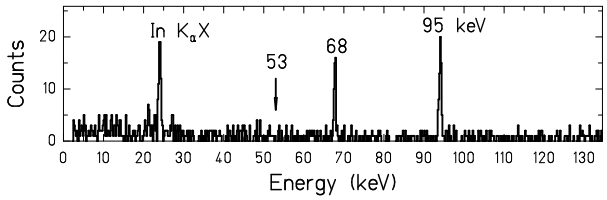

Fig. 1 *Low-energy γ-ray spectrum obtained for mass 102. An arrow shows the expected position of the 53 keV line which remained unobserved in this experiment.*

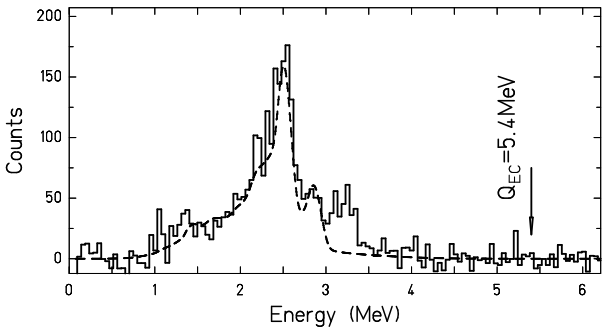

Fig. 2 *Beta-gated TAS spectrum of ^{102}Sn from the experiment (solid line) and from a GEANT simulation based on the modified level scheme of [3] (dashed line).*

[1] C. Plettner et al., Phys. Rev. C 66 (2002) 044319
[2] R. Kirchner, Nucl. Instr. Meth. B, in print, and www.gsi.de/annrep2001 (page 211)
[3] A. Stolz, Ph.D. Thesis, TU München (2001)

[1] *University of Warsaw, PL00681 Warsaw;* [2] *St. Petersburg Nuclear Physics Institute, RU-188350 Gatchina;* [3] *GSI, 64291 Darmstadt;* [4] *Technische Universität München, 85747 Garching;* [5] *Instituto de Estructura de la Materia, IEM CSIC, 28006 Madrid, Spain;* [6] *Universitá di Napoli, 80126 Napoli, Italy;* [7] *INFN Napoli, Italy*

Beta Decay of ^{103}Sn [G]

O. Kavatsyuk[1,2], M. Kavatsyuk[1,2], J. Döring[1], L. Batist[3], A. Banu[1], F. Becker[1], A. Blazhev[1,4], W. Brüchle[1], T. Faestermann[5], M. Górska[1], H. Grawe[1], Z. Janas[6], A. Jungclaus[7], M. Karny[6], R. Kirchner[1], M. La Commara[8], S. Mandal[1], C. Mazzocchi[1], I. Mukha[1], C. Plettner[1], A. Płochocki[4], E. Roeckl[1], M. Romoli[8], M. Schädel[1], R. Schwengner, J.Żylicz[6]

Doubly closed-shell nuclei and neighbouring isotopes/isotones provide a sensitive test ground for the nuclear shell model. ^{100}Sn is the heaviest doubly magic $N = Z$ nucleus, located at the proton drip line, where protons and neutrons occupy identical shell-model orbitals. The overlap of their wave functions is large, which further causes a strong proton-neutron interaction to be expected. Beta decay in this region is dominated by an allowed Gamow-Teller (GT) transformation $\pi g_{9/2} \rightarrow \nu g_{7/2}$, which populates the $I^\pi = 1^+$ GT resonance in the decay of an even-even nucleus. For an odd-neutron parent nucleus the coupling of this resonance to the unpaired nucleon can be studied. This provides a test of the residual interaction via the β-delayed γ-ray spectroscopy.

Measurements of β-delayed γ rays and protons were performed at the GSI-ISOL facility for ^{101,103,105}Sn. It was essential for this experiment to suppress efficiently the isobaric indium, cadmium, silver and palladium contaminants by using the novel sulphurisation technique [1]. The β-delayed γ-ray spectra were measured with an array of high-resolution germanium detectors (17 crystals) in grow-in mode as well as with the Total-Absorption Spectrometer (TAS) in decay mode. Moreover, a $\Delta E-E$ telescope was used to record β-delayed protons [2, 3] Further experimental details are given in refs. [1-3].

We report on the new data for the β decay of ^{103}Sn. In Fig. 1 the β-gated γ-ray spectrum for ^{103}Sn, taken at mass $A = 103 + 32$ (SnS, cf. [1, 2]) with the germanium array, is shown. The 720, 726 and 740 keV lines are known to belong to the decay of the ^{103}In daughter activity [4]. The 1077 keV line has been identified by in-beam spectroscopy [5] to represent the $11/2^+ \rightarrow 9/2^+$ transition in ^{103}In. The data shown in Fig. 1 yield the first evidence for β-delayed γ rays at 643, 821, 1077, 1356, 1397 and 1428 keV, which are preliminarily assigned to the decay of ^{103}Sn. The TAS spectrum gated by protons is shown in Fig. 2. The 776 and 776 + 1022 keV lines correspond to the 2^+ state in ^{102}Cd fed by β-delayed protons after a EC and β^+-decay of ^{103}Sn, respectively. Based on these data, a β^+/EC ratio of 0.06 for the proton emission to the 2^+ state in ^{102}Cd was estimated. A corresponding ratio of 0.6 for the proton emission to the ground state in ^{102}Cd was obtained using a proton-γ anti-coincidence condition. The $Q_{\rm EC}$ value of ^{103}Sn was preliminarily determined from these β^+/EC ratios and the average energy of β-delayed protons [6] to be (7.5 ± 0.5) MeV.

The half-life of ^{103}Sn, obtained from the β-delayed proton time distribution, is shown in the inset of Fig. 2. The result of the fit being $T_{1/2} = (7.0 \pm 0.6)$ s is in agreement with the previously measured values of (7 ± 3) s [5], (7.5 ± 1.5) s [6] and in disagreement with (8.7 ± 0.6) s [7] by two standard deviations.

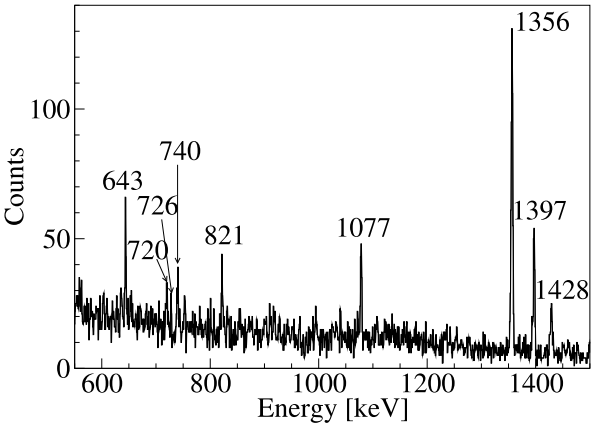

Fig. 1 *Gamma-ray spectrum obtained for mass A = 103 + 32 in coincidence with positrons. The strongest lines are marked with their energies in keV.*

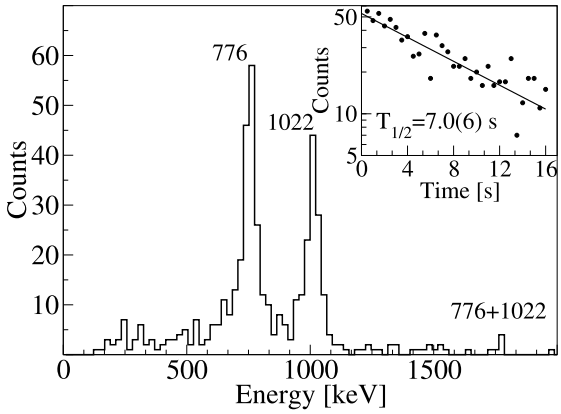

Fig. 2 *TAS spectrum taken in coincidence with β-delayed protons from the ^{103}Sn decay. The inset shows the time characteristic of β-delayed protons.*

[1] R. Kirchner, Proc. Conf. to EMIS-14, Nucl. Instr. Meth. A, in print
[2] M. Karny et al., This Report, p. 42
[3] I. Mukha et al., GSI Sci. Rep. 2002
[4] J. Szerypo et al., Z. Phys. A 359 (1997) 117
[5] J. Kownacki et al., Nucl. Phys. A 627 (1997) 239
[6] P. Tidemand-Petersson et al., Z. Phys. A 302 (1981) 343
[7] K. Rykaczewski, Report GSI-95-09, 1995
[8] A. Stolz, Ph.D. Thesis, TU München (2001)

[1] *GSI, 64291 Darmstadt;* [2] *Kiev National University, Ukraine;* [3] *St. Petersburg Nuclear Physics Institute, Russia;* [4] *University of Sofia, Bulgaria;* [5] *Technische Universität München;* [6] *University of Warsaw, Poland;* [7] *Instituto Estructura de la Materia, CSIC, and Departamento de Fisica Teórica, UAM Madrid, Spain;* [8] *Universitá di Napoli, Italy*

Gamma-Ray Spectroscopy of Fission Fragments with Super Clover Ge Detectors [G]

H. Sharma, A. Wagner, P. Adrich[1], P. Jesinger[2], J. Kopatch[3], J.v. Kalben[2], I. Kojouharov[4], A. Krasznahorkay[5], E. Lubkiewicz[1], Z. Mezentseva[3], M. Mutterer[6], W. Trzaska[7], H.-J. Wollersheim[4]

Gamma-ray spectroscopy of ternary and binary fission fragments have been carried out with a spontaneous fission source at GSI. A very thin and open ^{252}Cf fission source with activity of about 25kBq (fission/s) was mounted in the centre of a double ionization chamber. Both sides of the source were evaporated with 10μg/cm^2 gold in order to prevent the loss of ^{252}Cf by sputtering. The prompt gamma-rays were measured with the GSI super-clover segmented Ge detectors and the fission fragments were detected by a double ionization chamber. The light charged particles from ternary fission were also measured with an array of 24 $\Delta E-E$ telescopes mounted in the double ionization chamber. These telescopes consist of small segmented ionization chambers (for ΔE measurement) and silicon PIN diodes (for E measurement). All these detectors inside the ionization chamber were operated in CH_4 environment at pressure of about 570 torr. The gamma-rays, the light charged particles, and the fission fragments were measured in coincidence. A fragmented cathode was used in the ionization chamber for the determination of polar and azimuthal emission angles of the fragments. The sketch of the experimental setup is shown in Fig. 1. More details of the experiment are availabe at the GSI web site [1].

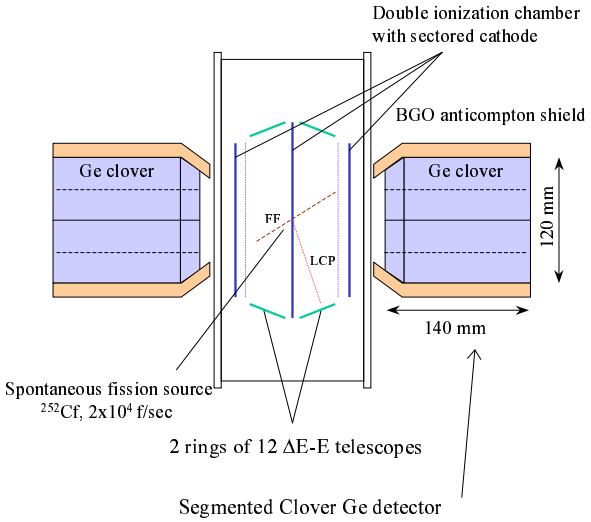

Fig. 1 *The sketch of the experimental setup at GSI.*

The list-mode coincidence data of more than 800 GB were taken during several weeks of experiment. The analysis of the data is in progress in order to extract the information of angular anisotropy of gamma-rays, fragments and light charged particle correlation, gamma-ray emission from light charged particles in ternary fission. The preliminary results of the analysis are shown in Figs. 2 and 3. Fig. 2 shows the energy versus mass distribution (upper) and the typical fission fragments mass distribution (lower). Fig. 3 represents the gamma-ray spectra with and without mass gating and also the spectra with improved quality after the Doppler correction.

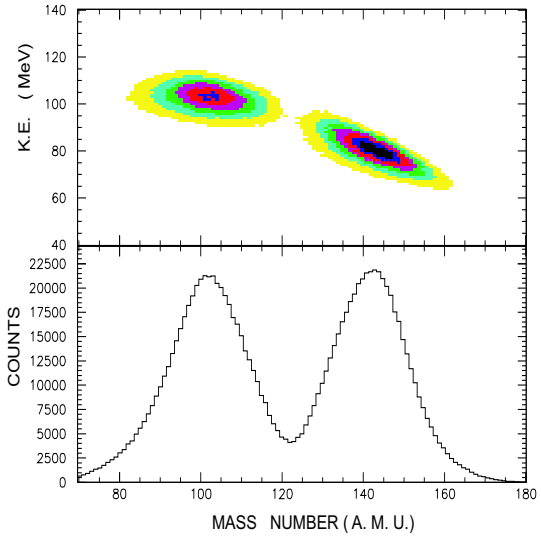

Fig. 2 *Energy versus mass number (top), fragment mass distributions (bottom).*

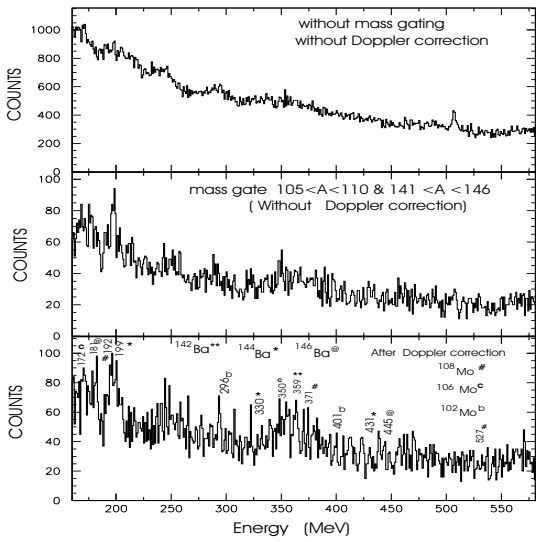

Fig. 3 *The gamma-ray spectra without any mass gating (top) with mass gating (middle) and with mass gating and with Doppler correction (lower).*

[1] http://www-aix.gsi.de/∼wolle/FISSION/fission.html

[1] *Jagellonian Univ., Cracow (Poland),* [2] *Tech. Univ., Darmstadt (Germany),* [3] *Joint Institute for Nuclear Research, Dubna (Russia),* [4] *Gesellschaft für Schwerionenforschung Darmstadt (Germany),* [5] *ATOMKI, Debrecen (Hungary),* [6] *Tech. Univ. Darmstadt (Germany),* [7] *Univ. of Jväskylä (Finland)*

Study of the Neutron-Rich Isotopes ^{91}Sr and ^{92}Sr in a Fusion-Fission Experiment

E.A. Stefanova[1], M. Danchev[2], R. Schwengner, D.L. Balabanski[2,3], M.P. Carpenter[4], M. Djongolov[3], S.M. Fischer[4], D.J. Hartley[3], R.V.F. Janssens[4], W.F. Mueller[5], D. Nisius[4], W. Reviol[6], L.L. Riedinger[3], O. Zeidan[3]

The Sr isotopes lying between the magic nuclide ^{88}Sr (N = 50) and the nuclide ^{94}Sr (N = 56) at the $1d_{5/2}$ neutron subshell closure represent one of the regions of very low collectivity in the nuclear chart. Almost constant $B(E2, 2_1^+ \rightarrow 0_1^+)$ values of $\approx$ 8 W.u. and 13 W.u. were found for $^{90-94}$Sr ($N = 52 - 56$) and ^{96}Sr ($N = 58$), respectively [1]. On the other hand, an onset of collective motion may be expected for nuclei with a few nucleons outside the shell closures. In order to study the interplay between single-particle excitations and collective motion as, e.g., vibrational-like excitations, we studied the nuclides ^{91}Sr and ^{92}Sr having three and four $1d_{5/2}$ neutrons, respectively, outside the shell closure at $N = 50$.

The nuclei ^{91}Sr and ^{92}Sr were produced as fission fragments via the fusion reaction ^{36}S + ^{159}Tb at a beam energy of 165 MeV. The ^{36}S beam was delivered by the 88-inch cyclotron of the Lawrence Berkeley National Laboratory. The target consisted of a ^{159}Tb layer of 0.78 mg cm^{-2} thickness evaporated on to a 13 mg cm^{-2} Au backing. Gamma rays were detected with the Gammasphere array [2] consisting of 93 Compton suppressed Ge detectors arranged in 17 angular rings. A minimum of four coincident γ rays was required, and a total of about 5 $\times 10^9$ events was collected.

The level scheme of ^{92}Sr resulting from the present experiment is shown in Fig. 1. On the basis of the present DCO analysis spin assignments were made for the first time.

Excited states in ^{91}Sr and ^{92}Sr were interpreted in the framework of the spherical shell model. The calculations were performed in a model space including the proton orbitals $(0f_{5/2}, 1p_{3/2}, 1p_{1/2}, g_{9/2})$ and the neutron orbitals $(1p_{1/2}, 0g_{9/2}, 1d_{5/2})$. Experimental and calculated level energies in ^{92}Sr are compared in Fig. 2. The calculations give a good overall description of the observed states. The 3^-, 5^-, and 7^- states in ^{92}Sr are described by coupling the proton excitations creating the octupole 3^- state of the core nucleus ^{88}Sr to the $1d_{5/2}^4$ neutrons. The observed equidistant $\Delta J = 2$ level sequence on top of the 8^+ state, which resembles a vibrational-like sequence, could be well described by the configuration $\pi[(0f_{5/2}^{-2})(0g_{9/2}^2)]\nu(1d_{5/2}^4)$ that favours even spins (cf. Fig. 2). The results of this study have been published in Ref. [3].

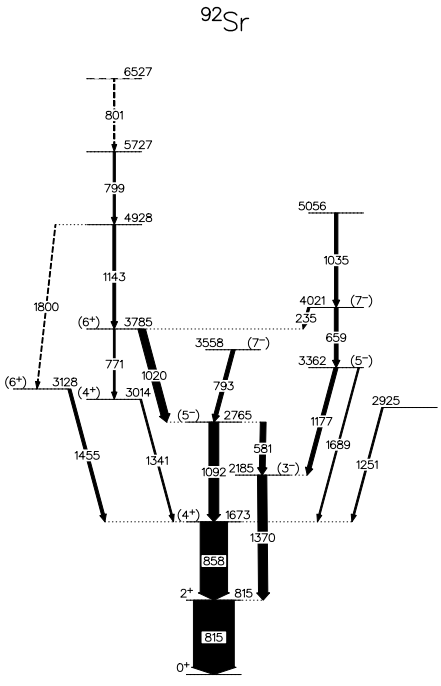

Fig. 1 *Level scheme of ^{92}Sr deduced from the present study.*

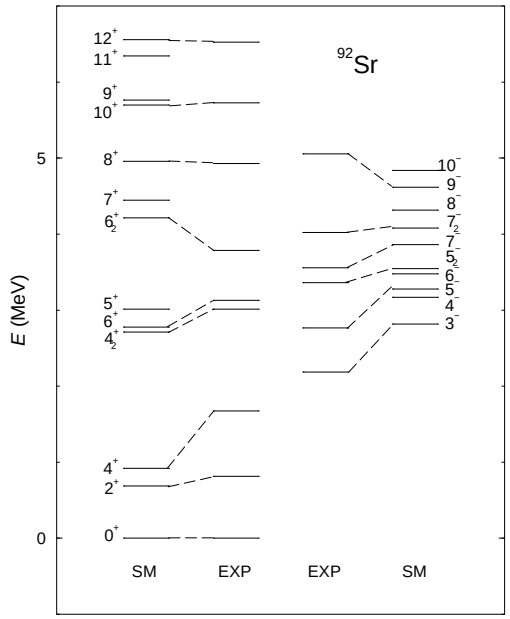

Fig. 2 *Experimental and calculated level energies in ^{92}Sr.*

[1] H. Mach et al., Nucl. Phys. A 523 (1991) 197
[2] I.Y. Lee, Nucl. Phys. A 520 (1990) 641c
[3] E.A. Stefanova et al., Phys. Rev. C 65 (2002) 034323

[1] *FZR and INRNE Sofia, 1784 Sofia, Bulgaria*
[2] *Faculty of Physics, University of Sofia, 1164 Sofia, Bulgaria*
[3] *Department of Physics and Astronomy, University of Tennessee, Knoxville, Tennessee 37996*
[4] *Physics Divison, Argonne National Laboratory, Argonne, Illinois 60439*
[5] *NSCL, Michigan State University, East Lansing, Michigan 48824*
[6] *Chemistry Department, Washington University, St. Louis, Missouri 63130*